Universitat Autònoma de Barcelona

Computational studies of thermal transport in functional oxides

Juan Antonio Seijas Bellido

DOCTORAL THESIS

Computational studies of thermal transport in functional oxides

Author:
Juan Antonio Seijas Bellido

Supervisors:
Riccardo Rurali
Jorge Íñiguez

Doctoral Program in Physics
Universitat Autònoma de Barcelona
Institut de Ciència de Materials de Barcelona (ICMAB-CSIC)
Bellaterra

October, 2019

ICMAB
INSTITUT DE CIÈNCIA DE MATERIALS DE BARCELONA
EXCELENCIA SEVERO OCHOA
CSIC
CONSEJO SUPERIOR DE INVESTIGACIONES CIENTÍFICAS

UAB
Universitat Autònoma de Barcelona

Report submitted for the achievement of the Doctor degree in Physics by:

Juan Antonio Seijas Bellido

Checked and accepted:

Dr. Riccardo Rurali

ICMAB
INSTITUT DE CIÈNCIA DE MATERIALS DE BARCELONA
EXCELENCIA SEVERO OCHOA
CSIC
CONSEJO SUPERIOR DE INVESTIGACIONES CIENTÍFICAS

Dr. Jorge Íñiguez

LUXEMBOURG INSTITUTE OF SCIENCE AND TECHNOLOGY
LIST

Bellaterra, October 2019

Acknowledgments (Agradecimientos)

The development of this Thesis has been possible thanks to the FPI program, so I want to acknowledge the financial support by the Ministerio de Economía, Industria y Competitividad (MINECO) under Grants No. FEDER-MAT2013-40581-P and No. FEDER-MAT2017-90024-P.

Desde el punto de vista personal, antes que nada, quiero dar las gracias a mis tutores, Riccardo y Jorge, por haberme guiado durante estos cuatro años y haberme ayudado a aprender tantas cosas interesantes. Ha sido una suerte tener dos supervisores que antepongan mi futuro a sacar resultados y publicar artículos.

También agradecer a toda la gente de mi grupo la ayuda prestada a lo largo de estos años y las conversaciones a la hora de comer. Gracias a Pol, Hugo, Miquel R., Miquel L., Madhura, Kostia, Matteo, Fernan,... y especialmente a Andrea, por haberse comido todos los trámites burocráticos siempre unos meses antes que yo y facilitarme la vida.

Agradecer también a Carlos su colaboración y todos los ratos que ha sacado para solucionarme dudas, además de haberme sacado por Luxemburgo cada vez que he ido de visita. Por supuesto también tengo palabras de agradecimiento para Claudio, Luciano, y el resto de compañeros de Cagliari, que me acogieron como a uno más esos tres meses de estancia.

Ha sido genial estudiar estos años en un sitio con tanta gente y tan buen ambiente como el ICMAB. Además de todo lo aprendido, también ha sido una suerte conocer al grupo de Cerdanyola, con Javi, Isa, Bego, Cristiano, Quique, Edu,... además de otros amigos como Laia, Francesc, Laura,... y muchos más, con los que tantas horas de

SAF he compartido, además de excursiones de fin de semana, fiestas y tardes en La Giralda. También me alegro mucho de haber compartido despacho con Susana y con todas las personas distintas que han ido rotando por aquí, por las buenas horas de conversación interesante y de entretenimiento los días más complicados. Aunque después de hacer la tesis la gente tienda a desperdigarse espero que nos sigamos viendo durante mucho tiempo.

Desde luego no me olvido de Aleandro, al que podría haber mencionado en varios de los apartados anteriores, pero por ello mismo me ha parecido que necesitaba una línea para el solo por haber estado ahí todos estos años.

También quiero dedicar unas líneas a mis compañeros de máster de este último año, especialmente a Cris y David, y también a los compañeros de almuerzo Mathias, Migue y Roser. Me ha encantado que algo que me parecía un trámite haya dado tan buenos resultados. Sois el principal motivo por el que ahora me alegre de haber hecho el máster en la UAB y no a distancia.

Agradecer también a todos mis compañeros de Barcelona, especialmente a Sergio y Lucía, todo el tiempo que hemos pasado y todo el trabajo que hemos hecho juntos, y sobre todo el que han hecho ellos mientras yo estaba escribiendo esta tesis. Ha sido genial aprender tanto con vosotros estos últimos años.

Muchas gracias también a la mayoría, a los que aunque estando lejos me ha parecido tenerlos cerca. Hablo de los físicos de Sevilla: Alberto P., Jose, Carlos,..., de los amigos de Sevilla: Alberto M., Cari, Elena, Jose, Lara, Quenopa, Sergio, Pablo, Gonzalo,..., y por supuesto de la familia que se elige: Jose, Iván, Borja, Ángel, Sergio, Gonzalo,... y de todos aquellos que siguen siendo una parte esencial de mi vida.

Agradecer a mi familia, principalmente a mi madre, mi padre y mi hermano, el haber estado ahí siempre y el saber que seguirán estando. Espero estar más cerca yo a partir de ahora.

Finalmente, quiero agradecer a Cristina el haber estado a mi lado todos estos años. No me puedo imaginar una persona mejor con la que haber compartido tantos momentos.

A todos vosotros, gracias.

Abstract

This Thesis collects the computational works we have done in the field of condensed matter physics, focused on the thermal transport properties of the Lead Titanate ($PbTiO_3$) and the Zinc Oxide (ZnO), both representative materials of many other insulating functional oxides. The first has been modeled using a second-principles potential, that is, a potential parameterized from first-principles calculations, which captures some quantum effects that can be relevant in the material. We have modeled the second one using the Buckingham's potential, a simple analytical expression that seems to describe the behavior of ZnO in a fairly approximate agreement with experiments.

In particular, we focus on how to modulate their thermal conductivity modifying their crystal lattice by means of an external electric field or pressure. Our studies have been always performed within the framework of Fourier's law, from two different techniques: performing Molecular Dynamics simulations, both at equilibrium and out-of-equilibrium, and solving the Boltzmann Transport Equation for phonons. Both techniques superbly combine, since while Boltzmann Transport Equation takes into account the quantum effects that intervene in the microscopic description of the system, but only up to the third order of the anharmonic scattering, Molecular Dynamics trajectories are classical but capture all scattering events, i.e., all orders of anharmonicity are included.

These studies also describe how phonons are affected when the crystal lattice of both oxides is altered, explaining which changes of their properties (frequency, velocity and mean free path) are relevant for the changes in thermal conductivity. Additionally, this work also present various applications in the field of phononics, laying the groundwork for the design of thermal switches and transistors.

Contents

Chapter 1

Introduction

The study of the thermal properties of materials is a very important field of research since they have a strong impact in many technological dispositives and in many devices of our daily life. In addition, they have relevance in all size scales, from nanostructured materials and microchips that can overheat, to objects such as the structure of a building, which can expand due to an increase of temperature. In this Thesis we work with bulk oxides, but due to the techniques we use our results would be also applicable in devices of micro and nano sizes.

The advances made in physics allow us to intervene at times in the thermal behavior of some insulators, designing materials with desired properties. Nonetheless, our current ability to control heat transport in insulators is rather limited and mostly consists in modulating the amount of scattering experienced by the heat-carrying phonons [1]. This approach is normally pursued by designing systems with tailor-made boundaries [2, 3], defect distributions [4, 5], or periodic sequences of different materials or nanostructuring [6–8], as in superlattices and phononic crystals. These strategies allow us to target a given thermal conductivity. Nevertheless, alternative approaches enabling a dynamical modulation of the thermal conductivity are seldom tackled because of the subtleties related with phonon manipulation.

The intrinsic difficulty in manipulating phonons is often ascribed to the fact that they do not possess a net charge or a mass; thus, it is difficult to control their propagation by means of external fields [9]. However, this is not always the case [10–13]. Insulators or semiconductors often feature polar phonons, i.e., phonons which typically involve atoms with different charges and have a vibrating electric dipole associated to them. These polar phonons can be acted upon by an external electric field, to harden or soften them, which should result in a modulation of the thermal conductivity. Further, the structural dielectric response of an insulator, which is mediated by these very polar modes, may have significant effects in the entire phonon spectrum, via anharmonic couplings, and further affect the conductivity.

In this Thesis we exploit this simple, yet almost unexplored, idea. We show thermal conductivity can indeed be controlled by an external applied electric field, and that this effect leads to a genuine thermal counterpart of the field effect in usual electronic transistors. Indications that such an electrophononic effect can be obtained experimentally have been previously reported in $SrTiO_3$ at very low temperatures [14, 15].

Another goal of phononics [9, 16, 17] is the proper modulation of the thermal flux to encode basic logic functions in devices that operate with heat currents rather than with charge carriers or electromagnetic waves. These operations rely on the existence of two well separated high and low conductance states, which are used to encode the logical values of 1 and 0. These two states should be as different as possible and it has to be possible to commute back and forth between them. Many materials are anisotropic and thus provide naturally access to two distinct conductance states, but practical implementations are nevertheless hindered. On the one hand, the anisotropy is often small, like in wurtzite crystals [18–20] where κ_{xx}/κ_{yy} may range from 0.96 (GaP) to 1.18 (ZnSe) at 300 K. In other materials, however, it can be much larger and a convenient limiting case is graphite. In that case, the in-plane thermal conductivity is orders of magnitude larger than the out-of-plane one [21], along which phonon propagation is mediated by weak van der Waals forces. On the other hand, and more importantly, switching from one conductance state to the other is normally not possible, because the device design determines the element of the thermal conductivity tensor that is relevant for phonon transport, i.e., heat flows along a given crystallographic direction and the sample cannot be rotated.

All these mentioned studies have been developed in this Thesis using $PbTiO_3$, a representative oxide of the ferroelectric perovskite oxides. These materials are anisotropic, and their anisotropy is determined by the off-center displacement of the cations with respect to the surrounding oxygen cages. This distortion of the lattice has an associated polarization that can thus be reoriented or fully reversed with an external electric field. Consequently, the access to a different element of the thermal conductivity tensor is allowed within a given device setup, thus implementing a thermal switch. In this same material, different domains of polarization can be created, which would affect the heat propagataion through the Domain Walls that separate the domains. As the domains can be written by means of an external electric field, we present another way to dynamically change from a low to a high conductance state.

A continuous modulation of the thermal conductivity can be also achieved in some materials by applying directly an external strain instead of an electric field to modify the crystal lattice. Strain engineering is an active field of research in condensed matter physics and in nanoscience with several applications in the design and optimization of electronic devices [22–24]. It consists in tuning the properties of a material by a suitable compressive or tensile strain. Indeed, the use of strained Si in conventional electronic devices represented a significant technological breakthrough, dramatically boosting chip speeds because of the increased electronic mobility [25, 26]. Comparatively less attention has been devoted to the effect of strain on thermal conduction [27], so in this Thesis we dedicate one Chapter to understand and quantify it, applying strain to a sample of ZnO.

To summarize, this Thesis presents several ways to modify the crystal lattice of some materials, by applaying an instantaneous or a long lasting electric field or by applying strain. With our research we have managed to delve into various theoretical aspects that were not established so far, and this has allowed us to control these external mechanisms to affect the lattice thermal conductivity of solids and design different structures for phononic applications. We expect that our results can stimulate experiments to verify our predictions. The Chapters are organized as follows. In Chapter 2 we introduce basic concepts of thermal transport, and the theoretical background of the techniques that have been used in this Thesis. In Chapter 3 the materials used in our simulations are described, and also the theory requiered to model the behavior of these materials is explained. In Chapter 4 we evaluate the thermal boundary resistance of 180° domain walls in $PbTiO_3$ within the numerical formalisms of non-equilibrium molecular dynamics. The obtained results prove the viability of an electrically actuated phononic switch. In Chapter 5 we demonstrate a fully electric control of the heat flux, which can be continuously modulated by an externally applied electric field, revealing the mechanisms by which experimentally accessible fields can be used to tune the thermal conductivity. In Chapter 6 we present a theoretical proposal for the design of a thermal switch based on the anisotropy of the thermal conductivity of $PbTiO_3$ and of the possibility to rotate the ferroelectric polarization with an external electric field. The calculations are based on an iterative solution of the phonon Boltzmann Transport Equation. In Chapter 7, using a combination of equilibrium classical molecular dynamics (within the Green-Kubo formalism) and the Boltzmann Transport Equation, we study the effect of strain on the ZnO thermal conductivity focusing in particular on the the case of hydrostatic and uniaxial strain. Finally, in Chapter 8 we expose our final comments about the developed work in this Thesis and future goals that can be achieved related with the studies presented here.

Chapter 2

Thermal transport

The main topic of this Thesis is to study how the thermal transport properties of different materials change when tuning their structures by different methods. The materials we have studied are isolating systems, which means that heat conduction due to the electrons is negligible. Therefore, when we talk about thermal conductivity we are referring just to the property of the materials of conducting heat due to the atomic vibrations of the lattice, that is, the lattice thermal conductivity κ.

Many computational techniques have been developed to calculate the thermal conductivity of a solid. To name a few, an original one is the phenomenological model presented by Callaway et al. [28], that requires experimental data and works at low temperatures. There are also other clever methods, like solving the Slack equation, that only requires the acoustic Debye temperature and the Grüneisen parameter of the material to calculate its thermal conductivity. This have been done recently by some authors that have also complemented the methodology using modern techniques [29, 30]. Although these methods are less time-consuming and can provide accurate results for some materials, people typically use more accurate methods to calculate the thermal conductivity, such as a Molecular Dynamics simulation or solving the Boltzmann Transport Equation for phonons. These methods are the ones used in this Thesis and are going to be discussed in this Chapter. However, before that we have to mention that these methods assume the validity of the Fourier's law, what means a linear relation between the thermal flux $\vec{J}$ and the temperature gradient

$$\vec{J} = -\kappa \vec{\nabla} T. \tag{2.1}$$

In most cases this assumption is reasonable, like in the cases we have studied in this Thesis, where we have worked with bulk materials. In bulk materials at typical conditions of temperature and volume we can consider that the thermal transport is diffusive, because of the huge number of scattering processes that phonons suffer. Because of this, their movement can be considered as a Brownian motion, so the Fourier's law applies. Nevertheless for lenght scales smaller than the mean free path of phonons, they go over their trajectory in a straight line, because they do not suffer any scattering process in such a short path, meaning that heat flow changes from diffusive to ballistic, so the Fourier's law does not apply. Some recent experiments have found this deviation from Fourier heat transport [31, 32], and in consequence new methods have emerged to explain the behavior of the heat in these cases.

One of these methods consist in solving an hydrodynamic heat flux equation like that

$$\vec{J} + \tau \frac{\partial \vec{J}}{\partial t} = -\kappa \vec{\nabla} T + l^2 (\nabla^2 \vec{J} + 2 \vec{\nabla} \nabla \cdot \vec{J}), \tag{2.2}$$

a generalization of the Fourier's law that can be obtained using the Extended Irreversible Thermodynamics formalism [33]. The name hydrodynamic is due to its similarity with the Navier-Stokes equation. In Eq. (2.2) τ and l are bulk (i.e. without considering any boundary effect) total relaxation time and non-local length respectively. The value of l determines the non-local range in phonon transport and is related to the viscosity of the phonons distribution. This equation is an improvement over Fourier's law becasuse of two reasons. On one side, it includes memory effects by the time derivative term on the left, which takes into account that the steady state is not reached immediately (Fourier's law is only valid in the stationary state). Besides it includes a geometric factor by the term with the laplacian and the gradient of the divergence, which take into account the shape of the system. Eq. (2.2) can be solved by finite elements, and the thermal conductivity that appears is usually calculated using the Kinetic Collective Model (KCM) [34, 35]. This model is derived from the exact solution of the Boltzmann Transport Equation (BTE) obtained by Guyer and Krumhansl [36], based on splitting the collision processes in two: ones that conserve the total momentum of the system but redistribute momentum between different phonons (normal processes), and others that give part of the momentum to the crystal lattice (resistive processes). The KCM, in addition to obtaining a value for the thermal conductivity of equivalent precision to one obtained by the iterative method for solving the BTE, also allows to obtain the values of the parameters that intervene in Eq. (2.2). As mentioned before, in this Thesis, as our studies have been permormed only with bulk materials, we have always assumed that Fourier's law applies.

2.1 Boltzmann Transport Equation

We are going to start this section by briefly defining what phonons are. As explained in all text books of solid state physics, the most generic vibration of a solid is a superposition of its normal modes. A normal mode is an oscillatory movement of the lattice in which all parts move sinusoidally with the same frequency and with a fixed phase relation. They are normal in the mathematical sense of orthogonality, because they are calculated using only the harmonic part of the interaction potential. Physically this means that they can vibrate independently, that is, an excitation of one mode will never cause motion of a different one. The normal modes of a crystal can be obtained by solving the equations of motion of the atoms in the unit cell, and they will be identified by the wave vector $\vec{k}$ (or sometimes, equivalently, by the reciprocal lattice vector $\vec{q}$) and its branch index s. They can also be in different excited states n, that is, they can have different frequencies of vibration ω. Nowadays the studies of solid state physics are performed in the framework of quantum theory, so a quantum version of the normal modes theory has been developed. A corcuspular description is more useful than the undulatory one, specially when one takes into account the anharmonic part of the potential, allowing the exchange of energy between the modes. When working with this description, instead of saying that the normal mode of the branch s with reciprocal lattice vector $\vec{q}$ is in its n^{th} excited state, one says that there are n phonons of type s with reciprocal lattice vector $\vec{q}$ present in the crystal. Therefore phonons are quasiparticles that in the quantum theory represent the normal modes, the quantum of structural vibrations. The thermodynamic properties of a crystal are related with the phonons that can populate it. For example, the specific heat mainly depends of the high-frequency phonons, while thermal conductivity is tipically more affected by the low-frequency ones.

In this section we are going to develop a theory to calculate the thermal conductivity of a system taking into account the properties of all the phonons that populate it. Instead of identifying a phonon by the reciprocal lattice vector $\vec{q}$ and the phonon branch index s as explained before, for simplicity we are going to define a unique index that encompasses both, $\lambda = \{\vec{q}, s\}$. The description will be semi-classical, because on one side we assume that the positions and the velocities of phonons are well determined, however, on the other hand, we are going to apply quantum statistics to study their populations.

When the system is at equilibrium, phonons are spread between the possible states as indicates the Bose-Einstein distribution

$$f_\lambda^{\mathrm{BE}} = \frac{1}{e^{\beta\hbar\omega_\lambda} - 1}, \tag{2.3}$$

where β is the inverse of the temperature multiplied by the Boltzmann constant $\beta = 1/k_B T$, $\hbar$ is the reduced Planck's constant and ω_λ is the angular frequency of the mode λ. But if we assume just local equilibrium at each point $\vec{r}$ of the space and also that there is a small temperature gradient in the system, the population of the states $f_\lambda(\vec{r}, t)$ will slightly deviate from its equilibrium distribution. Because of that in the system will appear a thermal flux that will try to equilibrate the temperature, and that can be expressed in function of the phonon properties as

$$\vec{J} = \sum_\lambda \hbar\omega_\lambda \vec{v}_\lambda f_\lambda, \tag{2.4}$$

where $\vec{v}_\lambda$ is the group velocity, and we have not written explicitly the dependence of f_λ with respect $\vec{r}$ and t to use a lighter notation [37]. To be able to calculate the thermal conductivity of the system using the Fourier's law (Eq. (2.1)) we need to obtain the value of all the magnitudes that define $\vec{J}$. The most difficult to obtain is f_λ, and to achieve that we need the Boltzmann Transport Equation (BTE).

Originally, the equation was developed to statistically describe transport of classical particles of an idealized diluted gas. But nowadays the use of the BTE have been extended to the study of quantum particles, like for studying the electronic transport in different materials [38, 39]. It can be also used to study the distribution function of phonons [37, 40–42], that is in what we are interested. We are going to use its differential form, and to write it we are going to consider that under steady-state conditions, the distribution function should be constant at any point, so the equation looks like

$$\frac{\partial f_\lambda}{\partial t} = 0. \tag{2.5}$$

The phonons distribution may change because of the following reasons:

- As there is a gradient in the system, and also phonons have their own velocities, some phonons can enter in a region of the space and others can leave it. So this term will be proportional to the gradient and to the velocity of phonons, and is called diffusive or entropic term

$$\left.\frac{\partial f_\lambda}{\partial t}\right|_{\text{diff}} = -\vec{v}_\lambda \cdot \frac{\partial f_\lambda}{\partial \vec{r}}. \tag{2.6}$$

- If there is an external force which is able to affect the particles we are studying, we need to add a term that captures this effect, for example, if we are studying the electrons of a system under an external electric field. But as we are working with phonons that have neither mass nor charge, we are going to neglect this term. In Chapter 5 we study how an external electric field affects the thermal conductivity of an oxide, but you will note that it is a different situation. We are avoiding the external force term because there is no external force that can directly modify the distribution function f_λ, the behavior of phonons, but what we do in Chapter 5 is to modify the lattice by means of a field, what results in different phonon bands for the material.

- Phonons may interact with each other and also with defects of the lattice or its boundaries, so we are going to call this term the scattering term. There will be processes that involve just one phonon, like scattering from isotopic disorder, that requires two λ index, the one that describes the state of the phonon before the scattering (λ) and the one that describes the phonon after it (λ'). We will have also processes with three phonons, for example the collision between two phonons λ and λ' that merge in a third one λ'', or one phonon that is decomposed in other two. As we consider elastic scattering between the states, these terms are proportional to the occupation numbers of the initial and final state, for example in the case of two phonons that merge in a third one, the term would include $f_\lambda f_{\lambda'}(1+f_{\lambda''})$. The term would be also proportional to the intrinsic probability of the transitions, that have to be determined using time-dependent perturbation theory in the framework of quantum mechanics. The way to do that is to add an extra term to the harmonic Hamiltonian, that will be treated as a perturbation, which makes possible transitions between some states to others of the harmonic Hamiltonian [40]. Typically this is enough to properly describe the thermal properties of a solid, so higher order processes will not be taken into account in the derivation.

As we mentioned before, under steady-state conditions the distribution function has to be constant at any point, so

$$\frac{\partial f_\lambda}{\partial t} = \left.\frac{\partial f_\lambda}{\partial t}\right|_{\text{diff}} + \left.\frac{\partial f_\lambda}{\partial t}\right|_{\text{scatt}} = 0. \tag{2.7}$$

Eq. (2.7) is the Boltzmann Transport Equation for phonons.

The BTE is very difficult to solve, so in order to simplify it we are going to linearize the equation. The diffusive term will vanish if we just insert a distribution function f_λ independent of $\vec{r}$. But our assumption of local equilibrium and the temperature gradient implies that f_λ depends on position $\vec{r}$ through the temperature. So, the diffusive term will take the form

$$\left.\frac{\partial f_\lambda}{\partial t}\right|_{\text{diff}} = -\vec{v}_\lambda \cdot \frac{\partial f_\lambda}{\partial \vec{r}} = -\vec{v}_\lambda \cdot \vec{\nabla} T \frac{\partial f_\lambda^{\text{BE}}}{\partial T}. \tag{2.8}$$

For the scattering term we can not take just the approximation $f_\lambda = f_\lambda^{\text{BE}}$ as in the diffusive term, because in equilibrium the collision term must vanish. So we may expand f_λ around its equilibrium value f_λ^{BE}

until the first-order perturbation

$$f_\lambda = f_\lambda^{\mathrm{BE}} - \vec{F}_\lambda \cdot \vec{\nabla} T \frac{\partial f_\lambda^{\mathrm{BE}}}{\partial T}, \tag{2.9}$$

where $\vec{F}_\lambda$ is the generalized mean free path. We can insert Eq. (2.9) in the expression for the heat current (Eq. (2.4)), and after some calculations and inserting this in the Fourier's law (Eq. (2.1)) we get the expression for the thermal conductivity tensor

$$\boldsymbol{\kappa} = \frac{1}{N\Omega k_B T^2} \sum_\lambda (\hbar\omega_\lambda)^2 f_\lambda^{\mathrm{BE}} (f_\lambda^{\mathrm{BE}} + 1) \vec{v}_\lambda \otimes \vec{F}_\lambda. \tag{2.10}$$

Here N, Ω and k_B are, respectively, the number of $\vec{q}$ points, the volume of the unit cell of the material and the Boltzmann's constant, and $\otimes$ is the symbol for the tensor product. Using also Eq. (2.9) in Eq. (2.7) we get the linearized BTE, now for the variable function $\vec{F}_\lambda$, and we can write the equation as in reference [37]:

$$\vec{F}_\lambda = \tau_\lambda (\vec{v}_\lambda + \vec{\Delta}_\lambda), \tag{2.11}$$

where

$$\frac{1}{\tau_\lambda} = \frac{1}{N} \left(\sum_{\lambda'\lambda''}^{+} \Gamma^{+}_{\lambda\lambda'\lambda''} + \frac{1}{2} \sum_{\lambda'\lambda''}^{-} \Gamma^{-}_{\lambda\lambda'\lambda''} + \sum_{\lambda'} \Gamma_{\lambda\lambda'} \right) \tag{2.12}$$

and

$$\begin{aligned} \vec{\Delta}_\lambda = {} & \frac{1}{N} \sum_{\lambda'\lambda''}^{+} \Gamma^{+}_{\lambda\lambda'\lambda''} \left(\frac{\omega_{\lambda''}}{\omega_\lambda} \vec{F}_{\lambda''} - \frac{\omega_{\lambda'}}{\omega_\lambda} \vec{F}_{\lambda'} \right) \\ & + \frac{1}{2N} \sum_{\lambda'\lambda''}^{-} \Gamma^{-}_{\lambda\lambda'\lambda''} \left(\frac{\omega_{\lambda''}}{\omega_\lambda} \vec{F}_{\lambda''} + \frac{\omega_{\lambda'}}{\omega_\lambda} \vec{F}_{\lambda'} \right) \\ & + \frac{1}{N} \sum_{\lambda'} \Gamma_{\lambda\lambda'} \frac{\omega_{\lambda'}}{\omega_\lambda} \vec{F}_{\lambda'}. \end{aligned} \tag{2.13}$$

Lets explain these equations. τ_λ is the relaxation time of mode λ. Its physical interpretation can be better understood in the framework of the Relaxation Time Approximation (RTA), also called single mode approximation. In this approximation the scattering term is written as

$$-\frac{\partial f_\lambda}{\partial t}\bigg|_{\text{scatt}} = \frac{f_\lambda - f_\lambda^{\text{BE}}}{\tau_\lambda}. \tag{2.14}$$

It can be proved that using this definition of the scattering term leads to Eq. (2.11) with $\vec{\Delta}_\lambda = 0$. Eq. (2.14) can be written as

$$\frac{\partial f_\lambda}{\partial t} + \frac{f_\lambda}{\tau_\lambda} = \frac{f_\lambda^{\text{BE}}}{\tau_\lambda}, \tag{2.15}$$

where can be better appreciated that we are dealing with a first-order differential equation, whose solution if we were working with it as an isolated term would be

$$f_\lambda = f_\lambda^{\text{BE}}(f_\lambda(0) - f_\lambda^{\text{BE}})e^{-t/\tau_\lambda}. \tag{2.16}$$

We can see that this approximation simplifies a lot the resolution of the problem because it treats phonons as a gas of quasiparticles that randomly collide with each other with a characteristic time τ_λ. The RTA assumes that the thermalization of each phonon population is independent of the others, and that the thermal conductivity can be written in terms of individual phonon properties, so in conclusion it is assuming that the main heat carriers are single phonons. Physically, this is equivalent to assume that an amount of heat current is perfectly dissipated any time that a single phonon is scattered, which is not true. There are processes that dissipate heat (Umklapp processes) but also others that just distribute heat between groups of modes (Normal processes). So the RTA is then not able to describe how the heat flux is exchanged through the various modes, giving only an approximate treatment of the heat transport theory. In spite of this, many people still uses this approximation [43, 44] because in practice the obtained results are not too far from the results obtained with the full solution of the BTE. According to Eq. (2.16), the RTA would be good when $(f_\lambda(0) - f_\lambda^{\text{BE}}) \approx 1$, what means that the system starts in a situation close to the equilibrium, and also τ_λ is independent of the distribution function. In this Thesis we will also use it, but also the full solution of the BTE, that requires the whole Eq. (2.11).

Now that we know the RTA, we can say that $\vec{\Delta}_\lambda$ is the measure of how much the population of a specific phonon mode deviates from the RTA prediction. A discretization of the Brillouin zone have been introduced in Eq. (2.13), where N is the number of points used in the grid, and the quantities $\Gamma^{\pm}_{\lambda\lambda'\lambda''}$ are three-phonon scattering rates, and can be expressed as

$$\Gamma^{+}_{\lambda\lambda'\lambda''} = \frac{\pi\hbar}{4}\frac{f^{\mathrm{BE}}_{\lambda'} - f^{\mathrm{BE}}_{\lambda''}}{\omega_\lambda\omega_{\lambda'}\omega_{\lambda''}}|V^{+}_{\lambda\lambda'\lambda''}|^2\delta(\omega_\lambda + \omega_{\lambda'} - \omega_{\lambda''}) \tag{2.17}$$

$$\Gamma^{-}_{\lambda\lambda'\lambda''} = \frac{\pi\hbar}{4}\frac{f^{\mathrm{BE}}_{\lambda'} + f^{\mathrm{BE}}_{\lambda''} + 1}{\omega_\lambda\omega_{\lambda'}\omega_{\lambda''}}|V^{-}_{\lambda\lambda'\lambda''}|^2\delta(\omega_\lambda - \omega_{\lambda'} - \omega_{\lambda''}). \tag{2.18}$$

$\Gamma^{+}_{\lambda\lambda'\lambda''}$ corresponds to absorption processes, which result in only one phonon with the combined energy of two incident phonons ($\omega_\lambda + \omega_{\lambda'} = \omega_{\lambda''}$), whereas $\Gamma^{-}_{\lambda\lambda'\lambda''}$ describes emission processes in which the energy of one incident phonon is split among two phonons ($\omega_\lambda = \omega_{\lambda'} + \omega_{\lambda''}$). Conservation of energy in the absorption and emission processes is enforced by the Dirac delta distributions.

As we are only interested in solids, we can asume that atoms just move around their equilibrium positions, what allow us to expand the potential energy of the system as a Taylor series. The coefficients of the expansion are the force constans of different orders, that is, the derivatives of the energy with respect the position of the atoms, that can be numerically calcaulated performing small displacements of the atoms at constant volume. Different displacements can be equivalents, so the required number of displacements will depend on the symmetry of the crystal. These force constants of the system are necessary because the scattering matrix elements $V^{\pm}_{\lambda\lambda'\lambda''}$ can be obtained from the anharmonic interatomic force constants, like the phonon frequencies, group velocities and phonon populations are determined by the harmonic interatomic force constants. Apart from three-phonon processes, scattering from isotopic disorder is accounted for within the model of Tamura [45].

Once we know all of these elements we can obtain the exact solution of the BTE using an iterative process, pioneered by Omini and Sparavigna [46]. The process consist in a conjugate gradient method for the $\vec{F}_\lambda$s, that are reintroduced in the expression for the $\vec{\Delta}_\lambda$s (that depends on the $\vec{F}_\lambda$s) after each iteration, starting with the RTA solution. To show the iterative process explicitly we could rewrite Eq. (2.11) as

$$\vec{F}_\lambda^{i+1} = \tau_\lambda(\vec{v}_\lambda + \vec{\Delta}_\lambda(\vec{F}_\lambda^i)). \tag{2.19}$$

We consider that the final solution has been reached when the difference between $\vec{F}_\lambda^i$ and $\vec{F}_\lambda^{i+1}$ is smaller than a certain value of tolerance.

2.2 Molecular Dynamics

We are going to use Molecular Dynamics (MD) to calculate the thermal conductivity of different systems in this Thesis, so we are going to introduce what is a MD simulation itself. Molecular Dynamics is a simulation technique which consists of numerically solving the equations of motion for a collection of interacting particles [47]. In our case, these particles will be ions in a periodic lattice as corresponds when one works with crystals, and the equations will be the classical equations of motion. This technique is more like an experiment, in which a sample of material evolves in time, so talking about phonons individually like in the BTE case does not make sense. In a MD simulation all phonons can be present, and they may be affected by scattering processes of all orders, not just the processes in which 3 phonons are involved.

To solve the equations of motion we need to know the interactions between the particles, that means, the potential, that will allow us to calculate the energy of the system for a given atomic configuration. There are many numerical methods to integrate Newton's equations of motion, like the well known leapfrog algorithm or the Euler method, but in this Thesis we are going to use the Velocity Verlet algorithm [48]. Using this algorithm, the positions $\{\vec{s}\}$ of the atoms are updated at the time $t + \Delta t$ by the expression

$$\vec{s}_i(t + \Delta t) = \vec{s}_i(t) + \vec{v}_i(t)\Delta t + \frac{1}{2}\vec{a}_i(t)(\Delta t)^2, \tag{2.20}$$

where $\vec{v}_i$ and $\vec{a}_i$ are the velocity and the acceleration of the i^{th} atom. Obviously, the time is a discrete variable, that increases an amount of Δt in each loop of the algorithm. For this new configuration, the potential energy E^{pot} is obtained from the Hamiltonian of the system, and the forces $\{\vec{F}\}$ acting on each atom are calculated as

$$\vec{F}_i(t + \Delta t) = -\vec{\nabla} E_i^{\text{pot}}(t + \Delta t). \tag{2.21}$$

After that, we use the classical equations of motion to obtain the new accelerations and velocities

$$\vec{a}_i(t+\Delta t) = \vec{F}_i(t+\Delta t)/m_i \tag{2.22}$$

$$\vec{v}_i(t+\Delta t) = \vec{v}_i(t) + \frac{1}{2}(\vec{a}_i(t) + \vec{a}_i(t+\Delta t))\Delta t. \tag{2.23}$$

Repeating this many times we obtain the trajectory of each atom, simulating the real dynamics of the system in an approximate way. We can use these trajectories to determine macroscopic thermodynamic properties of the system, like for example the temperature, that from the equipartition theorem we know that is

$$T = \frac{1}{3k_B N}\sum_{i=1}^{N} m_i|\vec{v}_i|^2, \tag{2.24}$$

where k_B is the Boltzmann constant and N is the number of atoms.

Some datails of this kind of simulations should be discussed. First of all, we have to choose a timestep Δt small enough to integrate the equations of motion with sufficient accuracy so that the energy is conserved, but as long as possible to simulate a longer time. Secondly we have to choose a set of initial conditions, that have to be introduced in Eq. (2.20) the first time we run the algorithm. The ground state of the system is typically chosen as the initial configuration of the system, and the initial velocities are usually random generated using the Maxwell-Boltzmann distribution defined for the desired temperature of the simulation. After that, the velocities are corrected to set at zero the linear and the angular momentums of the whole system, and also, as the initial conditions will not be consistent with the desired temperature of the simulation, we will have to thermalize the system before running our production simulation.

The thermalization process modifies somehow the particles velocities while they evolve in time, until they are compatible with the desired values of the macroscopic variables. At the end of the process, if we let the system evolve free, its not fixed variables (for example the temperature and the pressure in the NVE simulation) will not change either, they will only fluctuate around a fixed value. There are many ways to do the equilibration, for example to use the Berendsen or the

Langevin thermostats, but in this Thesis we use other two different methods. The first one is known as the velocity scaling, and consists in multiply every certain number of steps the velocity of all the particles by the factor $\sqrt{T_{\mathrm{des}}/T_{\mathrm{inst}}}$, where T_{des} is the desired temperature, the temperature at which we want to thermalize the system, and T_{inst} is the instantaneous temperature, the actual temperature of the system. This thermostat suppresses fluctuations of the kinetic energy of the system and therefore cannot produce trajectories consistent with the canonical ensemble. This also causes problems even in the later microcanonic simulation when one is interested in magnitudes related with the fluctuations of the system, like for example the microscopic thermal flux. In the studies where we need to avoid these problems, we use the Nosé-Hoover thermostat [49, 50] that instead correctly generates trajectories consistent with a canonical ensemble. This thermostat introduces an additional fictitious variable in the Hamiltonian coupled to the atomic dynamics to represent a heat bath. The equilibration must be run until the system has lost the memory of its initial conditions and is thoroughly equilibrated at the desired temperature.

In addition to the thermalization process and the rest of the details, we have to take into account that we work with periodic boundary conditions, so our systems are always surrounded by a copy of themselves, which is the typical procedure to study bulk materials. However all this is not enough to obtain the thermal conductivity from a MD simulation, and to achieve that we have to choose one of these three options:

- To perform a MD simulation out of equilibrium and use Fourier's law

  $$\vec{J} = -\kappa \vec{\nabla} T \tag{2.25}$$

  to calculate the thermal flux of the system $\vec{J}$ if the temperature gradient $\vec{\nabla} T$ has been imposed, or vice versa.

- To calculate the microscopic heat flux and its autocorrelation in a standard MD simulation and use the Green-Kubo expression that relates it with the thermal conductivity κ.

- To distinguish two portions of the system and thermalize them at two different temperatures, and then let the system evolve fitting the evolution of the temperature to the solution of the heat equation. This method is known as Approach-to-Equilibrium Molecular Dynamics (AEMD). It has been developed very recently [51], but some authors have already applied it to calculate the thermal conductivity of Si/Ge nanocomposites [52] and Si nanowires [53], and also of $GeTe_4$ by first-principles molecular dynamics [54].

The following subsections will explain the first and the second methods, the ones used in this Thesis.

2.2.1 Non-Equilibrium Molecular Dynamics

To perform a Non-Equilibrium Molecular Dynamics simulation (NEMD) we can proceed in two different ways: to fix a temperature gradient in the simulation cell and calculate the thermal flux during the evolution of the system, or impose a thermal flux along the system and obtain the temperature profile with the simulation. In our work we use the second method.

To impose the thermal flux we define two different regions in our simulation cell, the sink and the source (as sketched in Fig. 2.1), and after each Verlet step we take an amount of energy from one of the regions and put it in the other. We do that by rescaling the velocities of the atoms located in them as

$$v_{\mathrm{new}}(t) = v_{\mathrm{old}}(t)\sqrt{\frac{E \pm \Delta E}{E}}, \tag{2.26}$$

where E is the energy of the region and ΔE is the energy exchanged each time interval Δt. As we remove in one region the same amount of energy that we add in the other the total energy of the system is not altered by this procedure. This procedure will cause that the region from which we are taking energy gets colder and the region where we are adding it gets hotter. Then in the system the energy will flow from the hot region to the cold region, showing up a thermal flux.

By choosing the amount of energy that the sink and the source exchange we are directly choosing the flux that we are imposing in the system

$$J = \frac{\Delta E}{2A\Delta t}, \tag{2.27}$$

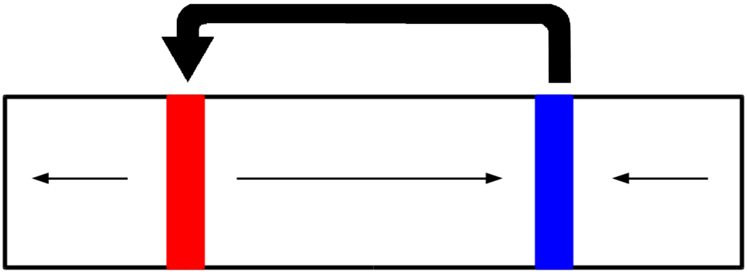

Figure 2.1: *Schematic view of a NEMD simulation. The thick arrow represents that an amount of energy is extracted from the blue region and added to the red region after each step of the algorithm. This cools down the blue region and warms up the red, so in the natural evolution of the system there will be a heat flux going from the hot region to the cold region, represented in the image by the thin arrows.*

where A is the surface that the flow passes through (the cross-section of the sample). The 1/2 factor appears by assuming that the same amount of energy flows to the left and to the right, but this is only true if the two regions of the material between the sink and the source are strictly equivalent.

If we let the system evolve under this condition, after some time it will reach a stationary state, and then we can start the production simulation, the one used to collect data. Defining the temperature of an atom using the definition of its kinetic energy and the equipartition theorem we get

$$E_{kin} = \frac{1}{2}mv^2 = \frac{3}{2}k_B T \Rightarrow T = \frac{mv^2}{3k_B}. \tag{2.28}$$

Averaging it in perpendicular slices to the thermal flux we obtain the temperature profile of the system in the direction of the flux, and we can calculate the temperature gradient $\vec{\nabla} T$ from it. With this we have all the ingredients to calculate the thermal conductivity by the Fourier's law (2.1) using NEMD.

Note that the thermal conductivity obtained in a NEMD simulation is κ_{ii}, the diagonal component of the thermal conductivity tensor in the direction of the thermal flux. Furthermore this value is valid only for the particular length of the system. As in practice a long enough system to obtain the converged value of κ is impossible to simulate, the way to obtain the bulk thermal conductivity using NEMD is to perform some different simulations with different system lengths and extrapolate the value of the thermal conductivity for an infinite system. This is achieved by plotting the inverse of the thermal conductivity $1/\kappa$ against the inverse of the lenght $1/L$ of the system in each simulation, assuming a linear dependance, and taking the value of the linear fit at $1/L = 0$ [55]. The strictness of this procedure have been recently questioned, because this would be accurate only if the minimum system size used in the simulations is comparable to the largest mean-free paths of the phonons that dominate the thermal transport, what is not typically satisfied [56].

2.2.2 Green-Kubo relation

To obtain the Green-Kubo relation for the thermal conductivity we are going to follow the method of Helfand [57] as presented in the book of Massoud Kaviany [58], adding useful information to clarify the derivation, like the explanation using the fluctuation-dissipation theorem or the definition of the microscopic thermal flux. We also present here the Einstein relation and an explanation about how to run simulations using this technique.

The derivation begins with a system in the canonical ensemble. It's energy equation, taking into account that there is not a net flow in the system and that Fourier's law apply, would be

$$nc_v \frac{\partial \rho'(\vec{r},t)}{\partial t} = \nabla \cdot \boldsymbol{\kappa} \cdot \nabla \rho'(\vec{r},t). \tag{2.29}$$

Here n is the number of particles per unit volume, c_v is the specific heat per particle and $\boldsymbol{\kappa}$ is the thermal conductivity tensor. The independent variable $\rho'(\vec{r},t)$ is the deviation of the energy density from its expectation value at position $\vec{r}$ at time t,

$$\rho'(\vec{r},t) = \rho(\vec{r},t) - \langle \rho(\vec{r},t) \rangle, \tag{2.30}$$

where $\rho(\vec{r},t)$ is the actual energy at that point and $\langle \rho(\vec{r},t) \rangle$ is its ensemble average.

Defining the Fourier transform of $\rho'(\vec{r},t)$ as $F(\vec{k},t)$, Eq. (2.29) becomes

$$\frac{\partial F(\vec{k},t)}{\partial t} = -\frac{\kappa k^2}{nc_v} F(\vec{k},t), \tag{2.31}$$

with initial condition $F(\vec{k},0)$. To solve this equation, we multiply it by $e^{\alpha k^2 t}$, (with $\alpha = \kappa/nc_v$), and after some calculations we get

$$F(\vec{k},t) = F(\vec{k},0)e^{-\alpha k^2 t}. \tag{2.32}$$

The fluctuation-dissipation theorem demonstrates that, for a system that satisfies detailed balance, the response to a thermal fluctuation in a physical variable (microscopic) is quantified by the admittance or impedance of the same physical variable (macroscopic), and vice versa. This theorem is the basis of the Green-Kubo method, which connects the previous expressions that include the thermal conductivity (macroscopic) with the correlation function of the microscopic thermal flux. So the next step in the derivation is to find a microscopic expression that could be related with the previous ones.

The energy density of the system on a microscopic level can be defined using a particle basis as

$$\rho(\vec{r},t) = \sum_{j=1}^{N} \epsilon_j(t)\delta[\vec{r} - \vec{r}_j(t)], \tag{2.33}$$

where $\epsilon_j(t)$ and $\vec{r}_j(t)$ are the energy and the position of particle j, and the sum runs over the N particles in the system. We can define the deviation with respect the equilibrium value as

$$\rho'(\vec{r},t) = \sum_{j=1}^{N} \epsilon'_j(t)\delta[\vec{r} - \vec{r}_j(t)]. \tag{2.34}$$

The Fourier transform of (2.34) is

$$F(\vec{k},t) = \int_{-\infty}^{\infty} \sum_{j=1}^{N} \epsilon'_j(t)\delta[\vec{r} - \vec{r}_j(t)]e^{i\vec{k}\cdot\vec{r}}d\vec{r} = \sum_{j=1}^{N} \epsilon'_j(t)e^{i\vec{k}\cdot\vec{r}_j(t)}. \tag{2.35}$$

Multiplying both sides of Eq. (2.32) by $F^*(\vec{k},0)$, the complex conjugate of the initial condition, using (2.35), and taking the ensemble average at the end, gives

$$\langle \sum_{j=1}^{N} \sum_{l=1}^{N} \epsilon'_j(t)\epsilon'_l(0)e^{i\vec{k}\cdot[\vec{r}_j(t)-\vec{r}_l(0)]} \rangle$$

$$= \langle \sum_{j=1}^{N} \sum_{l=1}^{N} \epsilon'_j(0)\epsilon'_l(0) e^{i\vec{k}\cdot[\vec{r}_j(0)-\vec{r}_l(0)]} \rangle e^{-\alpha k^2 t}. \tag{2.36}$$

As we are assuming small perturbations, we can expand both sides of Eq. (2.36) as Taylor series centered in $k = 0$. The calculations are simplified by choosing $\vec{k}$ to be in the x direction, i.e., $\vec{k} = k_x(1, 0, 0)$. After some algebra we find that the zeroth order of both expansions are the same, and also that the first order term is zero, so only the second order term is required. From the second order term the next expression for the thermal conductivity arises:

$$\kappa_{xx} = \frac{1}{2Vk_BT^2t} \langle \left[\sum_{j=1}^{N} [\epsilon'_j(t)x_j(t) - \epsilon'_j(0)x_j(0)] \right]^2 \rangle. \tag{2.37}$$

We could stop the derivation here and work with this last equation for the thermal conductivity. Actually, many authors do that. Eq. (2.37) is known as the Einstein relation for the thermal conductivity, although is typically written as

$$\boldsymbol{\kappa} = \frac{1}{Vk_BT^2} \lim_{t\to\infty} \frac{1}{2t} \langle [\vec{R}(t) - \vec{R}(0)] \otimes [\vec{R}(t) - \vec{R}(0)] \rangle, \tag{2.38}$$

showing explicitly the vector character of the equation and also that the converged value for the thermal conductivity would be found in a long enough time. By comparison of Eqs. (2.37) and (2.38) $\vec{R}$ should be the fluctuation in the energy momentum, but the minus signs allow the value of the energy momentum to be used directly, what is typically done. So

$$\vec{R}(t) = \sum_{j=1}^{N} \epsilon_j(t)\vec{r}_j(t), \tag{2.39}$$

and we will see that this quantity is related with the thermal flux.

This expression for $\vec{R}$ have been obtained in the thermodynamic limit, what means that we are assuming an infinite number of particles in our system. But if one has to perform a simulation using the Einstein relation, it will have a finite number of particles, and $\vec{R}$ will have a bounded behavior, so the time in the denominator of

Eq. (2.38) will cause the thermal conductivity to go to zero. To fix this problem and be able to use the Einstein relation in simulations with periodic boundary conditions, some authors proposed different alternatives, like adding an extra term to the definition of the energy momentum [59], or directly redefine it in a "cumulative way" that makes it increase with time and compensate the $1/t$ [60]. In this last reference, they show that this method is less noisy than the standard Green-Kubo, that the energy momentum can be splitted in kinetic and potential parts, and that the contribution of the potential part is negligible when working with solids. So, their final expression for $\vec{R}$ is independent of the potential, and the distribution of the potential energy between atoms, something that have to be done in the Green-Kubo formalism, can be avoided.

The method of the Einstein relation takes into account the contribution of some images of the system when working with periodic boundary conditions. For this reason, the range of interaction potential should be small enough so that one particle interacts at maximun with only the real or one of the images of any of others [61]. As in this Thesis we are going to work with charged atoms (ions), the coulombic long-range interaction will be present, so we are forced to use the traditional Green-Kubo relation instead of the Einstein relation. We have no other option but to continue with the derivation of the Green-Kubo formula.

To continue we have to note that the sum of Eq. (2.37) can be written as

$$\sum_{j=1}^{N}[\epsilon'_j(t)x_j(t) - \epsilon'_j(0)x_j(0)] = \int_0^t \frac{d}{dt}\sum_{j=1}^{N}[\epsilon'_j(t_1)x_j(t_1)]dt_1, \qquad (2.40)$$

and taking into account the definition of the atomistic heat current explained in Appendix A, we have in the x direction

$$J_x(t) = \frac{d}{dt}\sum_{j=1}^{N}\epsilon_j(t)x_j(t) = \frac{d}{dt}\sum_{j=1}^{N}(\langle\epsilon_j(t)\rangle + \epsilon'_j(t))x_j(t), \qquad (2.41)$$

and since

$$\frac{d\langle\epsilon_j(t)\rangle}{dt} = 0 \qquad (2.42)$$

we can write

$$J_x(t) = \frac{d}{dt}\sum_{j=1}^{N} \epsilon_j'(t) x_j(t). \tag{2.43}$$

Using the equations (2.40) and (2.43) in the expression for the thermal conductivity (2.37), after some calculations we get the well known relation of Green-Kubo for the thermal conductivity

$$\kappa_{xx}(t) = \frac{1}{V k_B T^2}\int_0^t \langle J_x(\tau) J_x(0)\rangle d\tau. \tag{2.44}$$

This equation can also be generalized to obtain any component of the thermal conductivity tensor

$$\kappa_{ij}(t) = \frac{1}{V k_B T^2}\int_0^t \langle J_i(\tau) J_j(0)\rangle d\tau. \tag{2.45}$$

Many things related to this equation have to be mentioned yet. First of all, it is useful to have a better understanding of the heat current $\vec{J}$ that appears in our whole derivation, and of the Heat Current Auto Correlation Function (HCACF) $\langle J_i(t) J_i(0)\rangle$. $\vec{J}$ is a vector that contains the information of the amount and the direction of energy transfer in the system at a certain time. Moreover, autocorrelation is a measure of how a signature of a dynamic system matches a time-shifted version of itself. So the HCACF says how fast changes the microscopic energy transfer in a system, what is also related with the thermal coductivity. A durable correlation means that fluctuations from equilibrium will dissipate slowly, what indicates that the material have a high thermal conductivity. If the correlation lives for a short time, the material we are studying have a low thermal conductivity.

Another important thing is that all the theoretical derivation to obtain the equation has been performed in the canonical ensemble, where we have a fixed temperature and fluctuations in the energy. Nevertheless, when one performs a EMD simulation to obtain the thermal conductivity using Green-Kubo, it is more rigorous to run a NVE simulation (in the microcanonical ensemble) instead of a NVT simulation (in the canonical ensemble). The reason is that the simulation has to satisfy ergodicity to be able to replace the ensemble average of Eq. (2.45) by a time average. The NVE simulation satisfies it, but ergodicity of the Nosé-Hoover thermostat has not been proved. In fact, some authors report that ergodicity is violated in some cases, like in case of small thermostat response times [62]. So a thermostat like the Nosé-Hoover one is only proved to provide correct equilibrium properties, but not dynamical properties such as time correlation functions.

So taking into account all this information, the EMD simulations in this Thesis have been first equilibrated at some temperature using the Nosé-Hoover thermostat, and after that we have run an NVE simulation to produce the heat current data. Very long simulations are required, because to have a truly ergodic system, during the NVE simulation the system have to explore the whole phase space, and explore each point of the phase space many times as the probability density indicates. That is what allows us to replace the ensemble average of Eq. (2.45) by a time average. The longer the simulation time is, the more likely it is that the system have explored the phase space properly, and therefore the more similar will be the time average to the theoretical ensemble average.

As we work with a discrete set of times, it is better to rewrite Eq. (2.45) as

$$\kappa_{ij}(t) = \frac{\Delta t}{V k_B T^2} \sum_{m=1}^{M} \frac{1}{N-m} \sum_{n=1}^{N-m} J_i(m+n) J_j(n). \tag{2.46}$$

In this last formula, Δt is the timestep of the simulation, N is the total number of timesteps in the simulation, M is the number of timesteps we want to include in the time window, i.e., $t = M\Delta t$, and $J_i(m+n)$ is the i^{th} component of the heat current at MD timestep $(m+n)$. We have replaced the ensemble average for a time average. This time average is performed by displacing the origin of time running the n index. The sum over m replaces the integral, and takes into account all the time-separations of the Js. As long is the separation in time of the Js less points we have to average, that is the reason of the $N - m$ denominator, and the explanation of the increase in the error of κ with time. N has to be bigger than M to have enough statistic even in the last point of the time window $m = M$.

A common thought is to think that running a extremely long simulation provides you a lot of long HCACFs to average, wich would result in a good amount of statistic to have a good enough result for the thermal conductivity. With this assumption we just require one long simulation to get the value of the thermal conductivity. However this assumption does not seem to be correct. The Fermi-Pasta-Ulam-Tsingou problem showed that many complicated enough physical systems exhibited almost exactly periodic behavior instead of the expected ergodic behavior. One of the resolutions of this paradox may be that ergodic behavior may depend on the initial energy of the system. If it were the case, running just one long simulation could make us to average some situations that are not uncorrelated. To avoid this problem in this Thesis we have run some different and independent simulations (changing the initial velocities changing the seed of the generator) and we have averaged the values obtained from Eq. (2.46) for the thermal conductivity in all of them. With this kind of simulations one can obtain the whole thermal conductivity tensor, and for a converged size of the system the value obtained is the bulk thermal conductivity of the material.

Chapter 3

Modeling oxides

The studies that have been performed during this Thesis are quite general and can be extrapolated to a wide family of materials, mainly to other functional oxides, but all the simulations presented here have been performed using two materials, Lead Titanate ($PbTiO_3$, abbreviated as PTO) and Zinc Oxide (ZnO). As we have said in Chapter 2, we can avoid dealing with electrons in our simulations because in insulating oxides like these ones the thermal transport is dominated by the dynamics of the lattice. Most of the methods that have been developed to capture the lattice dynamical behavior of materials model the interaction between atoms with an analytic expression, that is typically based in a physical interpretation. For example, we have the well known Lennard-Jones potential [63], that takes into account Pauli repulsion at short ranges due to overlapping electron orbitals with its r^{-12} term, and the van der Waals force with its r^{-6} term. Other common ones are the Tersoff potential [64], the Buckingham potential [65], that can be improved modeling atoms as a core-shell couple [66, 67], and the reactive force fields [68]. These potentials are still used in many works because of its simplicity and because of the possibility to be parametrized for different materials, but are not always able to properly describe the behavior of the materials we want to study, besides they are not always extendible to improve their precision and have a limited predictive power.

On the other hand, we have the most sophisticated methods available to study solid systems, namely first-principles methods. However these methods, even density-functional theory (DFT) [69] that is the most efficient one, are sometimes impractical to use because of the high associated computational load.

Keeping this in mind, Wojdeł et al. have developed an intermediate method [70]. It consists in a second-principles Hamiltonian, what allows to perform classical simulations with many atoms, but parametrized by first-principles calculations, so that it retains the precision and have a predictive power close to the first principles ones.

In this chapter we are going to give information about the PTO and the ZnO and also explain how to model them. ZnO is a simple material, so it can be properly described by the Buckingham potential, an analytical expression that despite its simplicity have been proved to properly describe thermal properties, the piezoelectric constant, and even surface properties of this material [71–74]. PTO is a more sophisticated material, which is reflected in the complexity of the second-principles models we are going to use to describe it. The second-principles Hamiltonian has a demonstrated predictive power for the key structural, vibrational, and response properties of ferroelectric perovskite oxides [75–78], including the PTO.

3.1 PbTiO$_3$

Lead titanate is an inorganic oxide with a perovskite structure. This material is usually represented with the Pb^{2+} cations placed at the corners, the Ti^{4+} cations in the center of the cube, and the O^{2-} anions situated in the center of the faces of the cube, forming an octahedron. At ambient pressure and higher temperatures than the critical temperature $T_C = 760$ K, PTO adopts a cubic structure, but at T_C the material undergoes a phase transition to a tetragonal perovskite structure (see Fig. 3.1).

From a lattice dynamics point of view, the phase transition happens because of the softening of a soft mode [79], a mode whose frequency decreases anomalously when the system goes close to the transition point, where the eigenvalue of the dynamical matrix, i. e., the matrix of the second-derivatives of the energy in the reciprocal space, for this mode have an imaginary frequency. This happens when the anharmonic terms that contributes to the ω^2 of the soft mode (positive) are not able to counter the effects of the harmonic terms that contributes to the ω^2 (negative) sufficiently. In other words, the phase transition results from a delicate balance between long-range

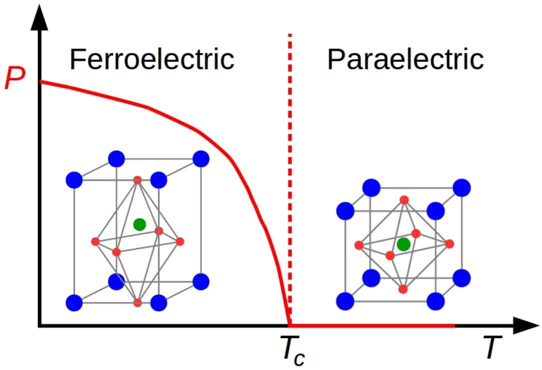

Figure 3.1: *Schematic view of the perovskite structure of the* $PbTiO_3$ *in it's two solid phases. In blue the* Pb^{2+} *cations, in green the* Ti^{4+} *cations, and in red the* O^{2-} *anions.*

electrostatic forces which favour the tetragonal phase and short-range repulsions which favour the cubic phase [80].

The structural distortion that appears at low temperatures has a polar character, and it essentially involves a displacement of the Ti^{4+} and Pb^{2+} cation sublattices against the O^{2-} anions. This distortion can be reversed by an external electric field, so at ambient temperature and pressure PTO is a ferroelectric material.

Pb is more deformable and polarizable than other elements that tipically takes the A place in the ABO_3 perovskite structure [81]. Moreover, as emphasized by Megaw [82] the directional character of the Pb-O bond, possessing a covalent component, could be also responsible for the high Curie point and the large axial ratio, i.e., large c/a, where c and a are the crystallographic axes of the polarized direction and the others respectively.

A PTO crystal in the ferroelectric phase is an ensemble of domains of polarization with different orientations, but these domains can be reoriented applying an strong enough external electric field. In our studies we will choose some different configurations of domains, all of them justified by this property, because they can be obtained experimentally by the application of an external electric field in the region we want to reorient. Between two domains we have an interfase called Domain Wall (DW). This DWs, under some circunstances (angle between the polarization of the domains, temperature,...), can show a spontaneous polarization, that can also be switched by an external electric field, so this interphase behaves like a 2D ferroelectric material [76].

This material and in general ferroelectric materials and perovskites have many different technological applications. For example, many researchers have prepared ferroelectric random access memory (FeRAM) like flexible devices and multi-state memories [83–85], even using organic compounds [86]. PTO is also typically used in the design of these devices [87]. Other option is nanostructure the PTO as thin films for designing infrared sensors based on the pyroelectric effect, as presented in these references [88–90].

We think this family of materials also have promising applications in phononics even though for the moment its role in this field is almost unexplored. In Chapter 4 we study how affects the presence of DWs to a heat flux that goes trough them. The possibility of writing and erasing DWs by means of an strong and instantaneous external electric field makes possible the design of a thermal switch. In the same direction go the studies we have done in Chapter 6, where we use directly the anisotropy of the material to achieve a similar effect. In chapter 5, on the contrary, applying a weaker electric field but constant in time we study how the thermal conductivity of the PTO is affected and how this makes possible to use this material to design a thermal transistor.

3.2 Second Principles Lattice Dynamics

The first step in constructing the model of Wojdeł et al. [70] is choosing a reference structure (RS), usually a minimum or a saddle point of the energy. As the model has to reproduce the structural phase transition of the PTO, a good option is to take the cubic phase as the reference structure, more symmetric than the tetragonal structure of the ground state. To obtain the RS a relaxation imposing the symmetry of the cubic structure using first-principles calculations at $T = 0$ K has to be performed.

The atomic displacements will be studied as relatively small distortions of the RS. So, the position of the atoms are described like this

$$r_{lk\alpha} = \sum_{\beta}(\delta_{\alpha\beta} + \eta_{\alpha\beta})(R_{l\beta} + \tau_{k\beta}) + u_{lk\alpha}, \tag{3.1}$$

where δ is the Kronecker delta, $\boldsymbol{\eta}$ is the homogeneous strain, $\vec{R}_l$ is a lattice vector and l labels cells, $\vec{\tau}_k$ is the position of an atom inside a cell and k labels each atom, and $\vec{u}$ is an individual atomic displacement. α and β denote Cartesian directions.

The energy E is expressed as the energy of the RS E_{RS} plus the energy changes with respect the RS ΔE

$$E = E_{RS} + \Delta E. \tag{3.2}$$

The energy changes around the RS can be expressed as a function of the variables that affect the positions of the atoms as

$$\Delta E(\{\vec{u}_i\}, \boldsymbol{\eta}) = E_{\mathrm{p}}(\{\vec{u}_i\}) + E_{\mathrm{s}}(\boldsymbol{\eta}) + E_{\mathrm{sp}}(\{\vec{u}_i\}, \boldsymbol{\eta}). \tag{3.3}$$

Here, $E_{\mathrm{p}}(\{\vec{u}_i\})$ is the energy change due to the phonons and can be split into the harmonic $E_{\mathrm{har}}(\{\vec{u}_i\})$ and the anharmonic $E_{\mathrm{anh}}(\{\vec{u}_i\})$ contributions, $E_{\mathrm{s}}(\boldsymbol{\eta})$ is the change in the energy when we strain the RS, and $E_{\mathrm{sp}}(\{\vec{u}_i\}, \boldsymbol{\eta})$ is the energy variation occurring when homogeneous strains and atomic distortions appear simultaneously.

The next step is to write these three terms as Taylor expansions. The phononic term becomes

$$\begin{aligned} E_{\mathrm{p}}(\{\vec{u}_i\}) &= E_{\mathrm{har}}(\{\vec{u}_i\}) + E_{\mathrm{anh}}(\{\vec{u}_i\}) \\ &= \frac{1}{2}\sum_{i\alpha j\beta} K^{(2)}_{i\alpha j\beta} u_{i\alpha} u_{j\beta} + \frac{1}{6}\sum_{i\alpha j\beta k\gamma} K^{(3)}_{i\alpha j\beta k\gamma} u_{i\alpha} u_{j\beta} u_{k\gamma} + \cdots \end{aligned} \tag{3.4}$$

where $\boldsymbol{K}^{(n)}$ is a tensor whose components are the n^{th} derivatives of the energy with respect the displacements

$$K^{(n)}_{i\alpha j\beta\ldots} = \left.\frac{\partial^n E}{\partial u_{i\alpha}\partial u_{j\beta}\ldots}\right|_{RS}. \tag{3.5}$$

$\boldsymbol{K}^{(1)} = 0$ because the cubic structure of the PTO is a minimum of the potential energy. It is needed also take into account that the elements of the tensor are not independent and have to accomplish the acoustic sum rules

$$\sum_i K^{(n)}_{i\alpha j\beta k\gamma\ldots} = 0 \qquad\qquad \forall j, k, \ldots, \alpha, \beta, \gamma, \ldots \tag{3.6}$$

to maintain the translational invariance of the system. For the second order we can choose the $K^{(2)}_{i\alpha i\beta}$ as

$$K^{(2)}_{i\alpha i\beta} = -\sum_{j\neq i} K^{(2)}_{i\alpha j\beta}, \tag{3.7}$$

and simultaneously impose the symmetric character of the force-constant matrix

$$K^{(2)}_{i\alpha j\beta} = K^{(2)}_{j\beta i\alpha}. \tag{3.8}$$

As for higher orders imposing the acoustic sum rule is more difficult, a clever idea is to write the anharmonic part as a product of displacement differences

$$\begin{aligned} E_{\text{anh}}(\{\vec{u}_i\}) = \frac{1}{6} \sum_{ij\alpha kh\beta rt\gamma} & \tilde{K}^{(3)}_{ij\alpha kh\beta rt\gamma}(u_{i\alpha} - u_{j\alpha})(u_{k\beta} - u_{h\beta})(u_{r\gamma} - u_{t\gamma}) \\ & + \cdots , \end{aligned} \tag{3.9}$$

which guarantees the translation symmetry and simplify the task of fitting the coeficients by first-principles.

The elastic energy is written as

$$E_{\text{s}}(\boldsymbol{\eta}) = \frac{N}{2}\sum_{ab} C^{(2)}_{ab}\eta_a\eta_b + \frac{N}{6}\sum_{abc} C^{(3)}_{abc}\eta_a\eta_b\eta_c + \cdots \tag{3.10}$$

where N is the number of cells and

$$C^{(m)}_{ab\ldots} = \frac{1}{N}\left.\frac{\partial^m E}{\partial\eta_a\partial\eta_b\ldots}\right|_{RS}. \tag{3.11}$$

The elements $C^{(2)}_{ab}$ are the elastic constants.

Finally, the strain-phonon interaction energy can be written like

$$\begin{aligned}
E_{\mathrm{sp}}(\{\vec{u}_i\},\boldsymbol{\eta}) &= \frac{1}{2}\sum_{a}\sum_{i\alpha}\Lambda^{(1,1)}_{ai\alpha}\eta_a u_{i\alpha} \\
&+ \frac{1}{6}\sum_{a}\sum_{i\alpha j\beta}\Lambda^{(1,2)}_{ai\alpha j\beta}\eta_a u_{i\alpha}u_{j\beta} \\
&+ \frac{1}{6}\sum_{ab}\sum_{i\alpha}\Lambda^{(2,1)}_{abi\alpha}\eta_a\eta_b u_{i\alpha} \\
&+ \cdots
\end{aligned} \tag{3.12}$$

$\boldsymbol{\Lambda}^{(1,1)}$ is the force-response internal strain tensor, and describes the forces that the homogeneous strains causes on the atoms. The $\boldsymbol{\Lambda}^{(m,n)}$ tensors have to satisfy similar acoustic sum rules to the ones that have to fulfill the $\boldsymbol{K}^{(n)}$ tensors, so again a similar procedure can be performed for writing the $E_{\mathrm{sp}}(\{\vec{u}_i\},\boldsymbol{\eta})$ as function of displacement differences

$$\begin{aligned}
E_{\mathrm{sp}}(\{\vec{u}_i\},\boldsymbol{\eta}) &= \frac{1}{2}\sum_{a}\sum_{ij\alpha}\tilde{\Lambda}^{(1,1)}_{aij\alpha}\eta_a(u_{i\alpha}-u_{j\alpha}) \\
&+ \frac{1}{6}\sum_{a}\sum_{ij\alpha kh\beta}\tilde{\Lambda}^{(1,2)}_{aij\alpha kh\beta}\eta_a(u_{i\alpha}-u_{j\alpha})(u_{k\beta}-u_{h\beta}) \\
&+ \frac{1}{6}\sum_{ab}\sum_{ij\alpha}\tilde{\Lambda}^{(2,1)}_{abij\alpha}\eta_a\eta_b(u_{i\alpha}-u_{j\alpha}) \\
&+ \cdots
\end{aligned} \tag{3.13}$$

All the interactions mentioned until now have in principle an arbitrary spatial range, but in practice we will use a cutoff for the spatial extent of such interactions.

The model can be improved considering the symmetries of the system to simplify the Hamiltonian. For example, the displacements of atoms that are equivalent can be grouped in the same coefficient of the Taylor expansion. The authors refer to this symmetry-related products as a symmetry-adapted term (SAT). It also happens that a SAT cancels out, what simplifies even more the potential and the subsequent calculations that will be performed using this model. In our case that we are working with an ABO$_3$ perovskite, they prove that the symmetry of the RS makes zero all the bilinear strain-phonon couplings, i.e., $\boldsymbol{\Lambda}^{(1,1)} = \tilde{\boldsymbol{\Lambda}}^{(1,1)} = 0$.

Another thing that must be taken into account in insulating and semiconductor systems is the electrostatic interaction between ions. As previously said, the interactions of the Taylor expansions described above will be truncated at certain distance, but using a cutoff for the long-range Coulomb interaction introduce significant errors and artificial behavior in a simulation [91]. This is because despite the fact the electrostatic energy appears to be well approximated using a short-ranged approximation, derivatives of the energy do possess distinctively long-range effects. The direct summation method does not take the long-range nature of the derivatives into account [92].

The change in the energy of the RS due to its distortions caused by the electrostatic interaction of the ions must be also taken into account. This effect can be approximated as dipoles that appear when ions are not exactly in their RS positions. Within a linear approximation, the dipoles can be written as

$$d_{i\alpha} = \sum_{\beta} Z^{*}_{i\beta\alpha} u_{i\beta}, \tag{3.14}$$

where $\boldsymbol{Z}^{*}_{i}$ is the Born effective-charge tensor for atom i. These Born charges, as are calculated by first principles, quantifies not only the displacement of the ions but also the rearrangement of the electrons, what in the case of PTO results in charges with a value that is almost twice the value of the charge in the rigid-ion limit.

The lowest order dipole-dipole interactions are captured by the harmonic couplings $\boldsymbol{K}^{(2)}$. In the multipole expansion of the electrostatic energy also exist other harmonic couplings involving other terms. This model neglect their contribution to the long-range part of the energy, and effectively capture their possible effects in the short-range part. The long-range coupling is then written as explained by Gonze and Lee [93], what includes nonanalytical behavior of the phonon bands for homogeneous distortions. In simulations using this model, that typically uses a supercell, the infinite-range interactions can be computed using an Ewald summation.

The procedure we have seen has many advantages:

- It is a general procedure, so the second-principles Hamiltonian can be obtained for any material, not just for the PTO.
- The parameters that appear have a physical interpretation.

- The precision of the potential can be improved in three different ways: taking a higher order in the Taylor expansions, using a longer cutoff for the range of the interactions, and increasing the number of atoms involved in the coupling terms.

The parametrization of this second-principles Hamiltonian can be performed in different ways. The authors distinguish between:

- Parameters computed directly from first principles, like $\boldsymbol{K}^{(2)}$, $\boldsymbol{C}^{(2)}$ and $\boldsymbol{\Lambda}^{(1,1)}$, that quantify the response of the RS of the PTO to small atomic distortions or strains. These parameters can be calculated from density-functional perturbation theory. The Born effective charges are also calculated in this way. To compute the parameters from first principles it is better to use Eq. (3.12) for describing $E_{\mathrm{sp}}(\{\vec{u}_i\},\boldsymbol{\eta})$.

- Parameters fitted to first-principles results, like the higher-order couplings. They implemented an algorithm that adjust the parameters to reproduce first-principles results of the low-energy structures that are more stable than the RS, energy differences and equilibrium atomic configurations. To reproduce specific first-principles results they use Eq. (3.13).

- The parameters that control the dipole-dipole interactions are obtained considering the response of the material to electric fields.

The obtaining and the precision of the second-principles Hamiltonians for different materials have been recently improved by Escorihuela-Sayalero et al. [94], although in this Thesis we work with the old models developed by Wojdeł et al. [70]. In the limit of 0 K, the model for PTO reproduce a spontaneous polarization of 0.99 C m^{-2} and a ratio $c/a \approx 1.07$, very close to the values obtained by extrapolating to low temperatures the experimental results in [95], which are a polarization of 0.85 C m^{-2} and $c/a \approx 1.07$. The model also reproduce, although at a lower temperature than the experimental one, the phase transition of the material, as can be seen in Fig. 3.2 and also detailed in [70]. In fact, it even describes the 2D polarization of the DW between two domains, highlighting its behavior as a ferroelectric in two dimensions, as can be seen in Fig. 3.3 and also detailed in [76].

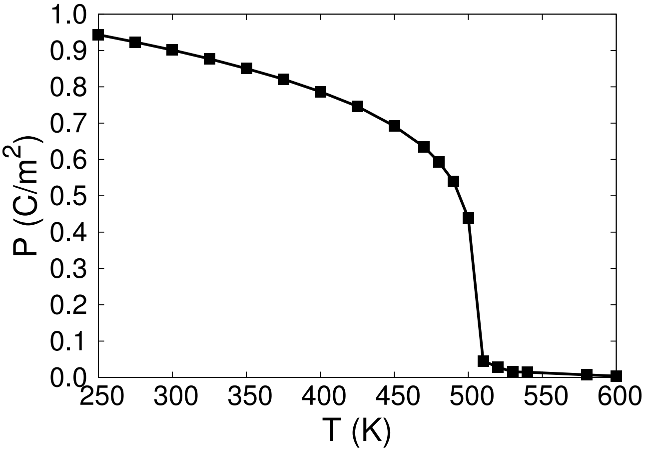

Figure 3.2: *Temperature-dependent polarization of PTO calculated by means of a Monte Carlo simulation for each value of the temperature using* $10 \times 10 \times 10$ *supercells. The transition between the paraelectric and the ferroelectric phases can be appreciated at approximately 510 K.*

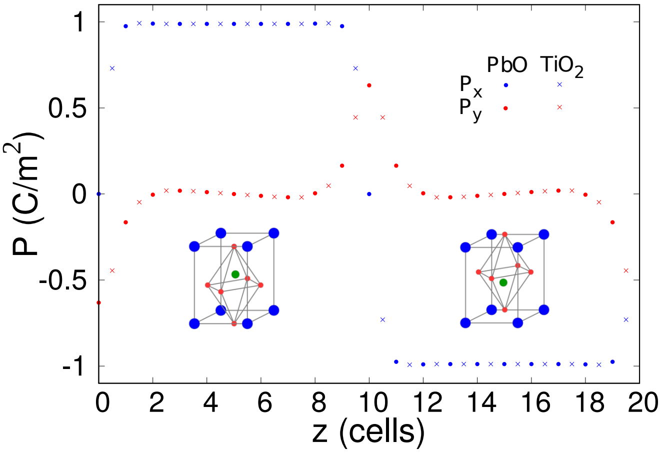

Figure 3.3: *Polarization profile corresponding to the ground state of a multidomain configuration of PTO. The profile has been obtained from a Monte Carlo simulation of a* $12 \times 12 \times 20$ *supercell. It can be appreciated the jump in the polarization when changing from one domain to another of the system* (P_x, *blue), and the spontaneous polarization of the DW* (P_y, *red).*

A program called SCALE-UP (Second-principles Computational Approach for Lattice and Electrons) have been developed to use these models [96]. This code is being continuously improved, but for the moment it can perform Monte Carlo and Molecular Dynamics calculations, tools that are required in this Thesis.

3.3 ZnO

Zinc Oxide is another inorganic material that can be found in three different phases. At normal conditions of temperature and pressure ZnO crystallize in an hexagonal wurtzite structure. Each zinc cation is surrounded by four oxygen anions at the corner of a tetrahedron, and vice versa. In the direction perpendicular to the hexagon, atoms are stacked in an ABAB pattern, as sketched in Fig. 3.4.

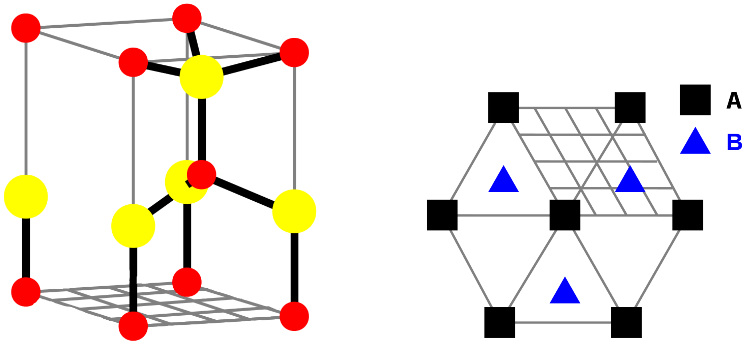

Figure 3.4: *(Left) Wurtzite structure of the ZnO. Zn^{2+} cations are represented in yellow and O^{2-} anions in red. (Right) Here we show an schematic representation of the ABAB stacking in the c direction of the material. The grey grid identifies the same region in each representation.*

This phase transforms to the cubic rock-salt at $\sim$ 9 GPa. The third solid phase of the material is zinc-blende. This phase is metastable and can be stabilized only growing it above cubic substrates [71]. We are interested in the wurtzite phase because is the most common one and the most used for applications. In this phase, by symmetry, the thermal conductivity in the a and b directions of the material will be the same, but different of the thermal conductivity in the c direction.

ZnO was widely used as white pigment for paint and in photocopy paper as a photoconductive ingredient. Nowadays it have been displaced by other materials in these applications, although it can still be found. The rubber industry is now the one that uses the highest amount of ZnO, as a vulcanizing activator [97]. More related with our study are the facts that the ZnO have a high heat capacity, low thermal expansion and high melting temperature, what makes ZnO a nice compound for ceramics [98]. ZnO can be also used in modern and technological applications because many different nanostructures can be synthesized using this material, like nanowires, nanobelts, nanoparticles, etc [99]. For example, Wei et al. developed a glucose sensor based on ZnO nanorods [100], and Solanki et al. have reported a cholesterol biosensor nanostructuring ZnO as films [101].

Also, lattice symmetries of this structure makes ZnO to show a strong piezoelectricity, and also pyroelectricity. Because of that ZnO have a lot of applications. One of the most important ones is the design of devices for use in telecommunications, like resonators and filters. The use of bulk acoustic wave (BAW) and surface acoustic wave (SAW) devices is very extended [102–104]. These devices use the piezoelectric property of ZnO to convert an electrical signal into a mechanical wave in the launching transducer, and conversely, to convert the mechanical wave into an electrical signal at the receiving transducer [105].

We have choosen ZnO to study how thermal conductivity is affected by strain. In this case we are more interested in the fundamental physic relying under the effects than in specific applications. Nevertheless it does not mean the study lacks of interest. In fact, ZnO can be found under strain in many technological applications, like when it is growth as nanowires [106]. Our results can be found in Chapter 7.

3.4 Buckingham potential

To model ZnO we are going to use the Buckingham potential for the short-range interactions, a simple potential with this analytical expression

$$U(r_{ij}) = A \exp\left(-\frac{r_{ij}}{\rho}\right) - \frac{C}{r_{ij}^6}, \tag{3.15}$$

where A, ρ and C are parameters and r_{ij} is the distance between two interacting ions. We are going to take into account also the long-ranged Coulombic interactions between ions

$$U(r_{ij}) = \frac{1}{4\pi\epsilon_0} \frac{q_i q_j}{r_{ij}}, \tag{3.16}$$

where ϵ_0 is the vacuum permittivity and q is the charge of each atom.

The first and second terms on the right-hand side of Eq. (3.15) represent the short-range repulsion and attraction, respectively [72]. To give a physical interpretation to the parameters involved in the potential, we could say that A is related to the "hardness" and ρ to the "size" of the ions, whilst the C term is used to represent the van der Waals interactions [107].

To parametrize the potential, the parameters A, ρ and C are changed iteratively such that they give the best least-squares fit to the experimental lattice parameters, elastic constants and dielectric constant [107]. We have found in the literature two different parametrizations, one made by Binks et al. [108], and other made by Nyberg et al. [73] based upon the original potential of Lewis and Catlow [109]. Both parametrizations seem to provide very close results [72].

In this Thesis we are going to use the Nyberg parametrization. The values of the parameters are written in Table 3.1. We use in our simulations the ionic charges of the Zn and O ions, i.e., +2 and −2 times the absolute value of the electron charge.

	A (eV)	ρ (Å)	C (eV·Å^6)
Zn-Zn	0.0	1.0	0.0
Zn-O	499.6	0.3595	0.0
O-O	22764.0	0.1490	27.88

Table 3.1: *Nyberg parametrization of the Buckingham potential in the Rigid Ion model.*

The lattice constants $a = b = 3.25$ Å and $c = 5.15$ Å of the ZnO wurtzite crystal structure calculated according to the Nyberg parametrization are in fairly good agreement with the experimental values [110] (errors are within 1.5% for both a and c).

For a better understanding of the Buckingham potential we plot in Fig. 3.5 the oxygen-oxygen interaction using for the parameters the values of the Nyberg parametrization.

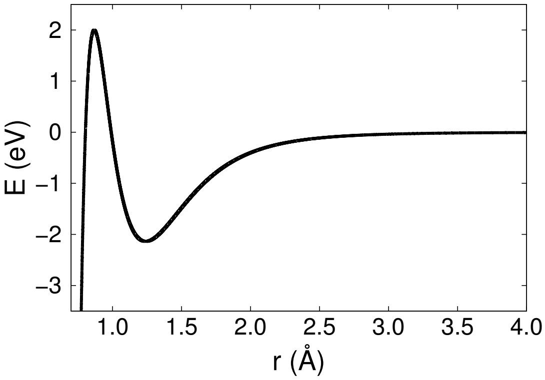

Figure 3.5: *Interaction between two oxygen ions modeled by the Buckingham potential with the parametrization performed by Nyberg et al. [73].*

With this we would have everything we need to model the ZnO with the Buckingham potential. In next paragraphs of the Thesis, as we are treating ions as point particles, we will refer to this model as the Rigid Ion model (RI). But this model can be complemented by distinguishing in the atoms two different parts: the core and the shell [67]. The characteristics of the Core-Shell model (CS) are:

- We assign a charge to the core and the shell of each atom, so that the sum of the two is the charge of the ion. This allows the polarizability of the atom.

- Each core will be linked to its shell by a spring, i.e., by an harmonic term. This will be the only interaction between a core and its own shell, all the other interactions will be excluded.

- Short range interactions are only present in shells. This may seem weird, but as the shell represents the electron cloud it is usual to have all the short-range van der Waals interactions attributed to the shells rather than the cores [111].

- There are also two different versions of the CS model:
    - The first and oldest one includes massless shells that are relaxed after each displacement of the cores [66].
    - The second one uses shells with small mass and their motion integrated in the same way as that of the cores [67]. In this case the frequency of the spring linking the core and the shell should be much higher than the lattice vibrational frequencies. It is always possible to satisfy this condition by making an appropriate choice of the amount of mass we are going to assign to shells, as we can see in the next equation

      $$T_x = 1/f_x = 2\pi\sqrt{x(1-x)M/k},$$

      where T and f are the period and the frequency of vibration, x is the proportion of the ion mass on the shell and $(1-x)$ on the core, M is the total mass of the ion and k is the elastic constant of the spring. Providing that this condition is satisfied, the behavior of the model should be independent of x.

The Nyberg parametrization for the short-range interactions in the CS model is the same that in the case of the RI (see Table 3.1), but in this case the interactions are between the shells [73]. We have to include also the harmonic interaction between the cores and its shells as $V(r_{ij}) = (1/2)kr_{ij}^2$, where for the O_{core}-O_{shell} pair we have $k = 15.52$ eV Å^{-2}, and for the Zn_{core}-Zn_{shell} pair we have $k = 8.77$ eV Å^{-2}. Finally, we have to mention that in this model the charges of the ions does not need to be the formal charges. Although the bonding in ZnO is largely ionic, we can choose partial values to represent bounds that are partially covalent. In our case the charges we are going to use are written in Table 3.2. The electrostatic energy of the system is calculated, as in the case of PTO, by means of an Ewald summation.

Charges	Zn core	Zn shell	O core	O shell
q_i ($\|e^-\|$)	-0.05	2.05	0.00	-2.00

Table 3.2: *Charges of the ions in the CS model.*

The Buckingham potential have been used in many MD simulations for many different materials. For example, in reference [109] authors studied oxides with a CS model and predicted the activation energies for dopant diffusion in NiO, and they also modeled the surface of the MgO and found the rumpled surface previously predicted by Rieder [112] using the exact-exchange Hartree-Fock approach. Moreover they calculated the elastic constant of ternary oxides, in particular those with the spinel and perovskite structures. Their results were generally satisfactory. In reference [113] authors use RI and CS models, and the Green-Kubo technique to study the thermal conductivity of KCl and RbCl-doped KCl, and compare their results with experimental values, obtaining a good agreement between them. To calculate the microscopic thermal flux, they take into account the cores and the shells, as we have done in our simulations of Chapter 7. Focusing attention on the ZnO, which is the material we will study, we have found a study which obtain the piezolectric coefficient for different ZnO nanobelts [74]. It also demonstrated that nanobelts with lateral dimensions smaller than ~ 1 nm undergo significant surface reconstruction relative to their bulk structure, which is consistent with previous reports using a combination of first principles calculations and analytical formulation [114]. In reference [71] authors study the zinc-blende phase of the ZnO in a very special way, modeling the zinc as rigid ions and distinguishing a nucleus and a shell in oxygens. They obtained structural parameters in good agreement with the experimental data, like the lattice constant, and also investigate the $P-V-T$ relationship and many thermal properties as the isothermal bulk modulus and the thermal expansivity. Finally, in this last reference [92] authors use the BTE to compute the thermal conductivity of UO_2, MgO and $SrTiO_3$ using the RI model. The RTA was found to be a very good approximation, only slightly underpredicting the κ compared with the iterative solution.

In this section we have all the theoretical background we need to study the thermal properties of the ZnO, using a potential that has proved its validity in many previous works.

Chapter 4

A phononic switch based on ferroelectric domain walls

Our goal in this Chapter is to design a structure whose thermal conductivity could be dynamically tuned. In particular, a system able to reversibly commute between a low and a high conductivity states, what allows digital signal processing with phonons. To fulfill this purpose, as we have said in Chapter 3, we are going to use the property of the PTO of writing and erasing DWs with an external electric field. This idea has been experimentally observed in different ferroelectrics and DW configurations. First Mante et al. [115] and later Weilert et al. [116, 117] demonstrated that the thermal conductivity of bulk $BaTiO_3$ and KH_2PO_4 can be dynamically tuned by electric field alteration of the density of DWs in the material. However, the effect was demonstrated only at low temperatures, i.e., when phonon-phonon interactions do not become the dominant scattering mechanism. This drawback has been recently overcome with the advent of nanostructured ferroelectrics. Ihlefeld et al. have been able to decrease the DW spacing in ferroelectric thin films made of $Pb(Zr_{0.3}Ti_{0.7})O_3$ below the average phonon mean free path [118, 119], which has made it possible to expand the electrically actuated thermal switch operation over a broad temperature range, including room temperature, thus boosting its potential technological impact.

In spite of the above experimental evidence, a quantitative evaluation of the DWs' resistance to the thermal flux is missing. Alternatively, this relevant magnitude can be estimated by means of atomistic computational simulations of phonon transport. Nevertheless, for the case of ferroelectric DWs, reports of such simulations are scarce [120, 121]. This can be attributed to the fact that large supercells are required in these types of calculations, which hampers the use of accurate ab initio methods, such as density-functional theory (DFT); a second problem relates to the relatively poor transferability and accuracy of the interatomic potential models available nowadays for perovskite oxides. Royo et al. have recently reported a study of phonon transport through ferroelectric DWs with atomistic precision [121]. To this end, they obtained the atomic force constants from second-principles model potentials [70] and performed harmonic (ballistic) phonon transport simulations within the non-equilibrium Green's function formalism. The calculations revealed an unprecedented polarization-dependent phonon scattering mechanism occurring at PTO 180° DWs capable of longitudinally polarizing a thermal flux when piercing several DWs. Yet, the harmonic description employed in that study limits, in principle, the validity of the results obtained at the low-temperature and short-channel situations in which phonon-phonon scattering events can be neglected.

In this Chapter we go beyond this limitation by performing molecular dynamics simulations, where all orders of anharmonicity are included in the description of the lattice dynamics, devoted to investigating phonon transport across ferroelectric DWs in the technologically relevant diffusive regime.

4.1 Details of the simulations

To know how much the presence of DWs affects the heat flux through a sample of PTO we compare the two easiest configurations that we can imagine. The first one is the monodomain case, a supercell in the ferroelectric ground state with all the ferroelectric distortions pointing along the x direction and, thereby, a continuous polarization P_x developed throughout the simulation box. The second one is the configuration with two domains, separated by 180° DWs, which are sharp interfaces that have the same material at both sides but with polarizations in the opposite direction. Both configurations are sketched in Fig. 4.1.

To study these systems we use the second principles Hamiltonian for the PTO described in Chapter 3. We use a $6 \times 6 \times 180$ super-

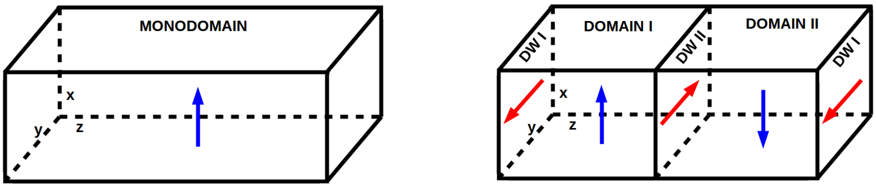

Figure 4.1: *Schematic view of the systems that we simulate. The polarization of the domains are oriented in the x direction, the polarization of the domain walls are oriented in the y direction, and the thermal flux will be imposed in the z direction.*

cell of the 5-atom $PbTiO_3$ unit cell, which corresponds to a total number of atoms of 32400, to a cross-section of 6 nm^2 and a length of 72 nm. The supercell is repeated in all directions using periodic boundary conditions. We perform non-equilibrium molecular dynamics (NEMD) simulations with these two configurations at an average temperature of 200 K. We use this value because a huge temperature gradiend is created in the system using this technique, and it will also suffer many fluctuations in temperature. The spontaneous polarization of the DW is destroyed at temperatures higher than 320 K [76], so we can not guarantee its survival thermalizing the system at ambient temperature, which is what we would have liked to do. As schematically shown in Fig. 4.2, we generate a steady state heat flux along the z axis by injecting a certain amount of kinetic energy in a heat source placed at $z = 0$, which is then removed through a heat sink at $z = L_z/2$, where L_z is the size of the simulation supercell along the transport direction [55]. The resulting heat flux is calculated as we mentioned in Section 2.2, using Eq. (2.27). To have exactly the same at both sides of the sink and the source we place the DWs of the two domains configuration at $z = L_z/4$ and $z = 3L_z/4$ as Fig. 4.2 shows. Notice that, to satisfy periodic boundary conditions, an even number of DWs must be present in the computational cell.

We use a time step of 0.1 fs. Initially, we thermalize the system at 200 K by rescaling the velocities of the atoms for 1 ps. When the system is equilibrated, we start the NEMD run by injecting/extracting a certain amount of kinetic energy in the heat source/sink aplying the velocity rescaling just in these regions, whose size amounts to 5 unit cells along z. The amount of energy injected in one region is the

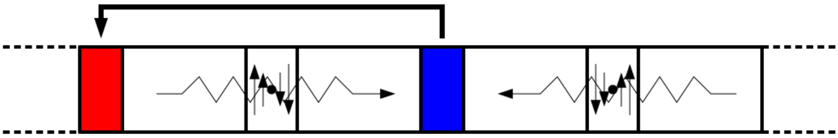

Figure 4.2: *Schematic view of the supercell for a simulation in which thermal transport through two independent DWs is evaluated. The red and blue rectangles illustrate the position of the thermal source and sink, respectively, and the transport directions are indicated with horizontal arrows.*

same than the extracted in the other, so the total energy of the system is conserved. Outside the heat source and sink the system evolves microcanonically. We run 100 ps to reach a non-equilibrium steady state, with $J_z = 6.3 \times 10^{10}$ W m^{-2}, and then average the temperature over the next 200 ps. The global or macroscopic strain, previously determined with a standard equilibrium Monte Carlo calculation at an effective temperature of 200 K, is kept fixed in the NEMD simulation.

4.2 Results and discussion

The simulation of the monodomain case allows us to know the thermal conductivity κ of a piece of PTO of the size that we are simulating. Far enough from the heat source and sink, the averaged temperature profile is linear, as predicted by Fourier's law, with a fitted slope of 4.1 K nm^{-1} as can be seen in red in Fig. 4.3. This estimate, together with the imposed heat flux, allows us to compute the thermal conductivity from (2.1). In this way, we obtain $\kappa = 16$ W m^{-1} K^{-1}, in good agreement with the self-consistent solution of the Boltzmann transport equation [122], using second- and third-order interatomic force constants calculated within the same second-principles model as inputs. Tachibana et al. [123] experimentally reported a lower value of around 6 W m^{-1} K^{-1}. However, they report the existence of complex domain structures in their PTO samples, thus the true thermal conductivity of the monodomain should be larger. On the other hand, finite size effects, which in general bedevil NEMD simulations [55, 56], have a negligible effect in our study because we will focus in the thermal boundary resistance (TBR) of the DWs, which is a local property.

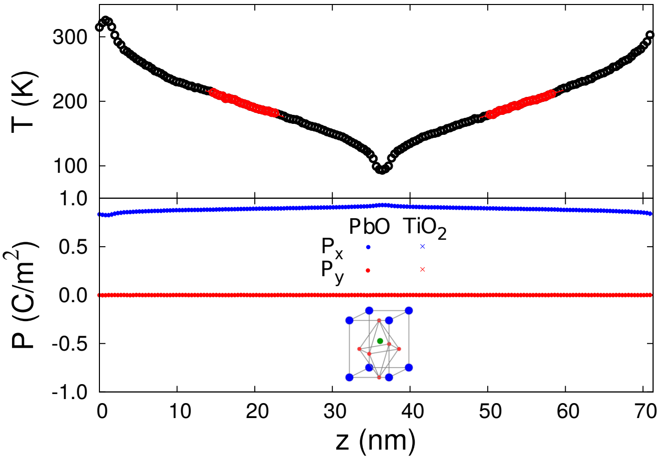

Figure 4.3: *Temperature (top) and polarization (bottom) profiles along the transport direction z for the case of a 72 nm piece of monodomain PTO. Heat flows from the heat source at $z = 0$ to the heat sink at $z = 35$ nm. Data in red are used to fit the thermal gradient. The uniform ferroelectric distortion is sketched in the inset of the bottom panel.*

The TBR will determine the ratio between the thermal resistance of the high and low conduction states, and has thus a pivotal role in the operation of a potential thermal switch. We extract its value from the simulation of two domains. As previously discussed, an even number of DWs is required to satisfy periodic boundary conditions, so each calculation will provide two values of the TBR, assessing the error bar of our estimate.

The temperature profile, shown in Fig. 4.4, features a jump at each DW, the characteristic signature of TBR. A ferroelectric DW is the paradigm of a structurally sharp interface. In reference [76] authors proved that the DW have a width of 1 cell in the limit of 0 K, although in our simulation can be expected to be broader. Notwithstanding, we will treat it in a different way, because even if the width is 1 cell, the presence of the DW affects its surrounding, so we can distinguish in our simulation system between regions that we consider bulk material and the regions that we call interfaces. The polarization and the temperature change rather abruptly, indeed, but they do so within a finite number of layers of material, as shown in the zoomed view of the inset of Fig. 4.4. For this reason, we calculate the TBR

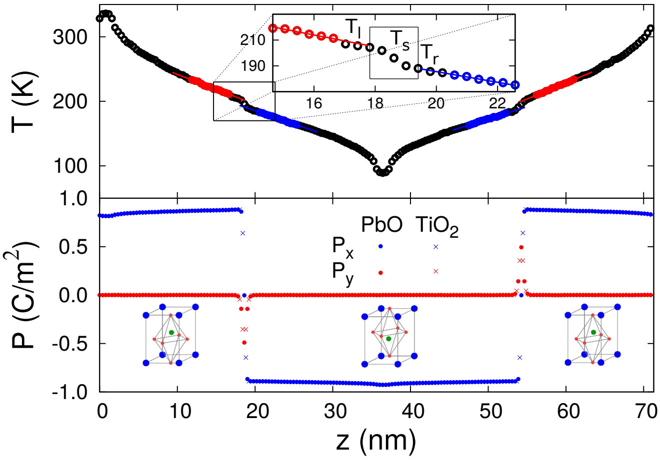

Figure 4.4: *Temperature (top) and polarization (bottom) profiles along the transport direction z for the two domains configuration. Heat source and sink are placed as in Fig. 4.3 and the DWs are at $\sim$ 17 and $\sim$ 52 nm. The inset of the top panel shows a zoomed view of the temperature profile at one of the DWs. The relevant temperatures used to calculate the TBR are indicated.*

within a generalized form of the more common Kapitza resistance formalism (see the Appendix B). We proceed as follows. First, we estimate the interface thickness Δz_{DW} by tracking the spontaneous polarization appearing at the DW [76] and perpendicular to the direction of the ferroelectric distortion P_y. The spontaneous polarization P_x that defines the ferroelectric state might appear to be a sounder choice. However, it varies more abruptly than P_y, thus we believe the latter better captures the nonbulk nature of a layer of material. So, a change in P_y of more than two standard deviations from the reference values (far from the DW and the heat source and sink) identify the interface. We obtain an effective thickness of 5 unit cells (2 nm). Next, we evaluate the DW temperature T_s and the temperatures at the DW boundaries, T_l and T_r (see the inset of Fig. 4.4), and put all of this information in the expression obtained for the TBR in Appendix B,

$$R^{\mathrm{TBR}} = \frac{\Delta T}{J_q}\frac{T_s^2}{T_l T_r}. \tag{4.1}$$

We obtain a value for R_{DW} of 2.9×10^{-10} K m^2 W^{-1}.

We have also calculated the Kapitza length associated to this resistance. Defining it as the ammount of material that have the same thermal resistance as the interface, we get $L_{\text{Kapitza}} = R_{\text{DW}}\kappa = 4.64$ nm, which is approximately the size of 12 cells of PTO.

The presence of a DW amplifies the resistance of the region of material that it occupies, yielding a larger total thermal resistance of the system. Therefore, a DW results in a low conductive state and can be used as the "0" of a phononic binary code. Erasing the DW switches the phononic bit to "1" because the high conductance state is recovered. The ratio between the high and the low conductive states is obtained by dividing the resistance of a segment of material $\bar{L}$ with and without the TBR. In the setup of Fig. 4.3, $\bar{L}$ can be as large as $L_z/4 - \Delta z$, but we take the lower value of $\bar{L} = 15.2$ nm to avoid entering the temperature nonlinear region next to the heat source and sink (see Fig.4.4). For the monodomain case, the resistance of this part of the material would be

$$R^{\text{mono}} = R^{\text{low}} = \frac{\bar{L}}{\kappa_{\text{PTO}}} \approx 9.51 \times 10^{-10} \text{ K m}^2 \text{ W}^{-1}, \tag{4.2}$$

and centering the DW in the simulation with two domains, we have

$$R^{\text{2dom}} = R^{\text{high}} = \frac{\bar{L}_A}{\kappa_{\text{PTO}}} + R_{\text{DW}} + \frac{\bar{L}_B}{\kappa_{\text{PTO}}} \approx 1.12 \times 10^{-9} \text{ K m}^2 \text{ W}^{-1}, \tag{4.3}$$

where $\bar{L}_A + \bar{L}_{\text{DW}} + \bar{L}_B = \bar{L}$. With this choice, we obtain a ratio $R^{\text{high}}/R^{\text{low}} \approx 1.18$. That means that we can increase the thermal resistance of a piece of PTO of 15.2 nm by 18% simply by creating a DW.

M. Royo, one of our colaborators, have also studied the TBR of the DW using the non-equilibrium Green's function (NEGF) method, and at 200 K he have obtained $R_{\text{DW}} \approx 2.8 \times 10^{-10}$ K m^2 W^{-1}, as shows Fig. 4.5 and as presented in our publication [124]. The excellent agreement between the length-independent estimate of NEGF (harmonic) and the NEMD (anharmonic) simulations implies that:

- The TBR is a local property of the DW.
- Anharmonic effects play a negligible role in the DW TBR.

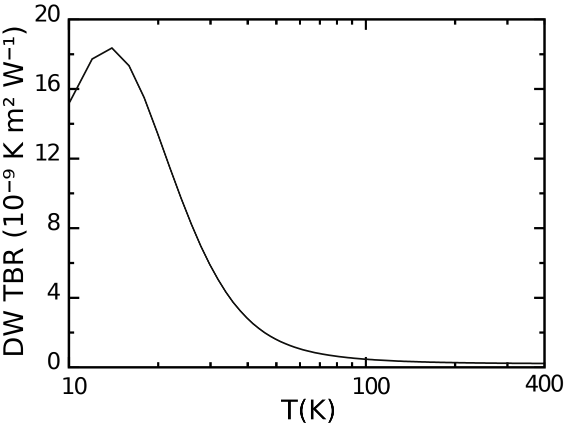

Figure 4.5: *TBR as a function of temperature computed within the harmonic NEGF approach.*

4.3 Increasing the number of interfaces

The possibility of introducing more DWs is very appealing because it would allow increasing the ratio $R^{\text{high}}/R^{\text{low}}$. Therefore, it is interesting to assess to what extent subsequent DWs behave as independent scattering centers with resistances that sum up, a sound assumption in a purely diffusive transport regime [125]. For this reason, we next study the thermal conduction in systems with two DWs. In particular, we consider two cases of DW pairs: In one case, the spacing between them is 1.5 nm, and in the other, 4 nm. We have repeated the procedure described above to define the interface thickness and to calculate the TBR; the final steady state temperature profiles are shown in Fig. 4.6. In the case of the smaller separation, the DWs coalesce, making it difficult to distinguish two separate interface regions; they are thus treated as one single interface complex. Proceeding in this way, we obtain a TBR of 4.7×10^{-10} K m^2 W^{-1}. When the spacing between the DWs is larger, we can treat them individually and we obtain a TBR of 2.3×10^{-10} K m^2 W^{-1} for each one. In both cases we did not appreciate any difference between parallel or antiparallel orientation of the spontaneous polarization P_y occurring at the DW [76].

While, roughly speaking, the thermal resistances of consecutive DWs add up, the obtained TBR per DW is smaller than the value of the individual DW previously calculated. In the low-temperature,

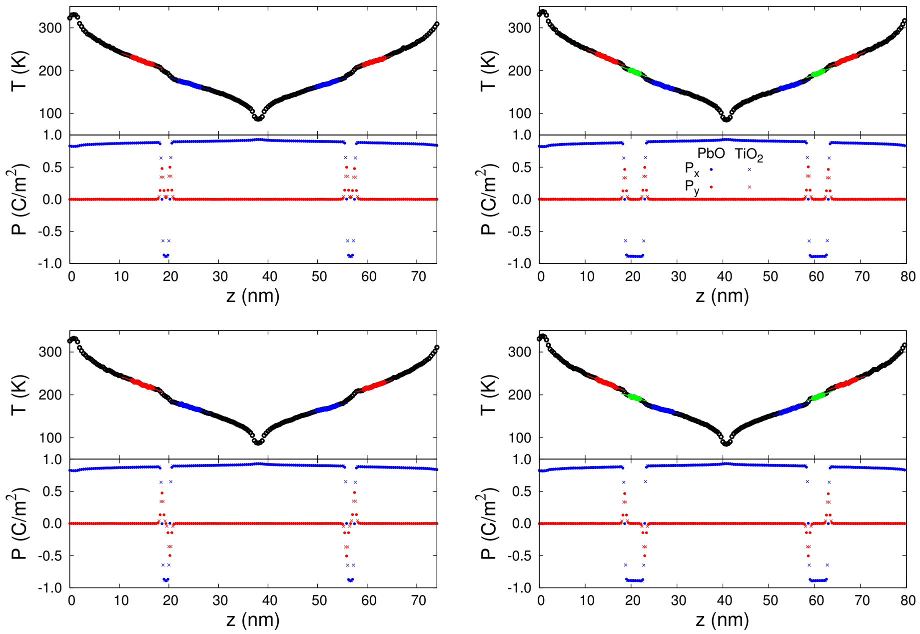

Figure 4.6: *Temperature and polarization profiles along the transport direction* z *for the cases with two DWs separated by* ~ 1.5 *nm (left) and* ~ 4 *nm (right), with the spontaneous polarization* P_y *of both DWs pointing in the same direction (up) and in the opposite (down).*

ballistic transport regime, these DWs have been shown to behave as phonon filters [121] and the presently observed behavior suggests that this effect might partially persist at 200 K and for the specific DW separation considered here. Actually, the total TBR for the system with two separated DWs via NEMD simulations (4.6×10^{-10} K m^2 W^{-1}) is larger than the one obtained from the NEGF harmonic calculations (3.7×10^{-10} K m^2 W^{-1}). These trends in the additivity of the TBRs indicate that the temperatures and dimensions assumed in our NEMD simulations do not entail a completely diffusive transport, although we can appreciate deviations from the harmonic transport regime.

We have calculated the $R^{\text{high}}/R^{\text{low}}$ for the configuration with two DWs taking the same value for $\bar{L}$; the contribution from the TBR is now twice 2.3×10^{-10} K m^2 W^{-1}, while for κ_{PTO}, as in the above discussion for a single DW, we have taken the value obtained in the monodomain configuration. With these assumptions, we obtain a value of 1.26. Therefore, by adding more DWs, the $R^{\text{high}}/R^{\text{low}}$ ratio can indeed become larger, but the increase in the case considered here is moderate. The gain $R^{\text{high}}/R^{\text{low}}$ depends on a delicate balance between design parameters of the system: Well spaced DWs entail a large total R_{DW} (approximately n times the TBR of an individual DW, n being the number of DWs), but also a large $\bar{L}$; conversely, in a series of nearby DWs, $\bar{L}$ can be small, but the TBR per DW could also decrease because of a constructive interference and filtering effect.

4.4 Conclusions

To summarize, in this Chapter we have numerically tested the extent to which the simplest types of ferroelectric DWs occurring in PTO, namely, 180° DWs, behave as barriers for lattice thermal conduction. Our molecular dynamics simulations carried out at relevant temperatures for device operation have shown that the thermal resistance increases by a factor of around 20% due to the presence of a single DW, at the system sizes considered here. This factor can be further increased by incorporating more DWs in the system, though the gain is lower than expected due to the partially nondiffusive nature of thermal transport in the regions between the DWs. We have also demonstrated the local and harmonic character of the DW scattering, as evidenced by the excellent agreement observed among the TBRs from anharmonic NEMD and harmonic NEGF calculations. Our numerical results support the use of ferroelectric DWs as active mobile elements in electrically actuated thermal switches.

Chapter 5

Electric control of the heat flux through electrophononic effects

In the last Chapter we performed non-equilibrium molecular dynamics simulations in PTO, for which we imposed a thermal flux that crossed the Domain Walls of the system. We decided, as typically in thermal transport studies, to assign the z axis to the direction of the thermal flux, and we arbitrarily decided to place the polarization of the different domains in the x axis. In this Chapter we work again with PTO, but as we are not considering any thermal flux, the polarized direction will be the z, that is, $\vec{P} = P_z(0,0,1)$, as typically in ferroelectric studies. Also, the functioning of the thermal switch explained in Chapter 4 was based in instantly turning on and off an external electric field, as an impulse. This allow experimentals to write and erase DWs. In this study the applied field is maintained in time, because is what will cause the distortion of the structure that will modify the thermal conductivity of the material. Having a durable electric field is in principle negative in terms of energy consumption, but it allows us to sweep a continuum of thermal conductivity values, instead of having access to a discrete number of states. Here we consider values of the electric field lower than the coercive field ($E < E_{\text{coe}}$), exploiting the fact that, like most ferroelectric materials, PTO displays a rather large structural (dielectric) response to even moderate applied fields.

5.1 Computational methods

To model the PTO we use again the second-principles Hamiltonian developed by Wojdeł et al. [70] as implemented in the SCALE-UP code [96], as explained in Chapter 3.

For the calculation of the thermal conductivity tensor, we proceed as follows. For each applied field, we first relax the structure by means of a Monte Carlo simulated annealing, automatically accounting for all dielectric and piezoelectric effects that may impact the thermal conductivity [126]. Then, we calculate the second-order interatomic force constants (IFCs) by finite differences in an 8 × 8 × 8 supercell [127]. We use the same supercell to compute third-order IFCs [37], considering interactions up to fourth (twelfth) nearest neighbors for parallel (perpendicular) fields. We then use the IFCs to calculate the anharmonic scattering rates and solve numerically the Boltzmann transport equation (BTE), employing the iterative method implemented in the ShengBTE code [37] on an 8 × 8 × 8 $\vec{q}$-point grid. The choice of the size of the supercell, the number of neighbors in the calculation of the third-order IFCs and the mesh of the reciprocal space are justified in the Appendix C, where we show that these numbers provide good convergence. Scattering from isotopic disorder is accounted for within the model of Tamura [45].

5.2 Expressions for $\boldsymbol{\kappa}$

We calculate the thermal conductivity solving the BTE as explained in Chapter 2, using Eq. (2.10), that we write here for each component of the thermal conductivity tensor

$$\kappa_{ij} = \sum_{\lambda} \kappa_{ij,\lambda} = C \sum_{\lambda} f_{\lambda}^{\mathrm{BE}} (f_{\lambda}^{\mathrm{BE}} + 1)(h\nu_{\lambda})^2 v_{i,\lambda} F_{j,\lambda}, \tag{5.1}$$

where $C^{-1} = k_B T^2 \Omega N$.

Our calculations thus yield κ_{ij} as a function of applied field and temperature, and we fit our results to

$$\kappa_{ij}(T, \vec{E}) = \kappa_{ij}^{0}(T) + \sum_{k} \alpha_{ij,k}(T) E_k + \sum_{k} \sum_{l} \beta_{ij,kl}(T) E_k E_l, \tag{5.2}$$

where we introduce the thermal-response tensors $\boldsymbol{\alpha}$ and $\boldsymbol{\beta}$, κ^0 being the thermal conductivity at zero field. Note that, because of the high tetragonal symmetry of PTO's FE phase ($P4mm$ space group), the number of independent tensor components in Eq. (5.2) is small. For example, we have $\kappa^0_{ij} = \delta_{ij}\kappa^0_{ii}$ and $\kappa^0_{xx} = \kappa^0_{yy} \neq \kappa^0_{zz}$. Here we focus on the behavior of κ_{xx}, κ_{yy}, and κ_{zz} as a function of fields parallel (along z) and perpendicular (along x) to P_z. We thus calculate $\alpha_{xx,z} = \alpha_{yy,z}$ and $\alpha_{zz,z}$, noting that $\alpha_{ii,x} = \alpha_{ii,y} = 0$ by symmetry; and we also calculate $\beta_{xx,xx}$, $\beta_{yy,xx}$, and $\beta_{zz,xx}$, as well as $\beta_{xx,zz} = \beta_{yy,zz}$ and $\beta_{zz,zz}$.

To explore the linear and nonlinear responses, we consider field values in a range up to 90% of the theoretical E_{coe}. Working with an idealized monodomain PTO state with $P_z > 0$, our predicted coercive fields are $E_{\text{coe},z} \approx -1.5 \times 10^8$ V/m (to reverse P_z to $-P_z$) and $E_{\text{coe},x} \approx 8.2 \times 10^7$ V/m (to rotate from P_z to P_x, a symmetry-equivalent x-polarized FE phase). These fields are relatively large when compared with experimental values, an issue that is typical of first-principles works on FE switching [128] and which is probably related, for example, to the absence of nucleation centers for the polarization reversal (defects, interfaces) in the simulations. This matter is not important here. Incidentally, note that it is customary to apply fields as large as these to FE thin films, using voltages of a few hundred meV.

5.3 Results with the (anti)parallel field

Let us discuss first the response to fields $\vec{E} = E_z(0,0,1)$, which can be parallel ($E_z > 0$) or antiparallel ($E_z < 0$) to the electric polarization $P_z > 0$. The parallel field stretch the z direction while shrinks the others, whilst the antiparallel field does the opposite.

Obviously, the change in the structure will affect the phonon bands of the material and in consecuence its thermal conduction properties. Fig. 5.1 shows the phonon dispersion of PTO under no external field and under an electric field of $|E_z| = 0.9 \times E_{\text{coe},z}$ (both parallel and antiparallel to the spontaneous polarization). A parallel (antiparallel) electric field induces a hardening (softening) of all the phonon modes. Thus, the phonon frequencies show a monotonic behavior with the applied electric field. The effect is more patent in the first optical modes, which can vary up to ~ 1 THz before reaching the coercive field value. The acoustic modes account for non-polar vibrational modes of the crystal and are therefore not directly affected by the

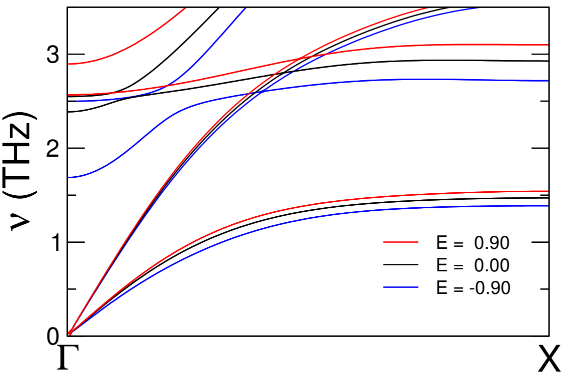

Figure 5.1: *Phonon band structure of PTO along the* $\Gamma - X$ *direction. The red (blue) curve displays the phonon dispersion for* $|E_z| = 0.9 \times E_{coe,z}$ *parallel (antiparallel) to the spontaneous polarization of the material. The black line corresponds to PTO under no external field. A monotonic behavior of all the phonon frequencies with the electric field is found.*

electric field, but rather by the structural deformation induced by it.

Fig. 5.2 shows the thermal conductivity components κ_{xx} and κ_{zz}, as a function of temperature, for different values of E_z. Let us first note that the zero-field conductivities feature a considerable anisotropy, with, for example, $\kappa^0_{xx} = 26.9$ W m^{-1} K^{-1} and $\kappa^0_{zz} = 11.4$ W m^{-1} K^{-1} at room temperature ($T_{\rm room}$). This is a direct consequence of the FE distortion along z, and it suggests that, if the electric field is able to affect the polarization considerably, it will also have a significant effect on the conductivity. This is indeed what we find. As shown in Fig. 5.2, parallel fields yield an increase of both κ_{xx} and κ_{zz}, while antiparallel fields cause a decrease. To better appreciate this effect, we plot the relative variation of the thermal conductivities $\kappa_{xx}/\kappa^0_{xx}$ and $\kappa_{zz}/\kappa^0_{zz}$ in the inset. The most extreme values, i.e., the ones corresponding to the fields of 0.9 in units of the coercive field, are $\kappa_{xx}/\kappa^0_{xx} = 1.12$ and $\kappa_{zz}/\kappa^0_{zz} = 1.16$ in the parallel case, and $\kappa_{xx}/\kappa^0_{xx} = 0.91$ and $\kappa_{zz}/\kappa^0_{zz} = 0.81$ in the antiparallel case.

Further insight can be gathered from Fig. 5.3(a), which shows the variation of both κ components as a function of E_z at $T_{\rm room}$. The obtained smooth behavior can be easily fitted using the quadratic expression in Eq. (5.2). Fig. 5.3(b) shows the T dependence of the corresponding α and β coefficients.

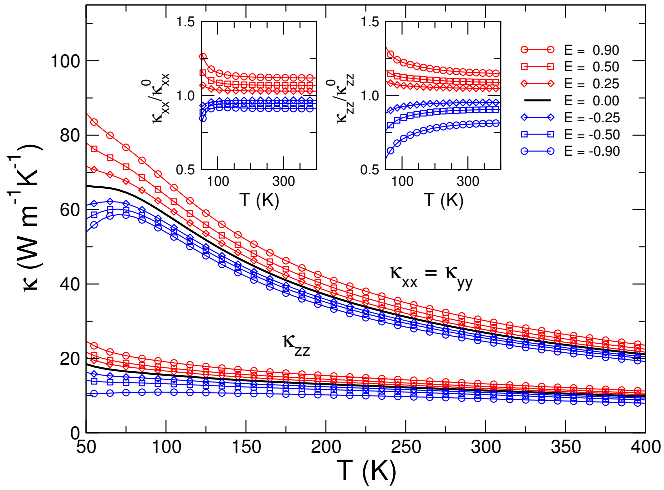

Figure 5.2: *Thermal conductivity as a function of temperature for different values of the parallel ($E_z > 0$) and antiparallel ($E_z < 0$) electric field. The inset shows the relative change of the thermal conductivity as the ratio of its value with and without an external field, $\kappa_{xx}/\kappa^0_{xx}$ (left) and $\kappa_{zz}/\kappa^0_{zz}$ (right). Fields are given in units of the parallel coercive field, $E_{\mathrm{coe},z}$.*

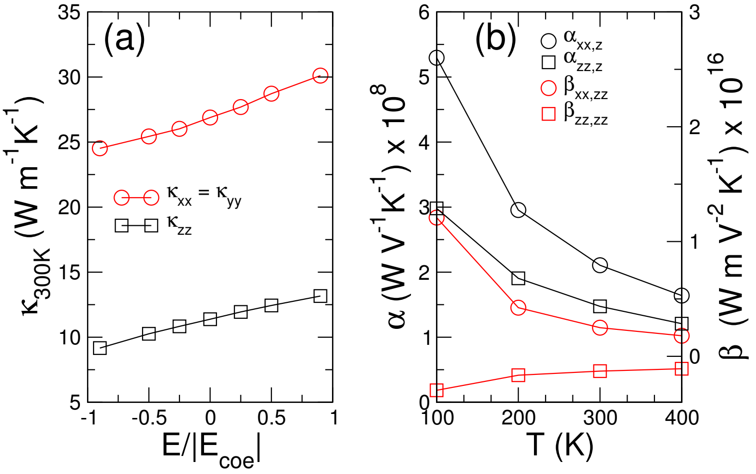

Figure 5.3: *(a) Dependence on the electric field, E_z, of the room-temperature thermal conductivity. (b) Coefficients α and β of Eq. (5.2) as a function of temperature for fields applied parallel to the $\vec{P}$ vector.*

The linear response clearly dominates, with values of $\alpha_{zz,z} = 1.47 \times 10^{-8}$ W V^{-1} K^{-1} and $\alpha_{xx,z} = 2.11 \times 10^{-8}$ W V^{-1} K^{-1} at room temperature. As regards the magnitude of the effect, for $E_z = 0.5 \times E_{\mathrm{coe},z}$ at T_{room} we obtain changes of about 7% and 9% in κ_{xx} and κ_{zz}, respectively. These large effects are ultimately a consequence of PTO's considerable structural response to the applied fields, as evidenced by the variation of P_z shown in Fig. 5.4. The corresponding lattice contribution to the dielectric susceptibility is about 31.

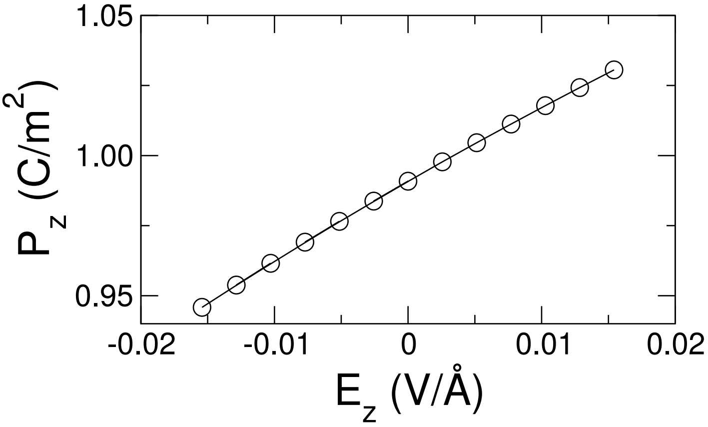

Figure 5.4: *Polarization as a function of a parallel/antiparallel electric field E_z.*

As we have seen, when an electric field is applied antiparallel to the polarization, the latter is first smoothly reduced until a certain critical value of the electric field (coercive field, E_{coe}) is reached. At that value the system reverses its polarization, and thus becomes aligned with the applied field. Since the lattice thermal conductivity of PTO shows a monotonic response to the external electric field, it will show a hysteretic behavior with the latter, as shown in Fig. 5.5. This allows us to devise another application which will be explained in detail in chapter 6.

We have modified the code that we are using to solve the BTE (ShengBTE) to make it print all the values of all the components of the contribution to the thermal conductivity of each mode. With this phonon-resolved thermal conductivity we can go deeper in the understanding of the problem, and we have found that:

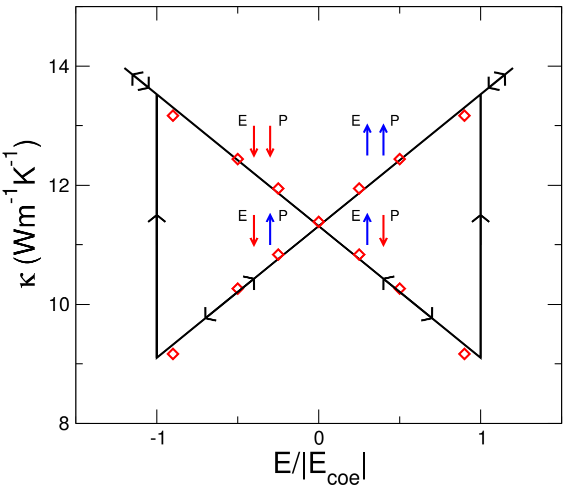

Figure 5.5: *Hysteretic behavior of the lattice thermal conductivity with parallel (and antiparallel) electric fields. The black line with arrows shows the hysteresis loop schematically, while red squares indicate the computed values of κ_{zz} for different values of the external electric field. Blue and red arrows indicate the relative orientations of the applied electric field and the polarization. Note that for $E = E_{coe}$ and the electric field being antiparallel to the spontaneous polarization of the ferroelectric material, the latter reverses its polarization and the electric field becomes parallel to the polarization. On the contrary, for parallel electric fields there is no polarization switching and the lattice thermal conductivity can be further increased (at least up to the breakdown electric field).*

- All the frequencies ν_λ increase with the parallel field, and all of them decrease with the antiparallel field. That also implies that:
  - → As the acoustic modes have $\nu_\lambda = 0$ at $\vec{q} = (0,0,0)$, the velocity of propagation $\vec{v}_\lambda$ of the acoustic modes increase with the parallel field and decrease with the antiparallel field.
  - → As the Bose-Einstein distribution is only a function of ν_λ if we fix the temperature at 300 K, the product $f_\lambda(f_\lambda + 1)$ of each mode decrease with the parallel field and increase with the antiparallel field.

- We can group all the terms that are explicitly dependent on the phonon frequencies by introducing $\theta_\lambda = f_\lambda(f_\lambda + 1)\nu_\lambda^2$. This quantity, that is the frequency-dependent contribution of the specific heat, decrease with the parallel field and increase with the antiparallel field, as we can see in Fig. 5.6.

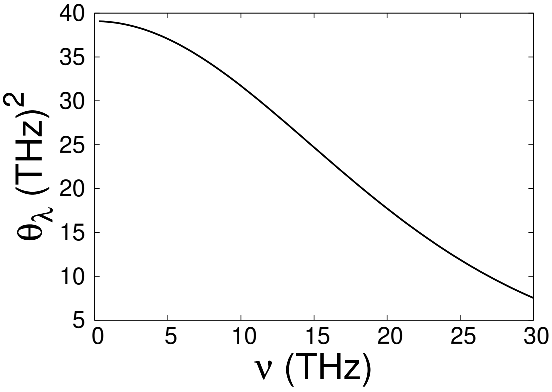

Figure 5.6: *Behavior of the frequency-dependent contribution of the specific heat* $\theta_\lambda = f_\lambda(f_\lambda + 1)\nu_\lambda^2$.

- In average the modes have to increase the product $v_{i,\lambda}F_{i,\lambda}$ with the parallel field, and decrease it with the antiparallel field, because we know that the whole thermal conductivity tensor increases with the parallel field and decrease with the antiparallel field. However this is not satisfied individually by each mode.

We summarize all the information contained in these points in the table 5.1.

	$\vec{E}$ parallel to $\vec{P}$	$\vec{E}$ antiparallel to $\vec{P}$
ν_λ	↑	↓
$f_\lambda(f_\lambda + 1)$	↓	↑
θ_λ	↓	↑
$v_{i,\lambda}F_{i,\lambda}$	∼↑	∼↓

Table 5.1: *Summary of the behavior of all the elements that contribute to the thermal conductivity when PTO is affected by an external electric field.*

We can also calculate the so-called participation ratios, i.e., the contribution to the thermal conductivity of each mode, $\kappa_{ij,\lambda}$, so that:

$$\kappa_{ij} = \sum_{\lambda} \kappa_{ij,\lambda}. \tag{5.3}$$

In Fig. 5.7 we plot $\kappa_{xx,\lambda}$ and $\kappa_{zz,\lambda}$ as a function of the frequency ν_λ in the case of a longitudinal field $|E_z| = 0.5 \times E_{\text{coe},z}$ and compare them with $E = 0$ in the histogram on the right-hand side. As it can be seen, the modes that contribute the most to κ behave as described before, and κ_λ increases (decreases) for parallel (antiparallel) fields.

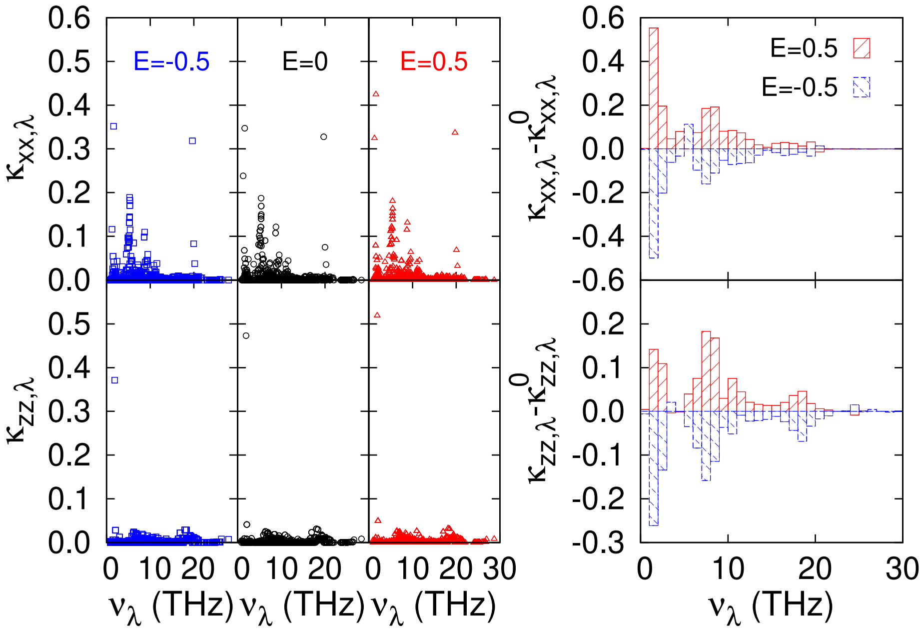

Figure 5.7: *(Left) Contribution of each mode to the thermal conductivity for* $|E_z| = 0.5 \times E_{coe,z}$ *and* $E = 0$. *(Right) Bar charts of the variation of* $\kappa_{xx,\lambda}$ *and* $\kappa_{zz,\lambda}$ *in presence of a parallel field* $|E_z| = 0.5 \times E_{coe,z}$.

To gain even further insight into these results, we find it convenient to analyze Eq. (5.1) writing the field-induced change of κ_{ij} as

$$\begin{aligned}\Delta\kappa_{ij} &= \kappa_{ij} - \kappa_{ij}^0 = \sum_\lambda \Delta\kappa_{ij,\lambda} \\ &= C\sum_\lambda[\Delta\theta_\lambda v_{i,\lambda}^0 F_{j,\lambda}^0 + \theta_\lambda^0 \Delta v_{i,\lambda} F_{j,\lambda}^0 + \theta_\lambda^0 v_{i,\lambda}^0 \Delta F_{j,\lambda} + \mathcal{R}_{ij,\lambda}], \quad (5.4)\end{aligned}$$

where the superscript "0" indicates as previously zero-field quantities, with $\Delta g = g - g^0$ for any magnitude g. This expression (whose mathematical explanation can be found in Appendix D) allows us to readily identify changes that are dominated by only one of the factors (θ_λ,$v_{i,\lambda}$,$F_{j,\lambda}$) entering the mode conductivity, while $\mathcal{R}_{ij,\lambda}$ captures any lingering changes. In the limit of small applied fields, $\mathcal{R}_{ij,\lambda} \to 0$. Further, we can group the changes in the mode conductivities in energy intervals, using the zero-field frequencies to assign specific modes to specific intervals, and thus plot Fig. 5.8 to analyze the E_z-induced changes in κ_{xx} and κ_{zz}.

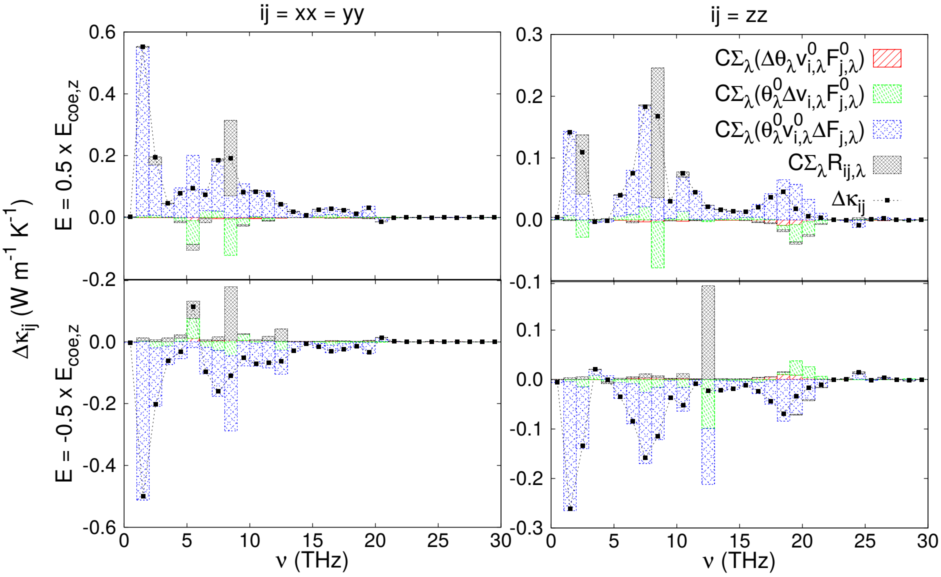

Figure 5.8: *The different terms of Eq.* (5.4) *in the case of a parallel field,* $E_z = 0.5 \times E_{coe,z}$ *(upper row) and of an antiparallel field,* $E_z = -0.5 \times E_{coe,z}$ *(bottom row). The dots indicate the variation of the total contribution to the thermal conductivity, i.e.,* $\Delta\kappa_{ij}$ *in Eq.* (5.4)*, in a given frequency interval.*

Two important observations can be drawn from this figure. On the one hand, the change of κ_{xx} and κ_{yy} does not depend on a particular group of phonons. Rather, the complete spectrum contributes to it, in a way that is rather homogeneous. Thus, for example, we have $\Delta\kappa_{zz} > 0$ for $E_z > 0$, where the total positive change is the result of a majority of phonons having positive $\Delta\kappa_{zz,\lambda} > 0$ contributions. Also, note the approximate symmetry of the results for $+E_z$ and $-E_z$, which is consistent with the dominant linear response. We also observe that, for most of the phonon spectrum, it is the change in mean free displacements that dominates the variation of the conductivity.

We can better understand the changes in $F_{j,\lambda}$ as follows. First, we can simplify our discussion by noting that $F_{j,\lambda} = \tau_\lambda(v_{j,\lambda}\Delta_{j,\lambda}) \approx \tau_\lambda v_{j,\lambda}$, as we observe that the correction to the RTA is small, typically below a 10%. Then, we find that the changes in phonon lifetimes dominate over the variations of the group velocities, which is consistent with the relatively modest impact of the $\Delta v_{j,\lambda}$ term shown in Fig. 5.8. Further, as can be deduced by Eq. (2.12) and Eq. (2.13), $\tau_\lambda^{-1} \sim f_{\lambda'} \times (\nu_\lambda \nu_{\lambda'} \nu_{\lambda''})^{-1}$, where λ' and λ'' label modes that interact with λ via a three-phonon scattering process. Hence, for example, if most phonons were to harden under application of a field $E_z > 0$, the phonon frequencies $\{\nu_\lambda\}$ would generally increase and the populations $\{f_\lambda\}$ decrease, which would yield an increase of the lifetimes $\{\tau_\lambda\}$. As shown before, this is precisely what we have in our calculations, as the average phonon frequency changes from $\bar{\nu}^0 = 9.96$ THz to $\bar{\nu} = 10.05$ THz for $E_z = 0.5 \times E_{\mathrm{coe},z}$, resulting in generally longer lifetimes and larger thermal conductivity. In contrast, for $E_z = -0.5 \times E_{\mathrm{coe},z}$ we obtain $\bar{\nu} = 9.87$ THz, with shorter lifetimes and greater thermal resistance. Indeed, we find that this is the dominant effect explaining our results for κ_{xx} and κ_{zz} under fields that are (anti)parallel to the polarization P_z.

The fact that most of PTO's phonon bands become harder for $E_z > 0$ (softer for $E_z < 0$) may seem surprising at first; yet, we believe it can be rationalized as follows. According to our simulations, the application of a parallel field has two main effects. On the one hand, the cell volume grows moderately. For example, we get $\Omega/\Omega^0 = 1.0018$ for $E_z = 0.5 \times E_{\mathrm{coe},z}$, which is a consequence of a dominant piezoelectric effect. The increased volume alone should result in a general softening (reduction) of the phonon frequencies, which is the usual behavior corresponding to a positive Grüneisen parameter. On the other hand, P_z grows for $E_z > 0$, and the stronger polar distortion can also be expected to have an impact on the phonon frequencies. More precisely, in the field of phase transitions in perovskites, it is generally observed that different distortions of the cubic perovskite structure tend to compete with each other, implying that the condensation of one (for example, the polar distortion) tends to harden the others, thus increasing the associated phonon frequencies (see Refs. [70, 129]). Our results suggest that this effect is dominant in PTO.

Since we attribute the changes in thermal conductivity under E_z field to a general hardening/softening of the phonon spectrum, it may seem strange to note in Fig. 5.8 that the changes associated with the $\Delta\theta_\lambda$ term [Eq. (5.4)] are negligible (in fact, they are barely visible in the figure). However, note that, in this term, the variations of frequencies and populations tend to cancel each other, yielding a relatively small net effect.

5.4 Results with the perpendicular field

Let us now move to the case in which we apply a field $\vec{E} = E_x(1,0,0)$, perpendicular to the polarization, P_z. We consider $E_x > 0$, noting that this situation is equivalent by symmetry to the application of $E_x < 0$ or fields along y. Fig. 5.9 summarizes our results, which feature a very large decrease of all the tensor components.

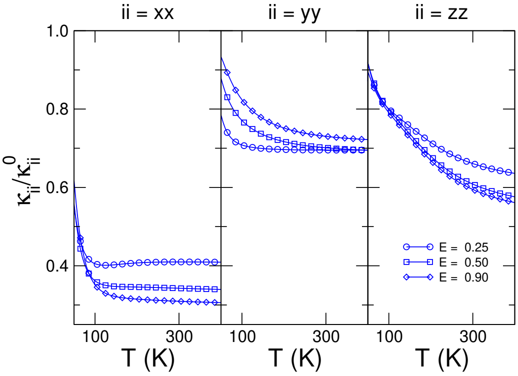

Figure 5.9: *Ratio of the thermal conductivity with and without a perpendicular external field, $\kappa_{xx}/\kappa^0_{xx}$ (left), $\kappa_{yy}/\kappa^0_{yy}$ (center), and $\kappa_{zz}/\kappa^0_{zz}$ (right), as a function of temperature.*

Thus, for example, for $E_x = 0.25 \times E_{\mathrm{coe},x}$ at T_{room}, we get $\kappa_{xx}/\kappa^0_{xx} = 0.41$, $\kappa_{yy}/\kappa^0_{yy} = 0.70$ and $\kappa_{zz}/\kappa^0_{zz} = 0.66$. This dramatic enhancement of the thermal resistance translates into very large values of the quadratic response β, as we obtain $\beta_{xx,xx} = -1.39 \times 10^{-12}$ W m V^{-2} K^{-1}, $\beta_{yy,xx} = -2.26 \times 10^{-13}$ W m V^{-2} K^{-1} and $\beta_{zz,xx} = -6.51 \times 10^{-14}$ W m V^{-2} K^{-1} at T_{room}.

In the case of a perpendicular field, the analysis of the contribution to the thermal conductivity of the individual modes reveals the frequency regions where the reduction of κ occurs. In particular, as we can see in Fig. 5.10, while the decrease of κ_{xx} and κ_{yy} mostly originate from a reduction of the contribution of modes with $\nu_\lambda \sim 5$ THz, κ_{zz} features also a significant decrease of the contribution of modes at higher frequencies, $\nu_\lambda \sim 20$ THz.

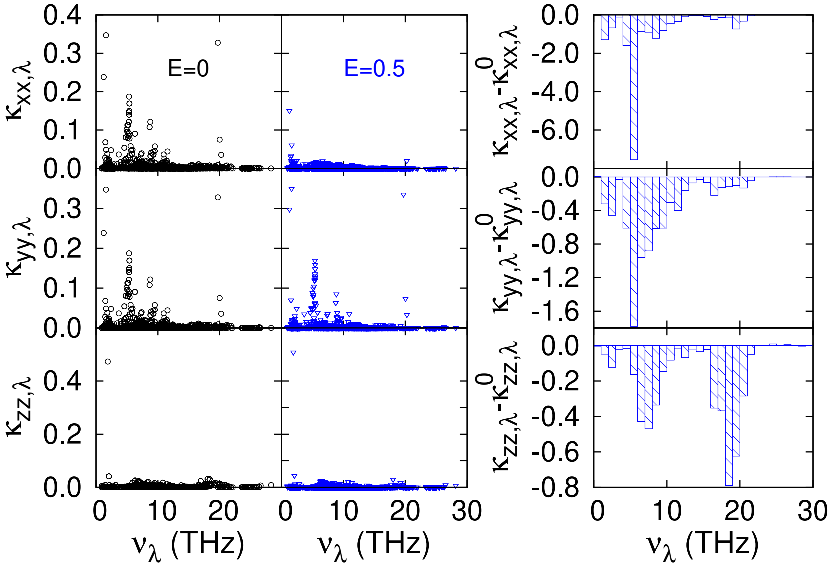

Figure 5.10: *(Left) Contribution of each mode to κ_{xx}, κ_{yy}, and κ_{zz} (top to bottom) for a perpendicular field $|E_x| = 0.5 \times E_{\mathrm{coe},x}$ and $E = 0$. (Right) Bar charts of the variation of $\kappa_{xx,\lambda}$, $\kappa_{yy,\lambda}$ and $\kappa_{zz,\lambda}$ in presence of a perpendicular field $|E_x| = 0.5 \times E_{\mathrm{coe},x}$.*

Fig. 5.11 shows the analysis based on Eq. (5.4), applied to the change in κ_{xx} at T_{room} for a field $E_x = 0.5 \times E_{\mathrm{coe},x}$, which is a representative case. As above, we find that the total $\Delta\kappa_{xx}$ is the result of

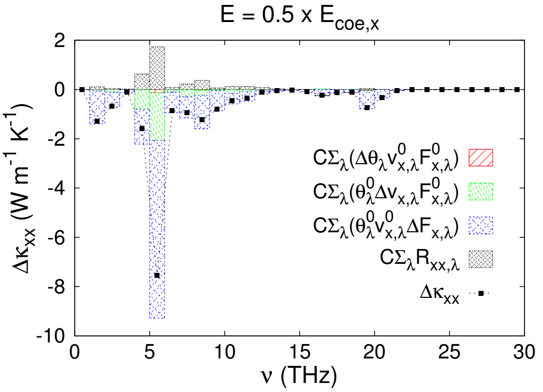

Figure 5.11: *The different terms of Eq.* (5.4) *in the case of a perpendicular field,* $E_x = 0.5 \times E_{coe,x}$*. The dots indicate the variation of the total contribution to the thermal conductivity in a given frequency interval, i.e.,* $\Delta\kappa_{xx}$ *in Eq.* (5.4)*.*

contributions spanning the whole phonon spectrum, and dominated by the changes in mean free paths. Also as above, we find that it is the change in the phonon lifetimes that controls $\Delta F_{j,\lambda}$; yet, at variance with the case of the E_z fields, the present effect cannot be attributed to a general shift of frequencies. Indeed, we find that the E_x field tends to harden the phonon spectrum (for example, we obtain $\bar{\nu} = 10.02$ THz for $E_x = 0.5 \times E_{\mathrm{coe},x}$). According to our above argument to explain the response to E_z fields, the larger frequencies should result in longer lifetimes and an increased conductivity; yet, the effect of the perpendicular fields is just the opposite, with increased resistivity. Interestingly, a further analysis of our results reveals that, in this case, the field dependence of the lifetimes is dominated by the three-phonon scattering matrix $V^{\pm}_{\lambda\lambda'\lambda''}$, which controls the phonon decay as $\tau_\lambda^{-1} \sim |V^{\pm}_{\lambda\lambda'\lambda''}|^2$ (see Eqs. (2.12), (2.17) and (2.18)). More specifically, we find that the E_x field activates a large number of new scattering processes due to the symmetry breaking that it causes, i.e., it broadens the phase space for anharmonic scattering. As an E_z field does not change the symmetry of PTO's P_z-polarized phase, the proliferation of scattering events does not occur in that case (see Fig. 5.12). This effect affects the whole phonon spectrum, and its magnitude naturally scales with the structural symmetry breaking caused by E_x, which is rather considerable given the large dielectric response of PTO to

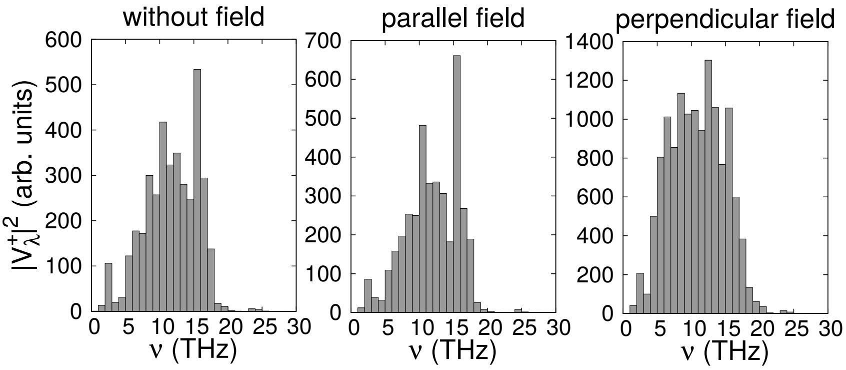

Figure 5.12: *Distribution in frequencies of the square of the three-phonon scattering matrix of the absorption processes* $|V^+_{\lambda\lambda'\lambda''}|^2$ *in the cases without (left), with a parallel (center) and with a perpendicular (right) electric field.*

such a perturbation (for the corresponding susceptibility, we obtain $\chi_{xx} \approx 304$; see Fig. 5.13). Such a strong response to a transversal field is related to the "easy polarization rotation" that is well known in FE perovskite oxides [130, 131].

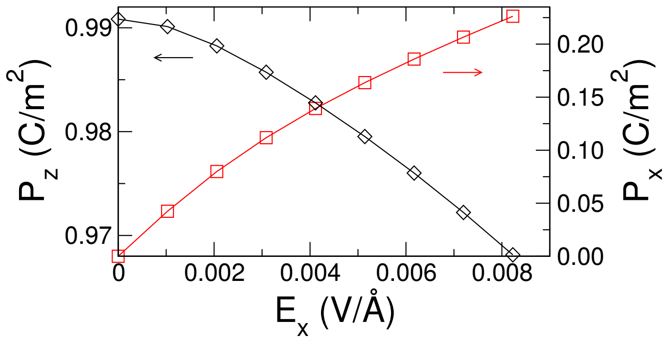

Figure 5.13: *Polarization as a function of a perpendicular field* E_x. *We display both* P_x *and* P_z, *whose increase/decrease allows us to appreciate the rotation of* $\vec{P}$.

Interestingly, we also observe a field-induced coupling of the x and z directions (those along which the initial $\vec{P}$ and the applied E_x field are oriented) in the thermal conductivity tensor. We obtain values of κ_{xz} and κ_{zx} that are not negligible, of the same order of those in porous [132, 133] or amorphous [134] materials. Their temperature dependence for applied fields is shown in Fig. 5.14.

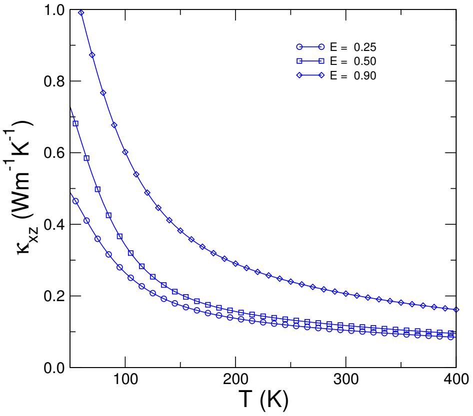

Figure 5.14: *κ_{xz} as a function of temperature for different values of perpendicular electric fields. Fields are given in units of the perpendicular coercive field, $E_{coe,x}$.*

These nonzero components imply that, for example, a thermal gradient along x results in a heat flux, not only along x but also along z, and viceversa.

5.5 Conclusions

In conclusion, we have reported evidence of the coupling between an electric field and thermal conductivity in a ferroelectric perovskite. We have shown that an electric field perpendicular to the spontaneous polarization greatly increases the thermal resistivity, the underlying physical mechanism being the breaking of the symmetry of the lattice, which activates new scattering processes with a concomitant reduction of the lifetimes of phonons throughout the vibrational spectrum. On the other hand, for parallel fields that do not activate new scattering processes, we observe a linear variation of the thermal conductivity, which can grow or decrease depending on the sign of the applied field. This linear effect is controlled by the overall hardening/softening of the phonon modes. The predicted behaviors open the way to a fully electric control of phonon transport. As the underlying physical principle is the manipulation of polar modes, these results can potentially be extended to a broader class of materials, possibly with even larger responses. Finally, we note that the symmetry breaking that leads to the largest changes in the thermal conductivity can also be achieved in other ways, such as mechanical strains, that do not involve electric fields.

Implementations of these concepts in a realistic device will have to take into account that substrates and additional layers will provide alternative heat transport channels and that the thermal contact resistance [135, 136] may complicate our taking advantage of the controllable transport properties of the ferroelectric layer. In Chapter 7 we present a study related with this issue, in which the thermal conductivity of bulk ZnO is tuned by means of the application of external strain.

Chapter 6

Anisotropy-driven thermal conductivity switching and thermal hysteresis in a ferroelectric

In Chapter 4, by means of writting and erasing Domain Walls using an instantaneous impulse of an external electric field, we found that is possible to implement a phonon-based Boolean algebra. In that case the monodomain of PTO acts as the high conductance state and the multidomain as the low conductance state. In this Chapter we discuss an even simpler effect, namely, how an electric field can be used to rotate the polarization in a monodomain and, consequently, gain access to a different element of the thermal conductivity tensor within a given device setup, thus implementing a thermal switch. As we discuss below this approach does not require the design of complex multidomains and only relies on the anisotropy of the thermal conductivity in the monodomain state.

Our study is based again on PTO, modeled with the second-principles Hamiltonian developed by Wojdeł et al. [70] as implemented in the SCALE-UP code [96], as we explained in Chapter 3. We also use the BTE to obtain the thermal conductivity of the system proceeding exactly in the same way of Chapter 5.

6.1 Hysteresis cycle of the $\boldsymbol{\kappa}$

As we have seen in previous Chapters, the thermal conductivity tensor of $PbTiO_3$ in the ferroelectric ground state has two independent components and has the form

$$\boldsymbol{\kappa} = \begin{pmatrix} \kappa^{\perp} & 0 & 0 \\ 0 & \kappa^{\perp} & 0 \\ 0 & 0 & \kappa^{\parallel} \end{pmatrix}, \tag{6.1}$$

where $\kappa^{\perp}$ and $\kappa^{\parallel}$ are the thermal conductivities that account for heat transport when phonons flow perpendicular or parallel to the polarization $\vec{P}$. We have decided to use this notation in this Chapter because we are going to describe the hysteresis cycle of the thermal conductivity, which implies external electric fields acting in different directions, sometimes parallel and at other times perpendicular to the polarization of the system. In addition, the relevant component of the thermal conductivity tensor will change from one stage to another, so working with Cartesian axes is more confusing.

The computed values of the thermal conductivity are plotted in Fig. 6.1, where it is easy to see that $\kappa^{\perp}$ is larger than $\kappa^{\parallel}$ throughout all the temperature range investigated.

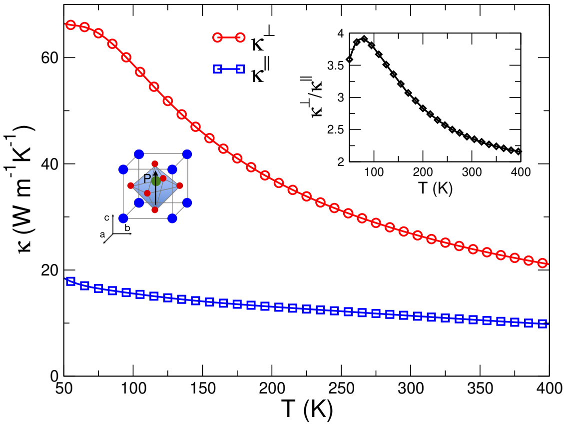

Figure 6.1: *Thermal conductivity as a function of temperature of PTO in the ferroelectric ground state along the c-axis and parallel to the polarization,* $\kappa^{\parallel}$*, and in the ab-plane and perpendicular to the polarization,* $\kappa^{\perp}$*. The ratio* $\kappa^{\perp}/\kappa^{\parallel}$*, which quantifies the thermal anisotropy of PTO, is shown in the inset.*

The anisotropy, $\kappa^{\perp}/\kappa^{\|}$, is larger at low temperatures (with a peak value of $\sim$ 4 at 100 K), as shown in the inset of Fig. 6.1, but at room temperature it is still larger than 2. This anisotropy can be used to implement a thermal switch, as schematically illustrated in Fig. 6.2: phonons that propagate along the x-axis will experience a large thermal conductivity $\kappa^{\perp}$ when $\vec{P}$ is oriented along y or z, while the conductivity will be lower and equal to $\kappa^{\|}$ when $\vec{P}$ is parallel to the heat transport direction, x. Commutation between the two conductance states is achieved with a rotation of the polarization (which is equivalent to a rotation of the lattice/sample) by means of an electric filed that acts as the gate control signal.

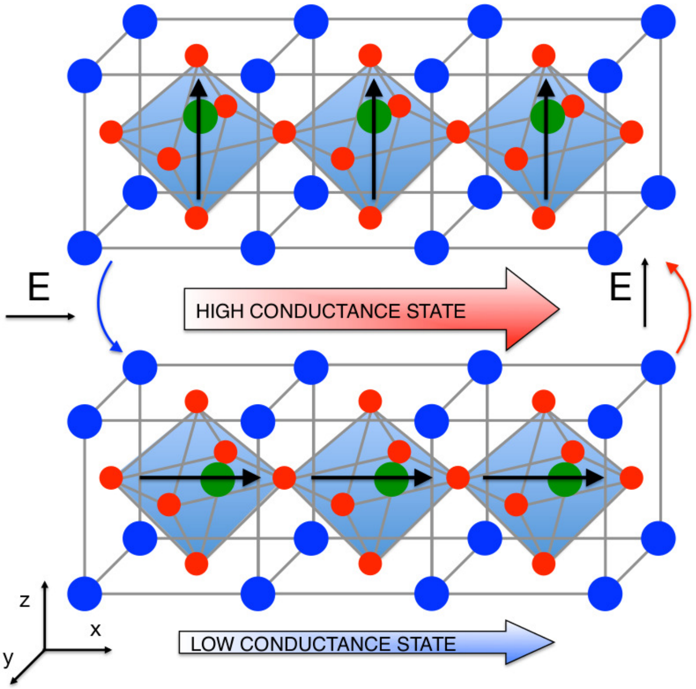

Figure 6.2: *Sketch of the thermal switch. In the high conductance state phonons flow along a direction perpendicular to* $\vec{P}$ *and the thermal conductivity is* $\kappa^{\perp}$. *In the low conductance state phonon flow parallel to* $\vec{P}$ *and the thermal conductivity is* $\kappa^{\|}$. *An electric field along the* x- *or* y-*axis rotates* $\vec{P}$ *and triggers the commutation from high-to-low conductivity, while an electric field along the* z-*axis triggers the low-to-high conductivity transition.*

We now take a closer look at the way the thermal conductivity switches between the low and the high state. We have calculated the thermal conductivity of intermediate situations applying different values of the external electric field. The values we propose would be valid assuming the process is adiabatic, i.e., in the limit of very slow variations of $\vec{E}$ we can assume to be always in equilibrium and thus we can define and calculate the thermal conductivity. In practice, obviously the process will not be adiabatic, and these values will be more realistic the slower the variation of the field.

The whole process of switching can be described as follows. We take as initial state the one with the polarization parallel to the phonon flow, that is, the low conductivity state. Then we start to apply a perpendicular electric field of increasing strength: $\vec{P}$ starts precessing and the conductivity is reduced (curve 1a in Fig. 6.3); this is a result of the field-induced lowering of the lattice symmetry, which increases the phase-space for three-phonon scattering events, discussed in Chapter 5. When the coercive field E_{coe} is reached, the polarization switches (curve 1b in Fig. 6.3) and becomes parallel to the electric field. If now the electric field is reduced until it vanishes (curve 2 in Fig. 6.3) a ground state equivalent to the starting configuration is reached. Now, however, $\vec{P}$ is perpendicular to the direction of phonon propagation and the system is in the high conductivity state. To rotate back the polarization we start applying an electric field along x, the direction of the heat flow: like before, κ decreases until $\vec{P}$ switches (curves 3a and 3b in Fig. 6.3). Finally, upon removal of the electric field (curve 4 in Fig. 6.3) we recover the starting configuration. As it can be seen, the value of κ in the direction of the phonon propagation follows a hysteresis cycle, and it can take different values at a given electric field, depending on how the field changed in the past. This is a direct consequence of the fact that given a value of $\vec{E}$ one cannot univocally know $\vec{P}$, which ultimately determines the thermal conductivity along a given direction.

The hysteresis cycle described in Fig. 6.3 can be compared with the one represented in Fig. 5.5. The more complex cycle described in this Chapter is created by applying the electric field in two different directions, while the hysteresis of Fig. 5.5 appears just for (anti)parallel fields to the polarization. This new version allow us to change between the different components of the thermal conductivity tensor,

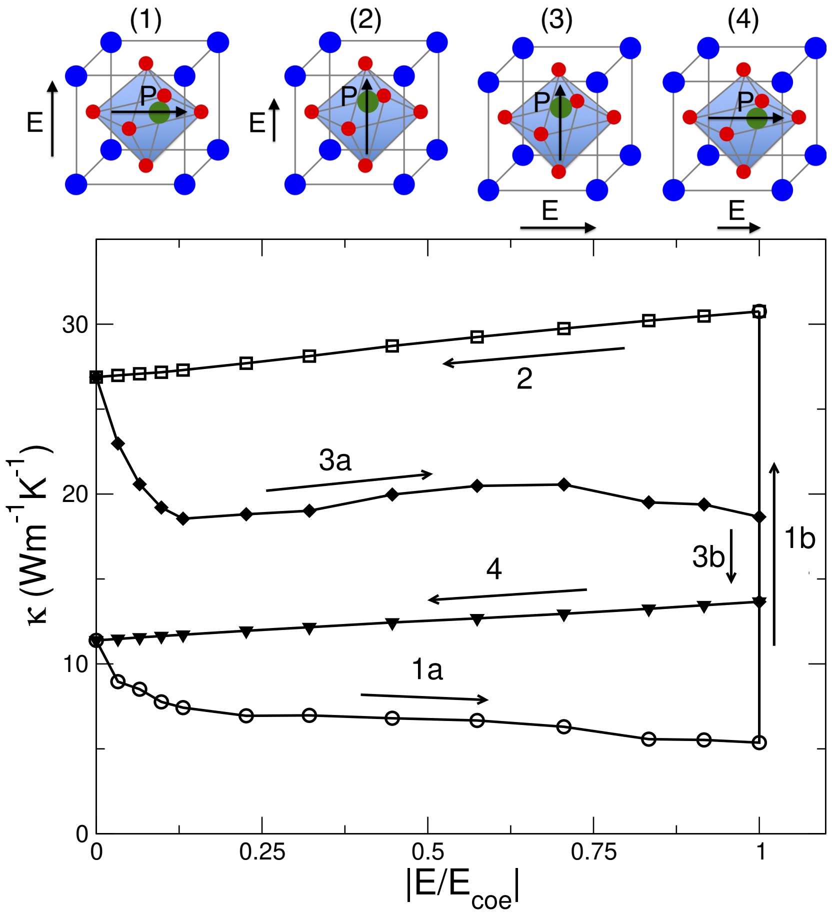

Figure 6.3: *Hysteresis cycle followed by the thermal conductivity in the direction of the phonon propagation when the polarization is rotated back and forth at 300 K. The sketches in the upper part of the figure depict the direction of the electric field (polarization), throughout (at the beginning of) the corresponding branch of the* $\boldsymbol{\kappa}(\vec{E})$ *curve; long (short) arrows indicate increasing (decreasing) values of* $\vec{E}$.

making more extreme values accessible.

The relation between $\vec{E}$, $\vec{P}$, and $\boldsymbol{\kappa}$ is more clearly illustrated in Figure 6.4 where one full hysteresis cycle is displayed as a function of time, which is assumed to vary conveniently slow to allow us to consider the transition adiabatic and the system in instantaneous equilibrium. Like in Fig. 6.3 $\vec{P}$ is initially taken to lie along the x-axis, so

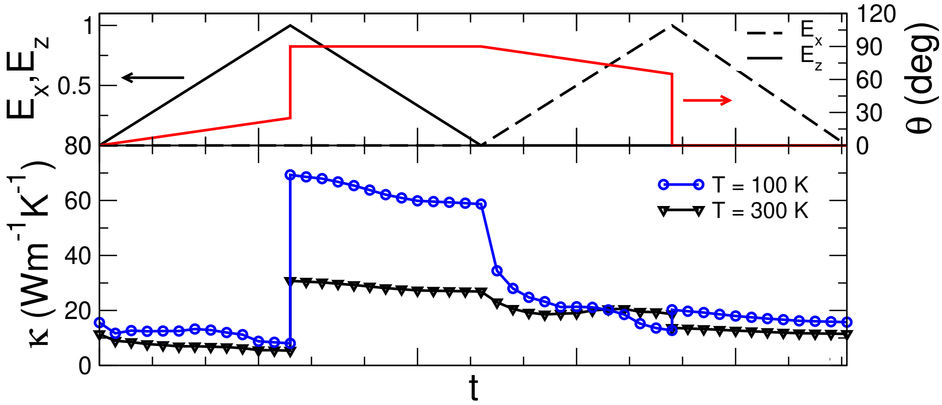

Figure 6.4: *Thermal conductivity as a function of time* $\kappa(t)$ *at* $T = 100$ *and 300 K in response to the variation of the electric field, whose component* E_x *and* E_z *are plotted in the upper panel in unit of the coercive field* E_{coe}*. The angle* θ *formed by the polarization vector and the direction of the heat flux is also shown.*

that the system is in the low conductance state and an electric field E_z must be applied to rotate the polarization and switch to the high conductance state. This plot highlights the role of temperature in determining the difference between the two conductance states, which is much larger at lower temperature, as already shown in the inset of Fig. 6.1.

6.2 Relaxation time of the commutation

In the discussion above the electric field was varied with slow ramps, so that the transition could be considered adiabatic, the system was always in equilibrium and $\boldsymbol{\kappa}$ could be computed all along the hysteresis cycle. Of course one would like to commute between 1 and 0, i.e., high- and low-conductance, as quick as possible and thus would rather use short electric field pulses to rotate the polarization. Although $\boldsymbol{\kappa}$ cannot be calculated in these (strongly) out-of-equilibrium conditions, we can infer on the overall relaxation time of the low-to-high and high-to-low commutation, which is an important information to estimate maximum operation frequency of the thermal switch. In general, if at a given time all the modes propagate along, say, x under a certain lattice potential, and then something happens (change of potential, removal of temperature gradient), such a propagation will continue for a time that will depend on the phonon lifetimes. More precisely, we introduce an effective relaxation time as

$$\tau^{\perp,\parallel} = \frac{1}{\kappa^{\perp,\parallel}} \sum_{\lambda} \tau_\lambda \kappa_\lambda^{\perp,\parallel} \tag{6.2}$$

where the relaxation time of each mode λ is weighted with its contribution to the thermal conductivity. In this way we estimate an upper bound of the time needed for the conductance to change from low to high and viceversa when the polarization is rotated, giving more weight to the modes that carry more heat. In Fig. 6.5 we plot the relaxation times τ_λ as a function of the frequency and the weighting factors $\kappa^{\perp,\parallel}(\nu)/\kappa^{\perp,\parallel}$, where we grouped the mode-by-mode contributions to $\boldsymbol{\kappa}$ in frequency intervals of 1 THz. We have obtained $\tau^{\perp} = 7$ ps and $\tau^{\parallel} = 5.8$ ps. These values are quite smaller than typical switching times of the polarization and thus their effect of the switching dynamics is negligible. Therefore, taking the ultrafast polarization switching time of 220 ps in thin-film ferroelectrics reported by Li and coworkers [137] we can estimate a maximum operation frequency of 4.5 GHz.

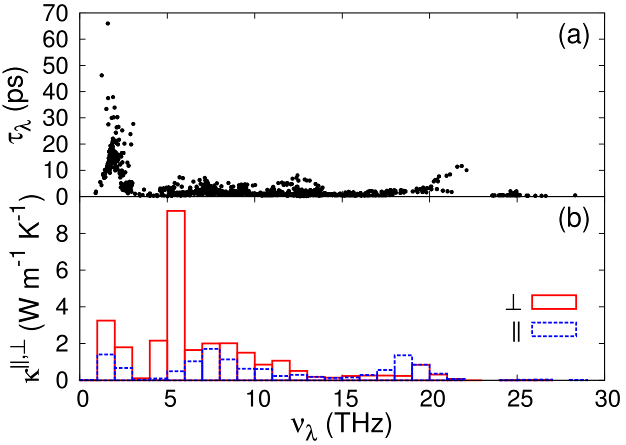

Figure 6.5: *(a) Relaxation time τ_λ as a function of frequency ν_λ. (b) Frequency resolved thermal conductivities $\kappa^{\perp}(\nu)$ and $\kappa^{\parallel}(\nu)$.*

6.3 Conclusions

In this Chapter we present a proposal of a thermal switch that takes advantage of the anisotropy of the thermal conductivity in PTO and, thus, of the availability of built-in low and high conductivity states. At variance with common anisotropic materials, the electrically-triggered rotation of the ferroelectric polarization can be used to switch between the two conductivity states. We also present a detailed study of the hysteresis cycle in the response of the thermal conductivity, showing that its value depends on how the electric field changed in the past. Finally, from the computed phonon relaxation times and contributions to the thermal conductivity, we argue that the response of such a ferroelectric thermal switch will be quite fast and only limited by speed of the ferroelectric switch itself; hence, our proposed device should be able to operate in the high-frequency regime.

Chapter 7

Strain engineering of ZnO thermal conductivity

As previously mentioned in this Thesis, strain engineering consists in modifying the properties of a material by applying strain, both compressive and tensile. In this Chapter we develop a study using ZnO that goes in this path, to find out how its thermal conductivity is affected by strain. An overview of the available experiments on the thermal conductivity of solids and liquids under pressure can be found in the paper by Ross et al. [138]. The data for covalent semiconducting and insulating materials are relatively scarce and are limited to some polymorphs of SiO_2 [139–141], Si [142], Ge [142], InSb [143], PbTe [144] and a few other compounds. The general trend outlined by these experiments seem to be that κ increases with pressure. However, the fact that the pressure range often differs from one experiment to the other, or that sometimes only data referring to uniaxial stresses are available, have prevented the formulation of a unifying picture on the strain effects on thermal conduction.

The advent of nanowires [145, 146], filamentary crystals with diameters in the range of few to several tens of nanometers, marked an increased interest in the design of materials with tailor made properties via strain engineering. Indeed, values of tensile strain much larger than those achievable in bulk materials have been obtained by a few groups [147–149]. ZnO can be synthesized under several different nanostructured forms and its great potential in several applications, ranging from nanogenerators [150], self-powered devices [151], and strain sensors [152] has been reported. Nevertheless, also in the case of ZnO the effect of strain on the vibrational and thermal properties has seldom been addressed.

The effect of strain on thermal conduction [27] is a key feature for thermoelectric applications, i.e., the conversion of heat into electricity via the the Seebeck effect [153]. The physics of thermoelectricity is summarized by the dimensionless figure of merit $ZT = (S^2\sigma/\kappa)T$, where S is the Seebeck coefficient, T is the temperature, while σ and κ are the electrical and thermal conductivity, respectively. High ZT values can be therefore obtained by reducing the thermal conductivity while preserving good charge transport characteristics or alternatively, by optimizing charge transport without simultaneously increasing the thermal conductivity. These ideas have been successfully applied to many different materials [154–157]. Our study clarifies if this can be achieved by applying strain to ZnO, a promising material for thermoelectric conversions [158] due to its low cost, stability at high temperature, and mainly because of its excellent charge carrier transport properties [159, 160].

7.1 Computational techniques and model

Motivated by the above considerations, we carry out equilibrium molecular dynamics (EMD) calculations within the Green-Kubo formalism (see Chapter 2) to assess the thermal conductivity of ZnO under strain. Specifically, we study the case of hydrostatic pressure, i.e. homogenous strain, as well as uniaxial strain.

The ZnO wurtzite phase has been described by the sum of a Coulomb and a Buckingham-type two-body potential, whose expression is

$$U(r_{ij}) = \frac{q_i q_j}{4\pi\epsilon_0 r_{ij}} + A \exp\left(-\frac{r_{ij}}{\rho}\right) - \frac{C}{r_{ij}^6}, \tag{7.1}$$

which is fully detailed in Chapter 3. Our simulations have been performed using the code LAMMPS [161]. We have used a simulation cell with dimensions of 3.859 × 3.899 × 4.123 nm^3 containing 5376 atoms to estimate the thermal conductivity along the a and c crystallographic directions (see Fig. 7.1). As previously shown for different

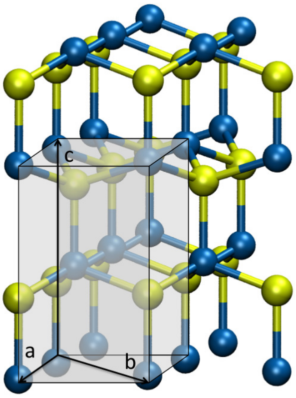

Figure 7.1: *Stick and ball representation of ZnO wurtzite crystal structure.*

systems including metal oxides [162–164], such cell dimensions guarantee the lack of any size artefacts that might affect thermal conductivity calculations within the Green-Kubo approach. The sample was preliminarly equilibrated for 500 ps in the isothermal-isobaric (NPT) ensemble, with a timestep of 1 fs, using the Nosé-Hoover thermostat and barostat at temperature and pressures of 300 K and 1 atm respectively. The autocorrelation function was then sampled for 2 ns in a microcanonical simulation. The maximum value chosen for the correlation time was 80 ps. The present choice of the simulation time as well as the maximum correlation time were motivated by the requirement to mitigate as much as possible the statistical error occurring in the estimation of the heat current autocorrelation function, while preserving a reasonable computational cost.

We also carry out lattice dynamics calculations solving the Boltzmann Transport Equation (BTE) within the Relaxation Time Approximation (RTA) (also explained in Chapter 2) to rationalize the results of the EMD calculations. We have chosen not to work with the iterative process in this case because, despite its classical nature, the potential we use features long-range interactions. This fact results in the need of considerably large supercells, because anharmonic force constants need to be computed among very far-away neighbours. However, we remark that our tests provide clear evidence that Normal-processes, i.e., normal scattering events, are not expected to be important in ZnO. Accordingly, we preferred to adopt the RTA solution which allows for using fully converged cell sizes and for properly treating far-away interactions. We use the ShengBTE code [37] for that. Phonon frequencies ν_λ were obtained by finite differences, using the Phonopy simulation package [127]. We use a ~ 5.5 Å cutoff for the generation of displacements in the 3^{rd} order force constants matrix.

In order to estimate the effect of uniaxial strains on the ZnO Seebeck coefficient, our colaborators at the Università di Cagliari (Italy) combine first-principles calculations with the Boltzmann transport theory within the constant scattering time approximation. The details of these calculations can be found in our publication [165].

7.2 Results of unstrained ZnO

The simulations that appear in this Section have been performed both with the Rigid Ion (RI) model and with the Core-Shell (CS), both explained in Chapter 3. The first thing we did was calculate the phonon bands of ZnO using Phonopy and the two models. In Fig. 7.2 we can see that acoustic branches are well reproduced by both models, but the optical ones are in a far better agreement with those obtained from first principles [166] in the CS model, that reproduce even the gap between the six lower and the six higher bands. Nevertheless as we are interested in thermal properties that are typically dominated by the acoustic modes, we expected to obtain similar results with the two models.

Fig. 7.3 shows the room temperature normalized heat current autocorrelation function (up) and the corresponding thermal conductivity (down) using the RI (left) and the CS (right) models as a function of the correlation time for a single trajectory collected for an unstrained bulk ZnO sample. For both models we observe an oscillatory behaviour of the heat current autocorrelation function (larger for the CS model) which has been recently also reported for complex silica structures [167, 168] and attributed to the relative motion of bonded atoms with different masses [163] or to the presence of optical phonons [169]. Due to the presence of such large oscillations in the autocorrelation function, the direct estimate of the thermal conductivity with the Green-Kubo integral is clearly not trivial since

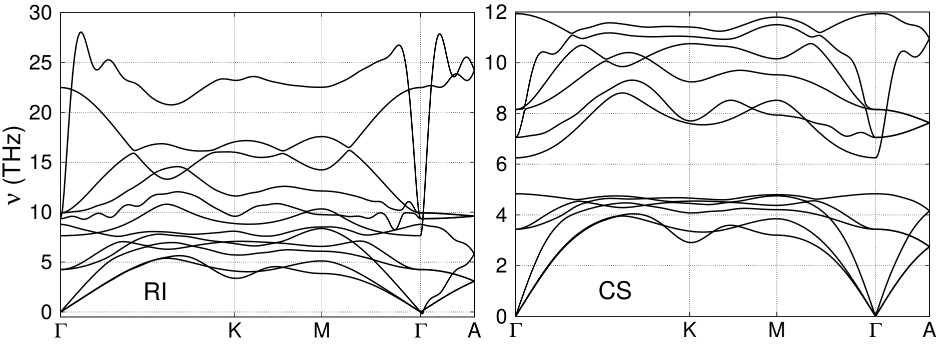

Figure 7.2: *Phonon bands of ZnO using the Buckingham potential with the Rigid Ion (left) and the Core-Shell (right) models.*

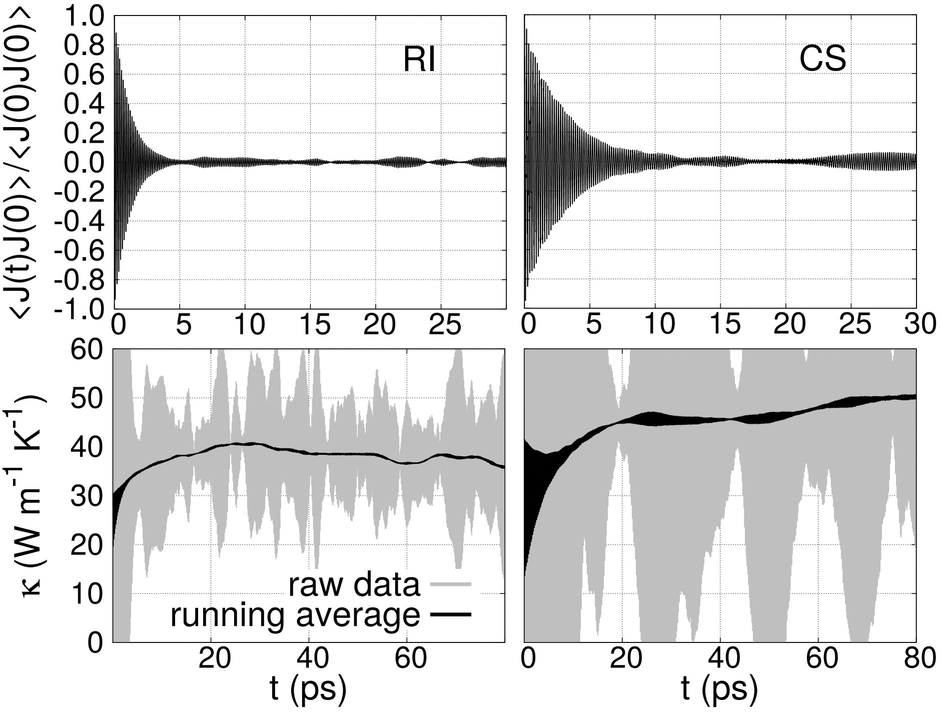

Figure 7.3: *Room temperature heat current autocorrelation function (up) and the corresponding thermal conductivity* κ_{cc} *(down) as a function of the correlation time obtained for one single trajectory. We show the results using the Rigid Ion (left) and the Core-Shell (right) models for the ZnO.*

the large amount of noise prevents the identification of a convergence region. A possible strategy recently proposed to directly address the thermal conductivity [167] in this case consists in performing a running average of the integral in overlapping blocks of few thousands steps. In the RI simulations, when the convergence region is eventually identified, a time lapse of at least 50000 time steps is set, over which the integral shows a constant value. However, the thermal conductivity does not seem to properly converge when modeling ZnO with the CS model.

In this kind of simulations, a configurational average over some independent trajectories has to be performed in order to obtain an acceptable result for the thermal conductivity. In our case, we have performed for each model the average over five independent trajectories differentiated by random initial velocities.

As can be appreciated in Fig. 7.4, it takes more time for the thermal conductivity to converge in the CS model simulations. In fact, the growing trend that show some of the independent simulations in this case makes us suspect that the thermal conductivity is not really converged even at 80 ps. This fact added to the larger noisy behaviour of the CS model, to its higher computational cost, to the unnecesary complexity of the model to describe the ZnO, and to the results obtained for both models, made us decide tu use the RI model in the following sections of the chapter.

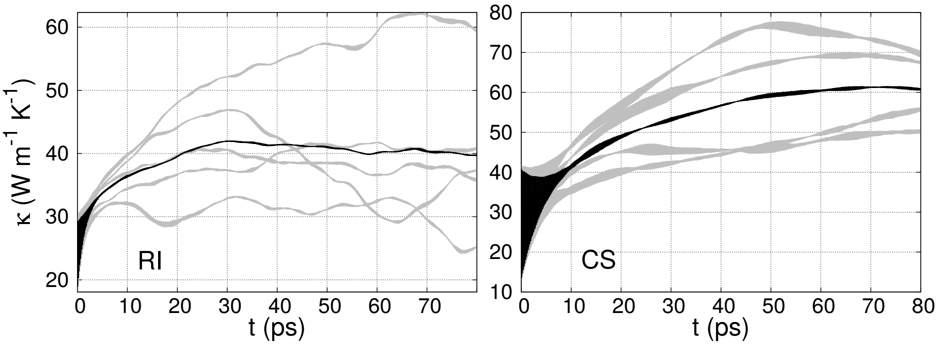

Figure 7.4: *Room temperature thermal conductivity* κ_{cc} *as a function of the correlation time for five independent simulations (gray curves) together with the corresponding average (black curve), using the RI (left) and CS (right) model.*

The estimated value of the thermal conductivity using the RI model calculated along the c direction is $\kappa_{cc} = 42 \pm 7$ W m^{-1} K $^{-1}$ while in the case of the a direction we obtain $\kappa_{aa} = 38{\pm}6$ W m^{-1} K^{-1}. The error in the average thermal conductivity has been estimated as the corresponding standard deviation. These two values are in remarkably good agreement with the experimental values, which range between 37 and 47 W m^{-1} K^{-1} [170]. We attribute this satisfactory result to the good description of the acoustic phonon branches provided by the Buckingham-type force field.

7.3 Thermal conductivity of ZnO under hydrostatic strain

We investigated the effect of strain on ZnO thermal conductivity by considering first the case of hydrostatic strain ϵ defined with respect to the equilibrium volume V_0 as:

$$\epsilon = \frac{V}{V_0} \tag{7.2}$$

where V is the volume of the strained simulation cell. We applied strains in the interval ±4% by considering steps of 2%. In detail, starting from the unstrained zero pressure cell volume V_0, strain is applied to the atomistic simulation cell by rescaling the size of the periodic box to $V = \epsilon V_0$. Furthermore, the positions of all atoms in the box were also rescaled accordingly. The system was then equilibrated at $T = 300$ K by performing an isothermal simulation as long as 0.5 ns in order to fully relax the atomic positions. The thermal conductivity was then estimated over five different trajectories using the same procedure as described above.

It has been demonstrated [171] that the effect of hydrostatic strain on the thermal conductivity of a crystalline system can be cast in the following power law:

$$\kappa \sim \epsilon^{-\gamma} \tag{7.3}$$

where γ is a material dependent parameter. Such a power-law has been interpreted as mainly due to the effect of both phonon relaxation time τ and group velocities v_g which show, in turn, the same power-law dependence on the applied hydrostatic strain:

$$\tau \sim \epsilon^{-(2\alpha+2\beta)} \tag{7.4}$$

and

$$v_g \sim \epsilon^{-\alpha} \tag{7.5}$$

where γ=4α+2β and both α and β are material dependent parameters.

Fig. 7.5 shows the thermal conductivities κ_{cc} (blue) and κ_{aa} (red) as a function of strain that we obtained from the Green-Kubo simulations. We observe a very good agreement between the model of Eq. (7.3) and our data that can be closely fitted as $\kappa_{cc} = 41.65 \times \epsilon^{-5.00}$ (blue curve in Fig. 7.5) and $\kappa_{aa} = 40.70 \times \epsilon^{-6.26}$ (red curve in Fig. 7.5).

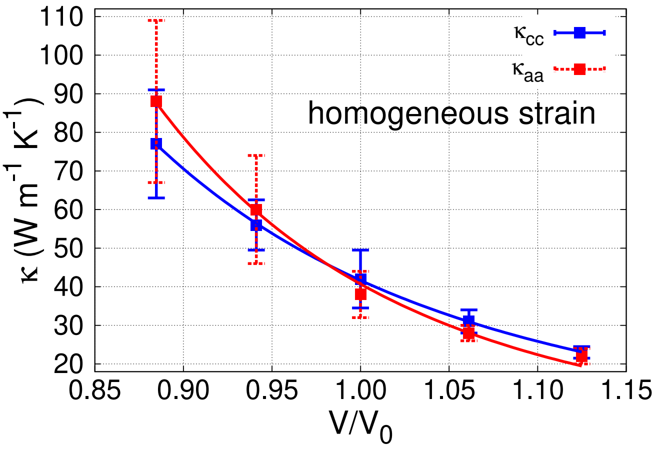

Figure 7.5: *Room temperature thermal conductivities* κ_{cc} *(blue) and* κ_{aa} *(red) as a function of the applied homogeneous strain. The blue and red curves represent the fitting function of Eq.* (7.3) *for* κ_{cc} *and* κ_{aa} *respectively.*

The present results stands for the reliability of our simulation protocol to describe the thermal conductivity dependence of crystalline systems under hydrostatic strain. We observe that by applying hydrostatic strains up to +4% (-4%) we are able to decrease (increase) the ZnO thermal conductivity by almost a factor 2 and, therefore, to largely affect its figure of merit. We observe that recent DFT results [172] give a less pronounced dependence of the thermal conductivity with the hydrostatic strain, fact most likely due to the limitations of the interatomic potential here employed. Nevertheless, the trend is similar to what found in the present work.

We take profit of the mode analysis offered by the RTA-BTE method to investigate how strain differently affect phonon group velocities and relaxation times. We focus on the two extreme cases of +4% and -4% strain where any possible effect is expected to be the largest, and we restrict these calculations to the c direction. We preliminary remark that RTA-BTE calculations underestimate κ both for the unstrained case (for which we get $\kappa_{cc} = 30.7$ W m^{-1} K^{-1}) and for the +4% ($\kappa_{cc} = 9.5$ W m^{-1} K^{-1}) and -4% ($\kappa_{cc} = 60.3$ W m^{-1} K^{-1}) cases. However, the overall thermal conductivity variations with respect to the unstrained case are very similar. Here we rather address relative variations than absolute values.

Fig. 7.6 shows the spectral contribution to thermal conductivity in the case of the unstrained system. We observe that the main contribution to thermal conductivity is due to phonons at relatively low frequency below 15 THz. A similar behaviour has been previously predicted for ZnO in Ref. [166] where it was demonstrated that the thermal conductivity was mainly governed by the six lower phonon branches. This result allows neglecting the contribution of higher frequency modes.

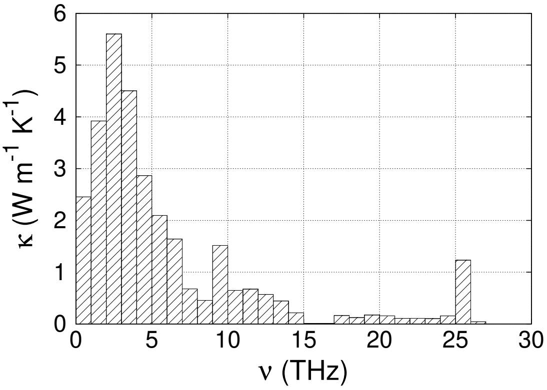

Figure 7.6: *Spectral contribution to thermal conductivity in the case of the unstrained system at T=300 K.*

To better understand the effect of the strain we use again the technique introduced in Chapter 5. In detail, we group all the terms that are explicitly dependent on the phonon frequencies of the thermal conductivity by introducing the quantity $\theta_\lambda = f_\lambda(f_\lambda + 1)\nu_\lambda^2$, i.e. the frequency-dependent contribution of the specific heat. This allows us to derive the strain-induced variation of κ as

$$\begin{aligned}\Delta\kappa = \kappa - \kappa^0 &= \sum_\lambda \Delta\kappa_\lambda \\ &= \frac{h^2}{N\Omega T^2}\sum_\lambda \Bigg[\Delta\left(\frac{1}{V}\right)\theta_\lambda^0(v_\lambda^0)^2\tau_\lambda^0 + \frac{1}{V_0}\Delta\theta_\lambda(v_\lambda^0)^2\tau_\lambda^0 \\ &\quad + \frac{1}{V^0}\theta_\lambda^0\Delta v_\lambda^2\tau_\lambda^0 + \frac{1}{V_0}\theta_\lambda^0(v_\lambda^0)^2\Delta\tau_\lambda + \mathcal{R}_\lambda\Bigg], \qquad (7.6)\end{aligned}$$

where we have applied the mathematical reasoning appearing in Appendix D. Like in Chapter 5, where the superscript "0" indicated zero-field quantities, here it indicates zero-strain quantities, while the magnitudes without superscript are for the strained cases. We also define $\Delta g = g - g^0$ for any magnitude g. This technique allows us to detect the change of which magnitude is more relevant for the global change of the thermal conductivity when we apply strain to the system. Also in this case we only take into account the c component of all the vector quantities in Eq. (7.6). This expression allows us to readily identify changes in κ that are dominated by the change of just one of the four factors (V, θ_λ, v_λ, τ_λ) involved in the mode conductivity, while $\mathcal{R}_\lambda$ captures any lingering changes, i.e., changes in κ where the change of two or more factors are implicated.

Fig. 7.7 shows the variations with respect to the unstrained condition of the different contributions to thermal conductivity (see Eq. 7.6) in the case of -4% (top) and (+4%) strains. The largest variation observed in both cases is found for the phonon relaxation times τ_λ (blue dashes), which is predominant with respect to all the other contributions including the group velocities v_λ. Notice that the term $\mathcal{R}_\lambda$ adds to the global trend for negative strains, while for positive strains it has an opposite behaviour. This explains why when compressing the material the thermal conductivity increases more than what the thermal conductivity is reduced when expanding it.

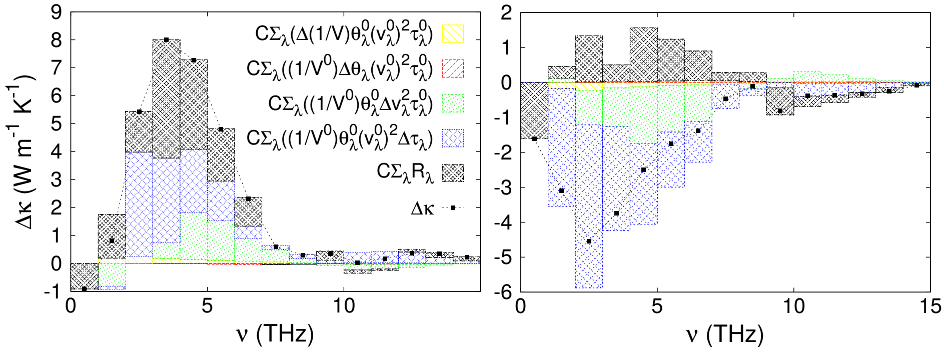

Figure 7.7: *Differences with respect to the unstrained condition of the different contributions to thermal conductivity (see* Eq. (7.6)*) in the case of* -4% *(left) and* +4% *(right) hydrostatic strains. The points represent the whole thermal conductivity difference while the colored stripes represents the different contributions.*

7.4 Thermal conductivity of ZnO under uniaxial strain

We further analyze the effect of strain on the ZnO thermal conductivity by taking into account the uniaxial tensile strain $\eta = (L - L_0)/L_0$, where L is the simulation cell length upon the application of the strain and L_0 is the one corresponding to 0% strain. In detail, the tensile strain was applied along the c direction (see Fig. 7.1) in the interval ± 4% by considering steps of 2%. We focus on the c axis since this is the most common growth orientation of ZnO nanowires and, therefore, it is the crystallographic axis along which high strain can be more easily applied. In this case, upon the elongation of the simulation cell, we perform an NPT (500 ps) simulation by fixing the simulation cell length along the c direction and allowing a full relaxation in the other two directions. The results are shown in Fig. 7.8. Differently from the previous case, we observe comparatively smaller variations upon the application of the uniaxial strain. In particular, the estimated κ_{aa} values for the 0% and the -4% strain are almost identical, indicating a negligible dependence of the thermal conductivity on compressive strains.

In order to further validate this result, we estimated the ther-

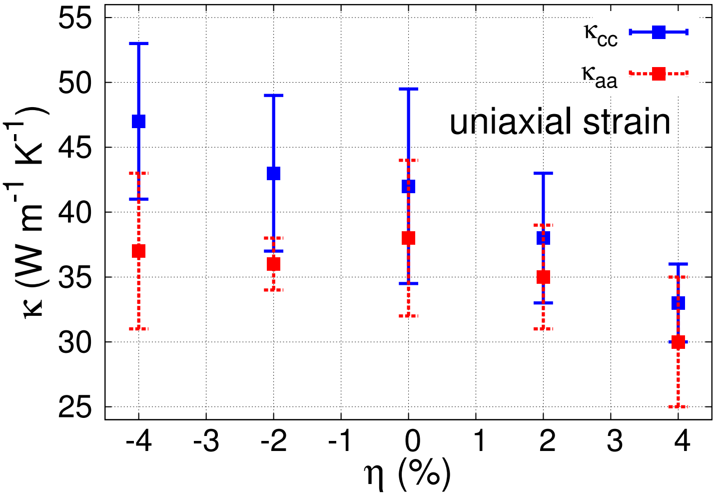

Figure 7.8: *Room temperature thermal conductivities* κ_{cc} *(blue) and* κ_{aa} *(red) as a function of the applied uniaxial strain.*

mal conductivity solving the RTA-BTE for the case of +4% and -4% uniaxial strains. Also in this case, we observe that the thermal conductivities corresponding to the 0% and -4% strain are very similar (30.7 and 30.0 W m^{-1} K^{-1} respectively), while the κ value corresponding to the 4% strain show a larger variation being equal to 18.2 W m^{-1} K^{-1}. This agreement between EMD and BTE is particularly remarkable and vouch for the reliability of the results obtained. On the one hand, the BTE results indicate that the EMD runs do not suffer from possible shortcomings of this kind of simulations, such as not long enough simulation and correlation times or too small computational cells; on the other hand, the EMD results, which account for anharmonicity at all orders, validate the results obtained from the solution of the BTE where these effects are considered only up to the third order.

We argue that the present result is relevant for thermoelectric applications since it has been reported [173] that the ZnO thin film electrical resistivity can be reduced by more than a factor 4 by imposing a uniaxial (compressive) strain as small as -0.4%. Fig. 7.9 presents the results of the first-principles calculations of the Seebeck coefficient as a function of temperature performed by our colabora-

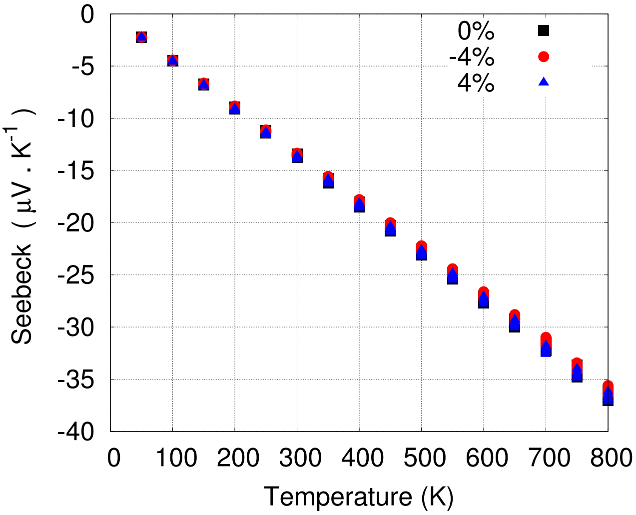

Figure 7.9: *Temperature dependence of the Seebeck coefficient in the case of 0% (black squares), −4% (red circles) and +4% (blue diamonds) uniaxial strain.*

tors in Cagliari. These calculations have been performed at a fixed electron carrier concentration of 6×10^{20} cm^{-3} corresponding to the maximum electron concentration achievable in ZnO via doping [158]. It clearly shows that the Seebeck coefficient is nearly unaffected by strain over a wide range of temperatures. This allows us to combine three separate results, namely:

- Our calculation indicates that the thermal conductivity is only marginally affected by compressive tensile strain up to 4%.
- Experimental evidence shows instead that electrical conductivity can be dramatically increased by imposing uniaxial compressive strains.
- Present first-principles calculations show that the Seebeck coefficient is nearly unaffected by tensile strain.

This implies the power factor ($S^2\sigma$) as a whole should increase upon uniaxial strain, leading to a corresponding ZT increase.

Similarly to the previous case, we show in Fig. 7.10 the variations with respect to the unstrained condition of the different contributions

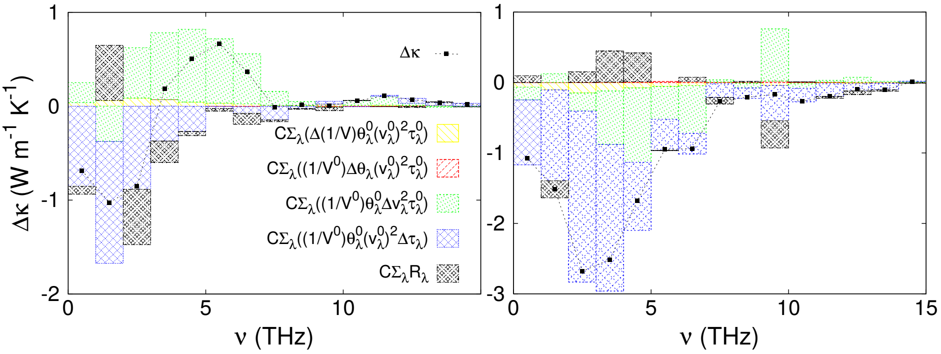

Figure 7.10: *Differences with respect to the unstrained condition of the different contributions to thermal conductivity (see Eq. 7.6) in the case of -4% (left) and +4% (right) uniaxial strains. The points represent the whole thermal conductivity difference while the colored stripes represents the different contributions.*

to thermal conductivity in the case of -4% (top) and (+4%) uniaxial strains. We observe large differences with respect to the case of hydrostatic strain. In the case of the -4% strain the detrimental contribution due to the phonon relaxation times at frequencies below $\sim$ 3 THz is balanced by the increase of the group velocities (green dashes) at higher frequencies, leading to an overall thermal conductivity equal to the one at 0% strain. On the other side, in the case of 4% strain, the contribution of both phonon relaxation times and group velocities is detrimental, leading to a thermal conductivity reduction with respect to the 0% strain case. A similar competitive mechanism has been recently identified for different telluride systems [174]. Differently from the case of hydrostatic strain, the contribution of the term $\mathcal{R}_\lambda$ (black dashes) is negligible. In order to verify wether the effect of the group velocities is compensated by the effect of the phonon density of states (PDOS), we compare in Fig. 7.11 the PDOS in the case of uniaxial compressive and tensile strains with the 0% strain case. In both cases we did not observe any significant PDOS variation, both in the acoustic as well as optical region, with respect to the unstrained sample. For this reason, we cannot claim any compensation effect on the group velocities by corresponding PDOS variation upon the application of tensile strains.

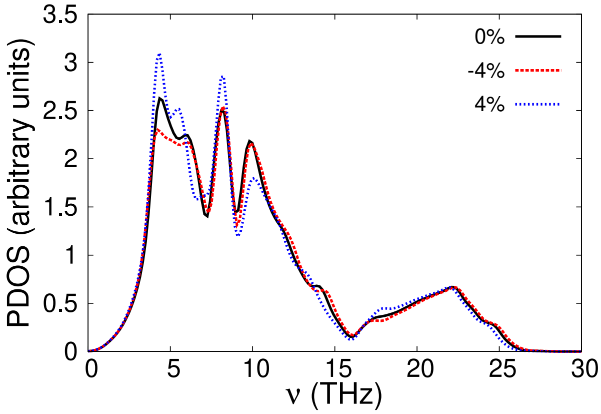

Figure 7.11: *Phonon density of states of ZnO for the unstrained case (black) and for the compressive (red) and tensile (blue) uniaxial strains of 4%.*

7.5 Conclusions

We have investigated the effect of strain (hydrostatic and uniaxial) on bulk ZnO thermal conductivity using EMD simulations within the Green-Kubo formalism and the numerical solution of the BTE equation within the RTA approximation. In the case of hydrostatic strain up to ±4% we estimate a corresponding thermal conductivity variation of more than a factor 2. On the other side, for uniaxial strains, the estimated thermal conductivity variations are comparatively very limited. In particular, for uniaxial compressive strain up to -4%, we estimate a negligible thermal conductivity variation. This result is potentially important for thermoelectric applications since the ZnO electrical resistivity is dramatically affected by a uniaxial compressive strain. This would arguably lead to a ZT increase due to the fact that the thermal conductivity would be unaffected. The spectral analysis of the solution of the BTE shows that, for hydrostatic strains, the thermal conductivity variations mainly originate from the variation of the phonon relaxations times. For uniaxial compressive strains instead the contribution of the phonon relaxations time is balanced by the increase of the group velocities.

Chapter 8

Conclusions

If we have to highlight a contribution of this Thesis to the field of condensed matter physics, we would say that it has been the opening of a line of research that has hardly been addressed in the literature, modulating the thermal conductivity of materials by modifying their crystal lattice. This was our original idea to overcome the difficulty of modifying the behavior of phonons, since they are particles that have neither mass nor charge and can not be directly affected by the typical force fields. Our studies have not only shown that this coupling between the thermal conductivity of a crystalline solid and an external field that distorts the crystal lattice is a perfectly observable effect, but that these effects have been quantified in different materials, reaching values of considerable magnitude. The studied materials have been chosen because they are representative compounds of many other oxides, besides being very relevant materials in today's technological applications. However, this effect analyzed throughout the chapters of the Thesis is a generic effect, i.e., it is not restricted just simply to the family of oxides, and in principle it should be possible to be observed in any material. In fact, a line of research that remains open with this Thesis is to find another materials in which this effect may be higher or have greater relevance in applications. In this line we have carried out a similar study using $SrTiO_3$ [175], a material in which we expected a greater coupling between the thermal conductivity and the electric field, due to its higher electric susceptibility. As in the case of $PbTiO_3$, the reduction of the symmetry of the lattice because of the external field activates another scattering mechanisms that decrease the thermal conductivity. However, we obtained that due to the global band softening caused by the electric field in $PbTiO_3$, the reduction of the thermal conductivity is higher in this material.

Solving the Boltzmann Transport Equation has allowed us, in addition to obtaining the values of the thermal conductivity at many different temperatures, going into detail in the microscopic description, providing information of the phonon properties. Working with this information we have been able to develop the method presented in Appendix D, another important contribution of our research. This method allow us to appropriately compare two different situations, one in which the crystal lattice is altered and the one in which it is not, and check the change of which properties of phonons affect more to the thermal conductivity. In both $PbTiO_3$ and ZnO, we have found that changes in frequencies, and hence, in specific heat, are almost negligible, and that changes in velocities never play the main role, leaving it to the mean free paths or the relaxation times of phonons. Remember that these last two magnitudes are related by the expression $\vec{F}_\lambda = \tau_\lambda(\vec{v}_\lambda + \vec{\Delta}_\lambda)$, we just simply work with the relaxation times when using the Relaxation Time Approximation because the velocities are not modified and it is easier to use the product $v_\lambda^2\tau_\lambda$, and we work with the mean free paths when using the iterative process for solving the BTE because is the magnitude affected by the iterations, so we use the product $\vec{v}_\lambda \cdot \vec{F}_\lambda$.

In a more applicative sense, the studies presented in this Thesis describe also the background of two possible designs for a thermal switch. One would be based in the inherent anisotropy of PTO, and its operation would consist of changing the direction of polarization of the system, making phonons to propagate in a different crystallographic direction. The second one would be based in that the domains can be experimentally written and erased also by means of an external electric field. We have also presented the possibility of designing a thermal transistor, due to the possibility of continuous sweeping in thermal conductivities by applying an electric field maintained in time that distorts the structure of the material.

This Thesis leaves many open topics, which will be future research lines of the group. For example, it would be interesting to find out under what conditions thermal transport occurs in PTO at temperatures close to the transition temperature from paraelectric to ferroelectric. This could lay the foundation for designing a device able to operate combining both phases, that in addition would have the advantage to work exclusively by means of thermal mechanisms, since the phase transitions would be controlled by the application of heat instead of applying an electric field or strain. This is currently being investigated by means of non-equilibrium molecular dynamics, although it would be better to study it by equilibrium molecular dynamics, since by this method a temperature gradient does not arise in the system and the transition temperature can be targeted more accurately. Our limitation to do so is that the SCALE-UP program does not yet have a parallel implementation of the distribution of energy between the different atoms of the system, which is necessary to properly calculate the microscopic thermal flux that appears in the Green-Kubo equation. Another interesting aspect that worth to be studied is if a domain wall can be moved along the system by a large enough heat flow. If phonons that interact with the domain wall are capable of transfer enough momentum to the atoms that do not contribute to the polarization of any of the domains, these atoms could displace, thus becoming part of one of the domains of the system, forcing the atoms placed in the next parallel plane to the domain wall to be relocated, forming a new domain wall displaced with respect to the first one. This problem perfectly suits in the non-equilibrium molecular dynamics framework.

In summary, we can conclude that the field of research that we have started, thermal transport in oxides, still has many open lines and interesting problems to be solved.

Appendix A

Microscopic thermal flux

It is not easy to find in the literature the derivation of an expression for the atomistic heat current (or microscopic thermal flux). The only place we have been able to check it is in the Supplemental Material of reference [176]. Here we follow their procedure but in more detail.

In an isolated system where there are neither sinks or sources of energy, the continuity equation of the energy relates the time-derivative of energy density $\rho(\vec{r},t)$ with the divergence of the heat flux density $\vec{J}(\vec{r},t)$

$$\frac{d\rho(\vec{r},t)}{dt} + \vec{\nabla} \cdot \vec{J}(\vec{r},t) = 0. \tag{A.1}$$

The most general expression for the energy density of an atomistic system would be

$$\rho(\vec{r},t) = \sum_{i=1}^{N} \epsilon_i(t)\delta(\vec{r} - \vec{r}_i(t)), \tag{A.2}$$

where $\epsilon_i(t)$ is the energy of atom i, located at $\vec{r}_i(t)$. $\delta(\vec{r} - \vec{r}_i(t))$ is the Dirac delta function in three dimensions

$$\delta(\vec{r} - \vec{r}_i) = \delta(x - x_i)\delta(y - y_i)\delta(z - z_i). \tag{A.3}$$

We can define an atomic heat flux density vector in a similar way

$$\vec{J}(\vec{r},t) = \sum_{i=1}^{N} \vec{j}_i(t)\delta(\vec{r} - \vec{r}_i(t)), \tag{A.4}$$

where $\vec{j}_i(t)$ is the heat current of atom i.

Taking the time derivative of $\rho(\vec{r}, t)$ we get

$$\frac{d\rho}{dt} = \sum_{i=1}^{N} \left\{ \frac{d\epsilon_i}{dt} \delta(\vec{r} - \vec{r}_i) - \epsilon_i \vec{v}_i \cdot \vec{\nabla} \delta(\vec{r} - \vec{r}_i) \right\} \tag{A.5}$$

where $\vec{v}$ is the velocity of the i^{th} atom. The divergence of $\vec{J}(\vec{r}, t)$ gives

$$\vec{\nabla} \cdot \vec{J} = \sum_{i=1}^{N} \vec{j}_i \cdot \vec{\nabla} \delta(\vec{r} - \vec{r}_i). \tag{A.6}$$

We insert equations (A.5) and (A.6) in equation (A.1)

$$\sum_{i=1}^{N} \left\{ \frac{d\epsilon_i}{dt} \delta(\vec{r} - \vec{r}_i) - \epsilon_i \vec{v}_i \cdot \vec{\nabla} \delta(\vec{r} - \vec{r}_i) \right\} = - \sum_{i=1}^{N} \vec{j}_i \cdot \vec{\nabla} \delta(\vec{r} - \vec{r}_i). \tag{A.7}$$

Multiplying by x and integrating over all space using the fact that

$$\int_{-\infty}^{\infty} dx \frac{d\delta(x)}{dx} f(x) = - \int_{-\infty}^{\infty} dx \delta(x) \frac{df(x)}{dx}, \tag{A.8}$$

the right part of the equation becomes

$$\begin{aligned}
& - \int_{-\infty}^{\infty} d\vec{r} \sum_{i=1}^{N} x \vec{j}_i \cdot \vec{\nabla} \delta(\vec{r} - \vec{r}_i) \\
&= \int_{-\infty}^{\infty} d\vec{r} \sum_{i=1}^{N} \vec{\nabla} \cdot (x \vec{j}_i) \delta(\vec{r} - \vec{r}_i) \\
&= \int_{-\infty}^{\infty} d\vec{r} \sum_{i=1}^{N} \left[(\vec{\nabla} x) \cdot \vec{j}_i + x (\vec{\nabla} \vec{j}_i) \right] \delta(\vec{r} - \vec{r}_i) \\
&= \int_{-\infty}^{\infty} d\vec{r} \sum_{i=1}^{N} \left[\frac{dx}{dx} \vec{u}_x \cdot \vec{j}_i + x \cdot 0 \right] \delta(\vec{r} - \vec{r}_i) \\
&= \sum_{i=1}^{N} \int_{-\infty}^{\infty} dx j_{ix} \delta(x - x_i) \int_{-\infty}^{\infty} dy \delta(y - y_i) \int_{-\infty}^{\infty} dz \delta(z - z_i) \\
&= \sum_{i=1}^{N} j_{ix},
\end{aligned} \tag{A.9}$$

and the left part

$$\int_{-\infty}^{\infty} d\vec{r} \sum_{i=1}^{N} \left\{ \frac{d\epsilon_i}{dt} x\delta(\vec{r}-\vec{r}_i) - \epsilon_i x \vec{v}_i \cdot \vec{\nabla}\delta(\vec{r}-\vec{r}_i) \right\}, \tag{A.10}$$

where the first term is

$$\sum_{i=1}^{N} \frac{d\epsilon_i}{dt} \int_{-\infty}^{\infty} d\vec{r} x\delta(\vec{r}-\vec{r}_i) = \sum_{i=1}^{N} \frac{d\epsilon_i}{dt} x_i, \tag{A.11}$$

and the second term is

$$\begin{aligned} -\sum_{i=1}^{N} \epsilon_i \int_{-\infty}^{\infty} d\vec{r} x \vec{v}_i \cdot \vec{\nabla}\delta(\vec{r}-\vec{r}_i) \\ = \sum_{i=1}^{N} \epsilon_i \int_{-\infty}^{\infty} d\vec{r}\, \vec{\nabla} \cdot (x\vec{v}_i)\delta(\vec{r}-\vec{r}_i) \\ = \sum_{i=1}^{N} \epsilon_i \int_{-\infty}^{\infty} d\vec{r} \left[(\vec{\nabla}x) \cdot \vec{v}_i + x\vec{\nabla} \cdot \vec{v}_i \right] \delta(\vec{r}-\vec{r}_i) \\ = \sum_{i=1}^{N} \epsilon_i \int_{-\infty}^{\infty} d\vec{r} \left[\vec{u}_x \cdot \vec{v}_i + 0 \right] \delta(\vec{r}-\vec{r}_i) \\ = \sum_{i=1}^{N} \epsilon_i v_{ix}. \end{aligned} \tag{A.12}$$

Replacing these calculations in Eq. (A.7) we get that the heat current of the total system in the x direction is

$$J_x = \sum_{i=1}^{N} j_{ix} = \sum_{i=1}^{N} \frac{d\epsilon_i}{dt} x_i + \epsilon_i v_{ix}, \tag{A.13}$$

what can be generalized to obtain the heat current vector of the total system

$$\vec{J} = \sum_{i=1}^{N} \vec{j}_i = \sum_{i=1}^{N} \frac{d\epsilon_i}{dt} \vec{r}_i + \epsilon_i \vec{v}_i. \tag{A.14}$$

The first term of this equation is related to the diffusive flow of heat while the second term is convective. We can rejoin the derivative and write it as

$$\vec{J} = \sum_{i=1}^{N} \vec{j}_i = \frac{d}{dt} \sum_{i=1}^{N} \vec{r}_i \epsilon_i, \tag{A.15}$$

what makes easy to realize about the relation between the heat current and the energy momentum defined in Eq. (2.39), that is

$$\vec{J} = \frac{d\vec{R}}{dt}. \tag{A.16}$$

Before finishing the explanation about the atomistic heat current it is necessary to mention that ϵ_i is the total energy of the i^{th} atom, so it can be split in its different components, typically the kinetic and the potential part, i.e., $\epsilon_i = \epsilon_i^K + \epsilon_i^P$. The kinetic energy of an atom is well defined, but the potential energy is not. Previously to perform a simulation using the definition of the microscopic heat current it is required to choose how to distribute the potential energy of the system between the atoms, and there is not an objective way to do that. Some works have proved that the choice almost does not affect the results [55], but when you are working with a pair potential, the most intuitive choice is to assign equitably to the atoms that are interacting in one term of the potential the fraction of the total energy that this term creates. Furthermore, if we work with a pair potential interaction, the derivative in Eq. (A.14) can be solved analytically, leading to the next expressions

$$\frac{d\epsilon_i}{dt} = \frac{d(\epsilon_i^K + \epsilon_i^P)}{dt}, \tag{A.17}$$

where

$$\frac{d\epsilon_i^K}{dt} = \frac{d}{dt}\left(\frac{1}{2} m_i v_i^2\right) = \frac{1}{2} m_i \frac{d(\vec{v}_i \cdot \vec{v}_i)}{dt} = \frac{1}{2} m_i 2\vec{a}_i \cdot \vec{v}_i = \vec{F}_i \cdot \vec{v}_i \tag{A.18}$$

and

$$\frac{d\epsilon_i^P}{dt} = \sum_{j=1}^{3N} \frac{d\epsilon_i^P}{dr_j} \frac{dr_j}{dt} = \sum_{j=1}^{3N} -f_{ji} v_j, \tag{A.19}$$

that are the ones used in this Thesis.

Appendix B

Thermal Boundary Resistance from Non-Equilibrium Thermodynamics

This Appendix combines the procedures that appear in references [177] and [178] to obtain a mathematical expression for the thermal boundary resistance (TBR). This resistance is a local property of the material, which appears because of the distortions in the positions of the ions, which affect the phonons. The derivation presented here is valid for any interface, either between two materials, or as in this Thesis, between two ferroelectric domains of the same material.

To study a system with the formalism of the non-equilibrium thermodynamics, we have to identify its independent variables A_i [177]. For these variables, we define its conjugate fluxes and forces as

$$J_i = \frac{dA_i}{dt} \qquad\qquad X_i = \frac{\partial S}{\partial A_i}, \tag{B.1}$$

where t is the time and S is the entropy of the system. We assume local equilibrium for the system, so the second law of thermodynamics is reformulated in terms of the local entropy production in the system σ, which is function of the conjugate fluxes and forces

$$\sigma = \sum_i J_i X_i > 0. \tag{B.2}$$

Each flux J_i can be expressed as a linear combination of all the generalized forces X_i, and vice versa, the generalized forces are linear functions of the fluxes, related by the Onsager resistivity coefficients r_{ij}. As in this Thesis we work just with the lattice contribution to the heat transport (in absence of any mass transport), our linear combination is reduced just to the thermal flux J_q and its generalized force X_q

$$X_q = \sum_i r_{qi} J_i = r_{qq} J_q. \tag{B.3}$$

As our heat transport occurs just in one dimension we also avoid to work with vectors in this appendix.

We can write an entropy continuity equation, where the change of the entropy in a volume element is given by the flow of entropy in and out of that volume element and by the entropy production inside the volume element

$$\frac{\partial s}{\partial t} = -\frac{\partial J_s}{\partial z} + \sigma. \tag{B.4}$$

In this equation s is the entropy density and J_s the entropy flux.

According to the first law of thermodynamics, we can also write this energy balance equation

$$\frac{\partial u}{\partial t} = -\frac{\partial J_q}{\partial z}, \tag{B.5}$$

that relates the change in internal energy density u per unit of time with the thermal flux.

These two time derivatives of the equations (B.4) and (B.5) are related by the thermodynamic identity $dU = TdS$, by

$$\frac{\partial s}{\partial t} = \frac{1}{T}\frac{\partial u}{\partial t}, \tag{B.6}$$

so replacing (B.5) in (B.6) and doing the following calculations

$$\frac{\partial s}{\partial t} = \frac{1}{T}\frac{\partial u}{\partial t} = -\frac{1}{T}\frac{\partial J_q}{\partial z} = -\frac{\partial}{\partial z}\left(\frac{J_q}{T}\right) + J_q \frac{\partial}{\partial z}\left(\frac{1}{T}\right) \tag{B.7}$$

we obtain an expression comparable with (B.4). From this comparation we can identify

$$J_s = J_q/T \tag{B.8}$$

that relates the entropic and the thermal fluxes, and

$$\sigma = J_q \frac{\partial}{\partial z}\left(\frac{1}{T}\right), \tag{B.9}$$

that gives an expression for the entropy production. Just checking the equation (B.2) after obtaining (B.9), we realise that

$$X_q = \frac{\partial}{\partial z}\left(\frac{1}{T}\right), \tag{B.10}$$

and developing this expression we get

$$X_q = \frac{\partial}{\partial z}\left(\frac{1}{T}\right) = \frac{\partial}{\partial T}\left(\frac{1}{T}\right)\frac{\partial T}{\partial z} = -\frac{1}{T^2}\frac{\partial T}{\partial z}. \tag{B.11}$$

Using now (B.3) we get

$$-\frac{1}{T^2}\frac{\partial T}{\partial z} = r_{qq} J_q. \tag{B.12}$$

The Fourier's law can be written as

$$\frac{\partial T}{\partial z} = -R_{qq} J_q, \tag{B.13}$$

so equating the two temperature derivatives of the two last expressions we find

$$R_{qq} = T^2 r_{qq}. \tag{B.14}$$

If we are working with interfaces, equation (B.4) is rewritten in the form

$$\frac{\partial s^{\text{int}}}{\partial t} = -(J_{s,l} - J_{s,r}) + \sigma^{\text{int}} \tag{B.15}$$

where the superscript "int" indicates an interface quantity, while $J_{s,l}$ and $J_{s,r}$ are the entropy density fluxes through the left and right borders of the interface, respectively [178]. Performing again the same calculations and taking into account that our system is in a stationary state we obtain the entropy density production term for the interface σ^{int}

$$\sigma^{\text{int}} = J_q\left(\frac{1}{T_s} - \frac{1}{T_l}\right) + J_q\left(\frac{1}{T_r} - \frac{1}{T_s}\right). \tag{B.16}$$

where T_s is the average temperature of the region of the material that we have defined as the interfase. As we can see from this equation, the study of the interfase requires the generalized forces of the left and right sides

$$X_{q,l} = \frac{1}{T_s} - \frac{1}{T_l} = r_{qq,l} J_q \tag{B.17}$$

$$X_{q,r} = \frac{1}{T_r} - \frac{1}{T_s} = r_{qq,r} J_q, \tag{B.18}$$

and obviously two Onsager resistivity coefficients. Therefore, the total thermal boundary resistance R^{TBR} is in fact a series of two Onsager resistances

$$R_{qq}^{\mathrm{TBR}} = T_s^2 \left(r_{qq,l} + r_{qq,r} \right) = \frac{T_s^2}{J_q} \left(\frac{1}{T_r} - \frac{1}{T_l} \right). \tag{B.19}$$

We can write this equation in a different way

$$R_{qq}^{\mathrm{TBR}} = \frac{\Delta T}{J_q} \frac{T_s^2}{T_l T_r} \tag{B.20}$$

that allows us to see that the diference between our definition of the TBR and the fenomenological TBR of Kapitza

$$R_{\mathrm{Kapitza}} = \frac{\Delta T}{J_q}, \tag{B.21}$$

is just the factor $T_s^2/(T_l T_r)$. When the interface has a non-vanishing width, this factor may be significantly different from unity, but even if we are working with a very sharp interfase, the factor is not unity when ΔT is an appreciable fraction of the average temperature of the interface T_s, as shown in reference [178].

In this Appendix we have shown a very rigurous formulation, just based on thermodynamical arguments, to obtain an expression for the thermal boundary resistance. This derivation does not assume anything about the interactions between the atoms of the system, and neither anything about the phonons of the system and the thermal energy exchange at the interface.

Appendix C

Convergence studies to solve the Boltzmann Transport Equation for the $PbTiO_3$

In order to assess the validity of our calculations we performed several convergence tests. We checked convergence against the size of the supercell used to calculate the second and third order interatomic force constants (IFCs), against the $\vec{q}$-point grid employed in the Brillouin zone, and against the cutoff radius for interatomic interactions when computing the third order IFCs.

In Fig. C.1 we show lattice thermal conductivity curves versus temperature for $PbTiO_3$ under no external field calculated with different supercell sizes $N_s \times N_s \times N_s$. All the calculations were performed using an $8 \times 8 \times 8$ Γ-centered $\vec{q}$-point grid. We see that for $N_s = 8$ all the diagonal components of the thermal conductivity tensor differ by less than 3% with respect to those obtained with $N_s = 7$ in the whole range of temperatures studied. Therefore, the calculations are reasonably converged for $N_s = 8$.

In Fig. C.2 we display the lattice thermal conductivity of PTO obtained from $N_s = 8$ supercell calculations and different $\vec{q}$-point grids of the $N_q \times N_q \times N_q$ type. While at low temperatures the differences between the lattice thermal conductivities obtained with $N_q = 8$ and $N_q = 16$ can add up to 15%, at $T = 300$ K these differences go down to 7% for κ_{xx} and 3% for κ_{zz}. Thus, the lattice thermal conductivity calculations of PTO are reasonably converged for an $8 \times 8 \times 8$ supercell and an $8 \times 8 \times 8$ $\vec{q}$-point grid, and the convergence is better for

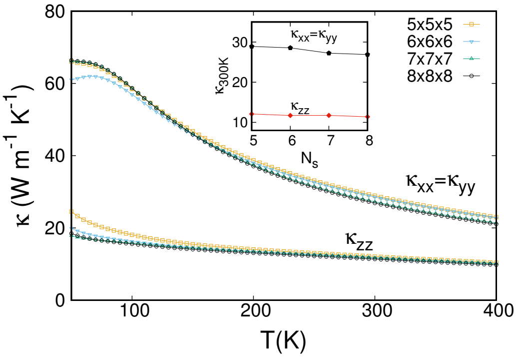

Figure C.1: *Convergence of the lattice thermal conductivity with the size of the supercell employed to obtain the second and third order IFCs for PTO under no external field. Supercells of the type $N_s \times N_s \times N_s$ were employed in all cases. The BTE was solved employing an $8 \times 8 \times 8$ $\vec{q}$-point grid in all cases. At any given temperature, the results for $N_s = 7$ and $N_s = 8$ differ at most by 6%. The inset shows the value of κ at $T = 300$ K for different supercell sizes.*

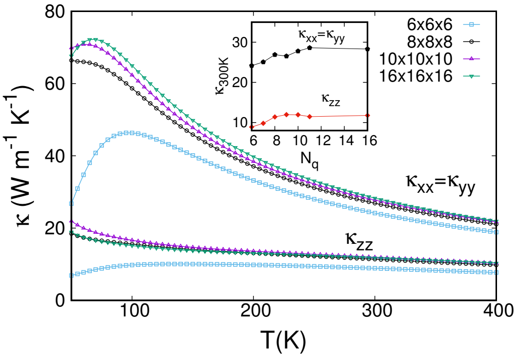

Figure C.2: *Convergence of the lattice thermal conductivity of PTO with the $\vec{q}$-point grid employed in the iterative solution of the BTE. Γ-centered grids of the type $N_q \times N_q \times N_q$ were employed in all cases. The BTE was solved employing an $8 \times 8 \times 8$ supercell in all cases. At any given temperature, the results obtained for $N_q = 8$ and $N_q = 16$ differ by $\sim 10\%$ close to the peak (at low temperatures) and by less than 5% at $T = 300$ K. The inset shows the value of κ at $T = 300$ K for different $\vec{q}$-point grid sizes.*

temperatures higher than 100 K. Note that increasing the value of N_s and/or N_q drastically increases the computational resources.

When computing the third order IFCs, a cutoff radius for interatomic interactions is employed in order to reduce the computational burden. We have checked that for PTO under parallel or antiparallel electric fields, as well as for PTO under no external field, our lattice thermal conductivity calculations including four or eight nearest neighbor interactions differ by less than 0.01% in the whole temperature range studied. In Fig. C.3 we display the calculated thermal conductivity curves for PTO under a perpendicular electric field employing different cutoffs in the calculations of the anharmonic IFCs. Perpendicular electric fields induce more severe deviations of the crystal cell geometry and reduce the symmetry of the system. In this case we found that convergence is achieved by accounting interactions among atoms up to twelfth nearest neighbors. This calculation shows deviations of at most 1 (6)% with respect to an equivalent calculation including fourteenth (eighth) nearest neighbors.

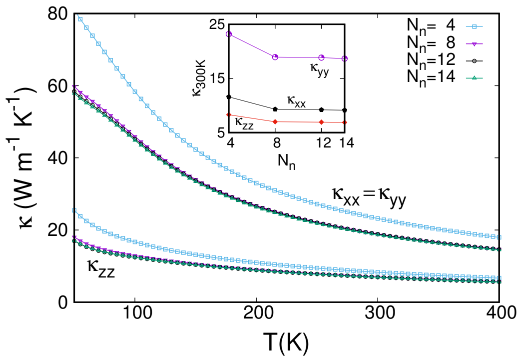

Figure C.3: *Convergence of the lattice thermal conductivity of PTO under a perpendicular electric field with respect to the number of nearest neighbors included in the calculation of the third order IFCs (N_n). The BTE was solved employing an $8 \times 8 \times 8$ supercell and an $8 \times 8 \times 8$ $\vec{q}$-point grid in all cases. The inset shows the value of κ at $T = 300$ K for different N_n values.*

Appendix D

Decomposition of the difference of a product

It is easy to prove that the difference of a product of three magnitudes (hereafter referred to as A, B, and C) in two different situations is given by

$$\begin{aligned} ABC - A^0B^0C^0 = (A - A^0)B^0C^0 + A^0(B - B^0)C^0 \\ + A^0B^0(C - C^0) + \mathcal{R}, \end{aligned} \tag{D.1}$$

where $\mathcal{R}$ would include all the terms that contain the deviation of two or three magnitudes with respect the reference situation labelled by the superscript "0", like

$$\mathcal{R} = (A - A^0)(B - B^0)C^0 + \cdots + (A - A^0)(B - B^0)(C - C^0). \tag{D.2}$$

In this Thesis, the superscript "0" will indicate zero-field quantities in Chapter 5 and zero-strain quantities in Chapter 7, while the magnitudes without superscript are for the cases with an electric field in Chapter 5 and for the strained cases in Chapter 7.

List of publications

Publications that have been included in this Thesis:

- Juan Antonio Seijas-Bellido, Carlos Escorihuela-Sayalero, Miquel Royo, Mathias P. Ljungberg, Jacek C. Wojdeł, Jorge Íñiguez, and Riccardo Rurali. A phononic switch based on ferroelectric domain walls. *Physical Review B* 96, 140101(R) (2017).
  DOI: 10.1103/PhysRevB.96.140101

- Juan Antonio Seijas-Bellido, Hugo Aramberri, Jorge Íñiguez, and Riccardo Rurali. Electric control of the heat flux through electrophononic effects. *Physical Review B* 97, 184306 (2018).
  DOI: 10.1103/PhysRevB.97.184306

- Juan Antonio Seijas-Bellido, Riccardo Rurali, Jorge Íñiguez, Luciano Colombo and Claudio Melis. Strain engineering of ZnO thermal conductivity. *Physical Review Materials* 3:065401, Jun 2019.
  DOI: 10.1103/PhysRevMaterials.3.065401

The contents of the previously mentioned publications have been
reproduced with the prior authorization of the
American Physical Society.

American Physical Society
Reuse and Permissions License

Submitted but not yet published work:

- Juan Antonio Seijas-Bellido, Jorge Íñiguez and Riccardo Rurali. Anisotropy-driven thermal-conductivity switching and thermal hysteresis in a ferroelectric.

Publications that have not been included:

- Martí Raya-Moreno, Hugo Aramberri, Juan Antonio Seijas-Bellido, Xavier Cartoixà, and Riccardo Rurali. Thermal conductivity of hexagonal Si and hexagonal Si nanowires from first-principles. *Appl. Phys. Lett.* 111, 032107 (2017).
DOI: 10.1063/1.4985278

- Pol Torres, Juan Antonio Seijas-Bellido, Carlos Escorihuela-Sayalero, Jorge Íñiguez, and Riccardo Rurali. Theoretical investigation of lattice thermal conductivity and electrophononic effects in $SrTiO_3$. *Physical Review Materials* 3:044404, Aprl 2019.
DOI: 10.1103/PhysRevMaterials.3.044404

Bibliography

[1] David G. Cahill, Wayne K. Ford, Kenneth E. Goodson, Gerald D. Mahan, Arun Majumdar, Humphrey J. Maris, Roberto Merlin, and Simon R. Phillpot. Nanoscale thermal transport. *Journal of Applied Physics*, 93(2):793–818, 2003.

[2] L. D. Hicks and M. S. Dresselhaus. Thermoelectric figure of merit of a one-dimensional conductor. *Phys. Rev. B*, 47:16631–16634, Jun 1993.

[3] Deyu Li, Yiying Wu, Philip Kim, Li Shi, Peidong Yang, and Arun Majumdar. Thermal conductivity of individual silicon nanowires. *Applied Physics Letters*, 83(14):2934–2936, 2003.

[4] Eric S. Toberer, Lauryn L. Baranowski, and Chris Dames. Advances in thermal conductivity. *Annual Review of Materials Research*, 42(1):179–209, 2012.

[5] David G. Cahill, Paul V. Braun, Gang Chen, David R. Clarke, Shanhui Fan, Kenneth E. Goodson, Pawel Keblinski, William P. King, Gerald D. Mahan, Arun Majumdar, Humphrey J. Maris, Simon R. Phillpot, Eric Pop, and Li Shi. Nanoscale thermal transport. II. 2003-2012. *Applied Physics Reviews*, 1(1):011305, 2014.

[6] Maria N. Luckyanova, Jivtesh Garg, Keivan Esfarjani, Adam Jandl, Mayank T. Bulsara, Aaron J. Schmidt, Austin J. Minnich, Shuo Chen, Mildred S. Dresselhaus, Zhifeng Ren, Eugene A. Fitzgerald, and Gang Chen. Coherent phonon heat conduction in superlattices. *Science*, 338(6109):936–939, 2012.

[7] Jayakanth Ravichandran, Ajay K. Yadav, Ramez Cheaito, Pim B. Rossen, Arsen Soukiassian, S. J. Suresha, John C. Duda,

Brian M. Foley, Che-Hui Lee, Ye Zhu, Arthur W. Lichtenberger, Joel E. Moore, David A. Muller, Darrell G. Schlom, Patrick E. Hopkins, Arun Majumdar, Ramamoorthy Ramesh, and Mark A. Zurbuchen. Crossover from incoherent to coherent phonon scattering in epitaxial oxide superlattices. *Nature Materials*, 13:168–172, Dec 2013.

[8] Martin Maldovan. Phonon wave interference and thermal bandgap materials. *Nature Materials*, 14:667–674, Jun 2015.

[9] Nianbei Li, Jie Ren, Lei Wang, Gang Zhang, Peter Hänggi, and Baowen Li. Colloquium: Phononics: Manipulating heat flow with electronic analogs and beyond. *Rev. Mod. Phys.*, 84:1045–1066, Jul 2012.

[10] Gerhart Groetzinger. Influence of an electric field on the thermal conductivity of a solid. *Nature*, 135(3424):1001–1001, 1935.

[11] Clifford E. Berry. The effect of an electric field on the thermal conductivity of glass. *The Journal of Chemical Physics*, 17(12):1355–1356, 1949.

[12] R. P. Gairola and B. S. Semwal. The effect of electric field on thermal conductivity of a ferroelectric crystal. II. *Journal of the Physical Society of Japan*, 43(3):954–960, 1977.

[13] Guangzhao Qin, Zhenzhen Qin, Sheng-Ying Yue, Qing-Bo Yan, and Ming Hu. External electric field driving the ultra-low thermal conductivity of silicene. *Nanoscale*, 9:7227–7234, 2017.

[14] H. H. Barrett and M. G. Holland. Thermal conductivity in perovskites. *Phys. Rev. B*, 2:3441–3443, Oct 1970.

[15] W. H. Huber, L. M. Hernandez, and A. M. Goldman. Electric field dependence of the thermal conductivity of quantum paraelectrics. *Phys. Rev. B*, 62:8588–8591, Oct 2000.

[16] Sebastian Volz, Jose Ordonez-Miranda, Andrey Shchepetov, Mika Prunnila, Jouni Ahopelto, Thomas Pezeril, Gwenaelle Vaudel, Vitaly Gusev, Pascal Ruello, Eva M. Weig, Martin Schubert, Mike Hettich, Martin Grossman, Thomas Dekorsy,

Francesc Alzina, Bartlomiej Graczykowski, Emigdio Chavez-Angel, J. Sebastian Reparaz, Markus R. Wagner, Clivia M. Sotomayor-Torres, Shiyun Xiong, Sanghamitra Neogi, and Davide Donadio. Nanophononics: state of the art and perspectives. *The European Physical Journal B*, 89(1):15, Jan 2016.

[17] Ilaria Zardo and Riccardo Rurali. Manipulating phonons at the nanoscale: Impurities and boundaries. *Current Opinion in Green and Sustainable Chemistry*, 17:1–7, 2019.

[18] Atsushi Togo, Laurent Chaput, and Isao Tanaka. Distributions of phonon lifetimes in brillouin zones. *Phys. Rev. B*, 91:094306, Mar 2015.

[19] Martí Raya-Moreno, Hugo Aramberri, Juan Antonio Seijas-Bellido, Xavier Cartoixà, and Riccardo Rurali. Thermal conductivity of hexagonal Si and hexagonal Si nanowires from first-principles. *Applied Physics Letters*, 111(3):032107, 2017.

[20] Martí Raya-Moreno, Riccardo Rurali, and Xavier Cartoixà. Semiconductor thermal conductivity for wurtzite and zinc-blende polytypes: the role of anharmonicity and phase space. *arXiv:1901.03268*, 01 2019.

[21] M. Harb, C. von Korff Schmising, H. Enquist, A. Jurgilaitis, I. Maximov, P. V. Shvets, A. N. Obraztsov, D. Khakhulin, M. Wulff, and J. Larsson. The c-axis thermal conductivity of graphite film of nanometer thickness measured by time resolved X-ray diffraction. *Applied Physics Letters*, 101(23):233108, 2012.

[22] Jesús A Del Alamo. Nanometre-scale electronics with III-V compound semiconductors. *Nature*, 479(7373):317, 2011.

[23] Vitor M Pereira and AH Castro Neto. Strain engineering of graphene's electronic structure. *Physical Review Letters*, 103(4):046801, 2009.

[24] Hiram J Conley, Bin Wang, Jed I Ziegler, Richard F Haglund Jr, Sokrates T Pantelides, and Kirill I Bolotin. Bandgap engineering of strained monolayer and bilayer MoS_2. *Nano letters*, 13(8):3626–3630, 2013.

[25] JL Hoyt, HM Nayfeh, S Eguchi, I Aberg, G Xia, T Drake, EA Fitzgerald, and DA Antoniadis. Strained silicon MOSFET technology. In *Electron Devices Meeting, 2002. IEDM'02. International*, pages 23–26. IEEE, 2002.

[26] Semiconductor Industry Association et al. International technology roadmap for semiconductors 2005 edition. *http://www.itrs.net/*, 2006.

[27] Yang Han, Jia-Yue Yang, and Ming Hu. Unusual strain response of thermal transport in dimerized three-dimensional graphene. *Nanoscale*, 10(11):5229–5238, 2018.

[28] Joseph Callaway. Model for lattice thermal conductivity at low temperatures. *Phys. Rev.*, 113:1046–1051, Feb 1959.

[29] Lasse Bjerg, Bo B. Iversen, and Georg K. H. Madsen. Modeling the thermal conductivities of the zinc antimonides ZnSb and Zn_4Sb_3. *Phys. Rev. B*, 89:024304, Jan 2014.

[30] Pinku Nath, Jose J. Plata, Demet Usanmaz, Cormac Toher, Marco Fornari, Marco Buongiorno Nardelli, and Stefano Curtarolo. High throughput combinatorial method for fast and robust prediction of lattice thermal conductivity. *Scripta Materialia*, 129:88–93, 2017.

[31] Mark E. Siemens, Qing Li, Ronggui Yang, Keith A. Nelson, Erik H. Anderson, Margaret M. Murnane, and Henry C. Kapteyn. Quasi-ballistic thermal transport from nanoscale interfaces observed using ultrafast coherent soft X-ray beams. *Nature Materials*, 9:26, Nov 2009.

[32] A. J. Minnich, J. A. Johnson, A. J. Schmidt, K. Esfarjani, M. S. Dresselhaus, K. A. Nelson, and G. Chen. Thermal conductivity spectroscopy technique to measure phonon mean free paths. *Phys. Rev. Lett.*, 107:095901, Aug 2011.

[33] D. Jou, G. Lebon, and J. Casas-Vázquez. *Extended Irreversible Thermodynamics*. Springer Netherlands, 2010.

[34] C. de Tomas, A. Cantarero, A. F. Lopeandia, and F. X. Alvarez. From kinetic to collective behavior in thermal transport

on semiconductors and semiconductor nanostructures. *Journal of Applied Physics*, 115(16):164314, 2014.

[35] C. de Tomas, A. Cantarero, A. F. Lopeandia, and F. X. Alvarez. Thermal conductivity of group-IV semiconductors from a kinetic-collective model. *Proceedings of the Royal Society of London A: Mathematical, Physical and Engineering Sciences*, 470(2169), 2014.

[36] R. A. Guyer and J. A. Krumhansl. Solution of the linearized phonon boltzmann equation. *Phys. Rev.*, 148:766–778, Aug 1966.

[37] Wu Li, Jesús Carrete, Nebil A. Katcho, and Natalio Mingo. ShengBTE: A solver of the boltzmann transport equation for phonons. *Computer Physics Communications*, 185(6):1747–1758, 2014.

[38] D A Greenwood. The boltzmann equation in the theory of electrical conduction in metals. *Proceedings of the Physical Society*, 71(4):585, 1958.

[39] H Tagashira, Y Sakai, and S Sakamoto. The development of electron avalanches in argon at high E/N values. II. Boltzmann equation analysis. *Journal of Physics D: Applied Physics*, 10(7):1051, 1977.

[40] J.M. Ziman. *Electrons and Phonons: The Theory of Transport Phenomena in Solids*. International series of monographs on physics. OUP Oxford, 2001.

[41] Aleksandr Chernatynskiy and Simon R. Phillpot. Evaluation of computational techniques for solving the boltzmann transport equation for lattice thermal conductivity calculations. *Phys. Rev. B*, 82:134301, Oct 2010.

[42] Giorgia Fugallo and Luciano Colombo. Corrigendum: Calculating lattice thermal conductivity: a synopsis (2018 Phys. Scr. 93 043002 [http://doi.org/10.1088/1402-4896/aaa6f3]). *Physica Scripta*, 93(5):059501, 2018.

[43] Marinko Jablan, Hrvoje Buljan, and Marin Soljačić. Plasmonics in graphene at infrared frequencies. *Phys. Rev. B*, 80:245435, Dec 2009.

[44] Jae Hun Seol, Insun Jo, Arden L. Moore, Lucas Lindsay, Zachary H. Aitken, Michael T. Pettes, Xuesong Li, Zhen Yao, Rui Huang, David Broido, Natalio Mingo, Rodney S. Ruoff, and Li Shi. Two-dimensional phonon transport in supported graphene. *Science*, 328(5975):213–216, 2010.

[45] Shin-ichiro Tamura. Isotope scattering of dispersive phonons in Ge. *Phys. Rev. B*, 27:858–866, Jan 1983.

[46] M Omini and A Sparavigna. An iterative approach to the phonon boltzmann equation in the theory of thermal conductivity. *Physica B: Condensed Matter*, 212(2):101–112, 1995.

[47] E. R. Hernández. Molecular dynamics: from basic techniques to applications (a molecular dynamics primer). *AIP Conference Proceedings*, 1077(1):95–123, 2008.

[48] Loup Verlet. Computer "experiments" on classical fluids. I. Thermodynamical properties of lennard-jones molecules. *Phys. Rev.*, 159:98–103, Jul 1967.

[49] Shuichi Nosé. A unified formulation of the constant temperature molecular dynamics methods. *The Journal of Chemical Physics*, 81(1):511–519, 1984.

[50] William G. Hoover. Canonical dynamics: Equilibrium phase-space distributions. *Phys. Rev. A*, 31:1695–1697, Mar 1985.

[51] E. Lampin, P. L. Palla, P.-A. Francioso, and F. Cleri. Thermal conductivity from approach-to-equilibrium molecular dynamics. *Journal of Applied Physics*, 114(3):033525, 2013.

[52] Claudio Melis and Luciano Colombo. Lattice thermal conductivity of $\mathrm{Si}_{1-x}\mathrm{Ge}_x$ nanocomposites. *Phys. Rev. Lett.*, 112:065901, Feb 2014.

[53] Miquel Royo and Riccardo Rurali. Tuning thermal transport in Si nanowires by isotope engineering. *Phys. Chem. Chem. Phys.*, 18:26262–26267, 2016.

[54] Assil Bouzid, Hayat Zaoui, Pier Luca Palla, Guido Ori, Mauro Boero, Carlo Massobrio, Fabrizio Cleri, and Evelyne Lampin. Thermal conductivity of glassy $GeTe_4$ by first-principles molecular dynamics. *Phys. Chem. Chem. Phys.*, 19:9729–9732, 2017.

[55] Patrick K. Schelling, Simon R. Phillpot, and Pawel Keblinski. Comparison of atomic-level simulation methods for computing thermal conductivity. *Phys. Rev. B*, 65:144306, Apr 2002.

[56] D. P. Sellan, E. S. Landry, J. E. Turney, A. J. H. McGaughey, and C. H. Amon. Size effects in molecular dynamics thermal conductivity predictions. *Phys. Rev. B*, 81:214305, Jun 2010.

[57] Eugene Helfand. Transport coefficients from dissipation in a canonical ensemble. *Phys. Rev.*, 119:1–9, Jul 1960.

[58] Massoud Kaviany. *Heat Transfer Physics*. Cambridge University Press, 2 edition, 2014.

[59] S. Viscardy, J. Servantie, and P. Gaspard. Transport and Helfand moments in the Lennard-Jones fluid. II. Thermal conductivity. *The Journal of Chemical Physics*, 126(18):184513, 2007.

[60] A. Kinaci, J. B. Haskins, and T. Çağın. On calculation of thermal conductivity from einstein relation in equilibrium molecular dynamics. *The Journal of Chemical Physics*, 137(1):014106, 2012.

[61] S. Viscardy, J. Servantie, and P. Gaspard. Transport and Helfand moments in the Lennard-Jones fluid. I. Shear viscosity. *The Journal of Chemical Physics*, 126(18):184512, 2007.

[62] Tatyana Kuznetsova and Bj⊘rn Kvamme. Ergodicity range of Nosé-Hoover thermostat parameters and entropy-related properties of model water systems. *Molecular Simulation*, 21(4):205–225, 1999.

[63] N.W. Ashcroft and N.D. Mermin. *Solid State Physics*. HRW international editions. Holt, Rinehart and Winston, 1976.

[64] J. Tersoff. New empirical approach for the structure and energy of covalent systems. *Phys. Rev. B*, 37:6991–7000, Apr 1988.

[65] The classical equation of state of gaseous helium, neon and argon. *Proceedings of the Royal Society of London A: Mathematical, Physical and Engineering Sciences*, 168(933):264–283, 1938.

[66] M. Dixon. Molecular dynamics studies of molten NaI. *Philosophical Magazine B*, 48(1):13–29, 1983.

[67] P J Mitchell and D Fincham. Shell model simulations by adiabatic dynamics. *Journal of Physics: Condensed Matter*, 5(8):1031, 1993.

[68] Adri C. T. van Duin, Siddharth Dasgupta, Francois Lorant, and William A. Goddard. ReaxFF: A reactive force field for hydrocarbons. *The Journal of Physical Chemistry A*, 105(41):9396–9409, 2001.

[69] R.M. Martin, R.M. Martin, and Cambridge University Press. *Electronic Structure: Basic Theory and Practical Methods.* Cambridge University Press, 2004.

[70] Jacek C. Wojdeł, Patrick Hermet, Mathias P. Ljungberg, Philippe Ghosez, and Jorge Íñiguez. First-principles model potentials for lattice-dynamical studies: general methodology and example of application to ferroic perovskite oxides. *J. Phys.: Condens. Matter*, 25:305401, 2013.

[71] X.W. Sun, Y.D. Chu, T. Song, Z.J. Liu, L. Zhang, X.G. Wang, Y.X. Liu, and Q.F. Chen. Application of a shell model in molecular dynamics simulation to ZnO with zinc-blende cubic structure. *Solid State Communications*, 142(1):15–19, 2007.

[72] Shuangxing Dai, Martin L Dunn, and Harold S Park. Piezoelectric constants for ZnO calculated using classical polarizable core-shell potentials. *Nanotechnology*, 21(44):445707, 2010.

[73] Mats Nyberg, Martin A. Nygren, Lars G. M. Pettersson, David H. Gay, and Andrew L. Rohl. Hydrogen dissociation

on reconstructed ZnO surfaces. *The Journal of Physical Chemistry*, 100(21):9054–9063, 1996.

[74] K. Momeni, Gregory M. Odegard, and Reza S. Yassar. Finite size effect on the piezoelectric properties of ZnO nanobelts: A molecular dynamics approach. *Acta Materialia*, 60(13-14):5117–5124, 8 2012.

[75] Jacek C. Wojdeł and Jorge Íñiguez. Testing simple predictors for the temperature of a structural phase transition. *Phys. Rev. B*, 90:014105, Jul 2014.

[76] Jacek C. Wojdeł and Jorge Íñiguez. Ferroelectric transitions at ferroelectric domain walls found from first principles. *Phys. Rev. Lett.*, 112:247603, Jun 2014.

[77] Padraic Shafer, Pablo García-Fernández, Pablo Aguado-Puente, Anoop R. Damodaran, Ajay K. Yadav, Christopher T. Nelson, Shang-Lin Hsu, Jacek C. Wojdeł, Jorge Íñiguez, Lane W. Martin, Elke Arenholz, Javier Junquera, and Ramamoorthy Ramesh. Emergent chirality in the electric polarization texture of titanate superlattices. *Proceedings of the National Academy of Sciences*, 115(5):915–920, 2018.

[78] Pavlo Zubko, Jacek C. Wojdeł, Marios Hadjimichael, Stéphanie Fernandez-Pena, Anaïs Sené, Igor Luk'yanchuk, Jean-Marc Triscone, and Jorge Íñiguez. Negative capacitance in multidomain ferroelectric superlattices. *Nature*, 534:524, 2016/06/13/online.

[79] G. Venkataraman. Soft modes and structural phase transitions. *Bulletin of Materials Science*, 1(3):129–170, Dec 1979.

[80] Ph. Ghosez, X. Gonze, and J.-P. Michenaud. Coulomb interaction and ferroelectric instability of $BaTiO_3$. *EPL (Europhysics Letters)*, 33(9):713, 1996.

[81] A. Sani, M. Hanfland, and D. Levy. Pressure and temperature dependence of the ferroelectric-paraelectric phase transition in $PbTiO_3$. *Journal of Solid State Chemistry*, 167(2):446–452, 2002.

[82] H. D. Megaw. Ferroelectricity and crystal structure. II. *Acta Crystallographica*, 7(2):187–194, Feb 1954.

[83] Lü Weiming, Li Changjian, Zheng Limei, Xiao Juanxiu, Lin Weinan, Li Qiang, Wang Xiao Renshaw, Huang Zhen, Zeng Shengwei, Han Kun, Zhou Wenxiong, Zeng Kaiyang, Chen Jingsheng, Ariando, Cao Wenwu, and Venkatesan Thirumalai. Multi-nonvolatile state resistive switching arising from ferroelectricity and oxygen vacancy migration. *Advanced Materials*, 29(24):1606165.

[84] X. Tian and A. Toriumi. New opportunity of ferroelectric tunnel junction memory with ultrathin HfO_2-based oxides. In *2017* IEEE *Electron Devices Technology and Manufacturing Conference (EDTM)*, pages 36–64, Feb 2017.

[85] Yu Hyeonggeun, Chung Ching-Chang, Shewmon Nate, Ho Szuheng, Carpenter Joshua H., Larrabee Ryan, Sun Tianlei, Jones Jacob L., Ade Harald, O'Connor Brendan T., and So Franky. Flexible inorganic ferroelectric thin films for nonvolatile memory devices. *Advanced Functional Materials*, 27(21):1700461.

[86] Matteo Ghittorelli, Thomas Lenz, Hamed Sharifi Dehsari, Dong Zhao, Kamal Asadi, Paul W. M. Blom, Zsolt M. Kovács-Vajna, Dago M. de Leeuw, and Fabrizio Torricelli. Quantum tunnelling and charge accumulation in organic ferroelectric memory diodes. *Nature Communications*, 8:15741, Jun 2017.

[87] Hyun Wook Shin and Jong Yeog Son. Nonvolatile ferroelectric memory based on $PbTiO_3$ gated single-layer MoS_2 field-effect transistor. *Electronic Materials Letters*, 14(1):59–63, Jan 2018.

[88] Ryoichi Takayama, Yoshihiro Tomita, K Iijima, and I. Ueda. Pyroelectric properties and application to infrared sensors of $PbTiO_3$, $PbLaTiO_3$ and $PbZrTiO_3$ ferroelectric thin films. *Ferroelectrics*, 118(1):325–342, 1991.

[89] Wei Ren, Yun Liu, Xiaoqing Wu, Liangying Zhang, and Xi Yao. Properties of $PbTiO_3$, La-modified $PbTiO_3$ and $Pb(Zr, Ti)O_3$ thin films and their application to infrared detectors. *Integrated Ferroelectrics*, 15(1-4):271–279, 1997.

[90] M. Okuyama and Y. Hamakawa. Ferroelectric $PbTiO_3$ thin films and their application. *International Journal of Engineering Science*, 29(3):391–400, 1991.

[91] Abdulnour Y. Toukmaji and John A. Board. Ewald summation techniques in perspective: a survey. *Computer Physics Communications*, 95(2):73–92, 1996.

[92] Chernatynskiy Aleksandr, Turney Joseph E., McGaughey Alan J. H., Amon Cristina H., and Phillpot Simon R. Phonon-mediated thermal conductivity in ionic solids by lattice dynamics-based methods. *Journal of the American Ceramic Society*, 94(10):3523–3531.

[93] Xavier Gonze and Changyol Lee. Dynamical matrices, born effective charges, dielectric permittivity tensors, and interatomic force constants from density-functional perturbation theory. *Phys. Rev. B*, 55:10355–10368, Apr 1997.

[94] Carlos Escorihuela-Sayalero, Jacek C. Wojdeł, and Jorge Íñiguez. Efficient systematic scheme to construct second-principles lattice dynamical models. *Phys. Rev. B*, 95:094115, Mar 2017.

[95] M. J. Haun, E. Furman, S. J. Jang, H. A. McKinstry, and L. E. Cross. Thermodynamic theory of $PbTiO_3$. *Journal of Applied Physics*, 62(8):3331–3338, 1987.

[96] Pablo García-Fernández, Jacek C. Wojdeł, Jorge Íñiguez, and Javier Junquera. Second-principles method for materials simulations including electron and lattice degrees of freedom. *Phys. Rev. B*, 93:195137, May 2016.

[97] Geert Heideman. *Reduced zinc oxide levels in sulphur vulcanisation of rubber compounds; mechanistic aspects of the role of activators and multifunctional additives.* Doctoral Thesis. University of Twente, 2004.

[98] F.C. Porter. *Zinc Handbook: Properties, Processing, and Use In Design.* Mechanical Engineering. Taylor & Francis, 1991.

[99] Amir Moezzi, Andrew M. McDonagh, and Michael B. Cortie. Zinc oxide particles: Synthesis, properties and applications. *Chemical Engineering Journal*, 185-186:1–22, 2012.

[100] A. Wei, X. W. Sun, J. X. Wang, Y. Lei, X. P. Cai, C. M. Li, Z. L. Dong, and W. Huang. Enzymatic glucose biosensor based on ZnO nanorod array grown by hydrothermal decomposition. *Applied Physics Letters*, 89(12):123902, 2006.

[101] Pratima R. Solanki, Ajeet Kaushik, Anees A. Ansari, and B. D. Malhotra. Nanostructured zinc oxide platform for cholesterol sensor. *Applied Physics Letters*, 94(14):143901, 2009.

[102] Chen, Ying, Saraf, Gaurav, Wittstruck, Richard H., Emanetoglu, Nuri W., Lu, and Yicheng. Studies on $Mg_xZn_{1-x}O$ thin film resonator for mass sensor application. *Proceedings of the 37th Annual Precise Time and Time Interval Systems and Applications Meeting, Vancouver, Canada*, pages 142–145, 2005.

[103] M.J. Vellekoop, C.C.O. Visser, P.M. Sarro, and A. Venema. Compatibility of zinc oxide with silicon IC processing. *Sensors and Actuators A: Physical*, 23(1):1027–1030, 1990. Proceedings of the 5th International Conference on Solid-State Sensors and Actuators and Eurosensors III.

[104] N.W Emanetoglu, C Gorla, Y Liu, S Liang, and Y Lu. Epitaxial ZnO piezoelectric thin films for saw filters. *Materials Science in Semiconductor Processing*, 2(3):247–252, 1999.

[105] C. Jagadish and S.J. Pearton. *Zinc Oxide Bulk, Thin Films and Nanostructures: Processing, Properties, and Applications.* Elsevier Science, 2011.

[106] A J Kulkarni and M Zhou. Tunable thermal response of ZnO nanowires. *Nanotechnology*, 18(43):435706, 2007.

[107] David Jason Binks. *Computational Modelling of Zinc Oxide and Related Oxide Ceramics.* Doctoral Thesis. University of Surrey, 1994.

[108] D. Jason Binks and Robin W. Grimes. The non-stoichiometry of zinc and chromium excess zinc chromite. *Solid State Communications*, 89(11):921–924, 1994.

[109] G V Lewis and C R A Catlow. Potential models for ionic oxides. *Journal of Physics C: Solid State Physics*, 18(6):1149, 1985.

[110] DR Lide et al. Handbook of chemistry and physics. CRC press, boca raton, fl. *Handbook of chemistry and physics. 88th ed. CRC Press, Boca Raton, FL.*, 2007.

[111] Stephen Robert Yeandel. *Atomistic Simulation of Thermal Transport in Oxide Nanomaterials.* Doctoral Thesis. University of Bath, 2015.

[112] K.H. Rieder. Helium diffraction from MgO(100). *Surface Science*, 118(1):57–65, 1982.

[113] G. V. Paolini, P. J. D. Lindan, and J. H. Harding. The thermal conductivity of defective crystals. *The Journal of Chemical Physics*, 106(9):3681–3687, 1997.

[114] Lixin Zhang and Hanchen Huang. Structural transformation of ZnO nanostructures. *Applied Physics Letters*, 90(2):023115, 2007.

[115] A.J.H. Mante and J. Volger. Phonon transport in barium titanate. *Physica*, 52(4):577–604, 1971.

[116] M. A. Weilert, M. E. Msall, J. P. Wolfe, and A. C. Anderson. Mode dependent scattering of phonons by domain walls in ferroelectric KDP. *Z. Phys. B: Condens. Matter*, 91(179), 1993.

[117] M. A. Weilert, M. E. Msall, A. C. Anderson, and J. P. Wolfe. Phonon scattering from ferroelectric domain walls: Phonon imaging in KDP. *Phys. Rev. Lett.*, 71:735–738, Aug 1993.

[118] Brian M. Foley, Elizabeth A. Paisley, Christopher DiAntonio, Tom Chavez, Mia Blea-Kirby, Geoff Brennecka, John T. Gaskins, Jon F. Ihlefeld, and Patrick E. Hopkins. Phonon scattering mechanisms dictating the thermal conductivity of lead zirconate titanate ($PbZr_{1-x}Ti_xO_3$) thin films across the compositional

phase diagram. *Journal of Applied Physics*, 121(20):205104, 2017.

[119] Jon F. Ihlefeld, Brian M. Foley, David A. Scrymgeour, Joseph R. Michael, Bonnie B. McKenzie, Douglas L. Medlin, Margeaux Wallace, Susan Trolier-McKinstry, and Patrick E. Hopkins. Room-temperature voltage tunable phonon thermal conductivity via reconfigurable interfaces in ferroelectric thin films. *Nano Letters*, 15(3):1791–1795, Mar 2015.

[120] Jian Jun Wang, Yi Wang, Jon F. Ihlefeld, Patrick E. Hopkins, and Long Qing Chen. Tunable thermal conductivity via domain structure engineering in ferroelectric thin films: A phase-field simulation. *Acta Materialia*, 111:220–231, 6 2016.

[121] Miquel Royo, Carlos Escorihuela-Sayalero, Jorge Íñiguez, and Riccardo Rurali. Ferroelectric domain wall phonon polarizer. *Phys. Rev. Materials*, 1:051402, Oct 2017.

[122] Anindya Roy. Estimates of the thermal conductivity and the thermoelectric properties of $PbTiO_3$ from first principles. *Phys. Rev. B*, 93:100101, Mar 2016.

[123] Makoto Tachibana, Taras Kolodiazhnyi, and Eiji Takayama-Muromachi. Thermal conductivity of perovskite ferroelectrics. *Applied Physics Letters*, 93(9):092902, 2008.

[124] Juan Antonio Seijas-Bellido, Carlos Escorihuela-Sayalero, Miquel Royo, Mathias P. Ljungberg, Jacek C. Wojdeł, Jorge Íñiguez, and Riccardo Rurali. A phononic switch based on ferroelectric domain walls. *Phys. Rev. B*, 96:140101, Oct 2017.

[125] Simon Lu and Alan J. H. McGaughey. Thermal conductance of superlattice junctions. *AIP Advances*, 5(5):053205, 2015.

[126] Bijay Kumar Sahoo. Effect of piezoelectric polarization on phonon group velocity in nitride wurtzites. *Journal of Materials Science*, 47(6):2624–2629, Mar 2012.

[127] A Togo and I Tanaka. First principles phonon calculations in materials science. *Scr. Mater.*, 108:1–5, Nov 2015.

[128] Bin Xu, Jorge Íñiguez, and L. Bellaiche. Designing lead-free antiferroelectrics for energy storage. *Nature Communications*, 8:15682, May 2017. Article.

[129] Alain Mercy, Jordan Bieder, Jorge Íñiguez, and Philippe Ghosez. Structurally triggered metal-insulator transition in rare-earth nickelates. *Nature Communications*, 8(1677), 2017.

[130] Huaxiang Fu and Ronald E. Cohen. Polarization rotation mechanism for ultrahigh electromechanical response in single-crystal piezoelectrics. *Nature*, 403:281–283, 2000.

[131] L. Bellaiche, Alberto García, and David Vanderbilt. Finite-temperature properties of $\mathrm{Pb}(\mathrm{Zr}_{1-x}\mathrm{Ti}_x)O_3$ alloys from first principles. *Phys. Rev. Lett.*, 84:5427–5430, Jun 2000.

[132] G Gesele, J Linsmeier, V Drach, J Fricke, and R Arens-Fischer. Temperature-dependent thermal conductivity of porous silicon. *Journal of Physics D: Applied Physics*, 30(21):2911–2916, nov 1997.

[133] Riccardo Dettori, Claudio Melis, Xavier Cartoixà, Riccardo Rurali, and Luciano Colombo. Model for thermal conductivity in nanoporous silicon from atomistic simulations. *Phys. Rev. B*, 91:054305, Feb 2015.

[134] B. L. Zink, R. Pietri, and F. Hellman. Thermal conductivity and specific heat of thin-film amorphous silicon. *Phys. Rev. Lett.*, 96:055902, Feb 2006.

[135] Sara Yazji, Eric A. Hoffman, Daniele Ercolani, Francesco Rossella, Alessandro Pitanti, Alessandro Cavalli, Stefano Roddaro, Gerhard Abstreiter, Lucia Sorba, and Ilaria Zardo. Complete thermoelectric benchmarking of individual InSb nanowires using combined micro-raman and electric transport analysis. *Nano Research*, 8(12):4048–4060, Dec 2015.

[136] S Yazji, M Y Swinkels, M De Luca, E A Hoffmann, D Ercolani, S Roddaro, G Abstreiter, L Sorba, E P A M Bakkers, and I Zardo. Assessing the thermoelectric properties of single InSb nanowires: the role of thermal contact resistance. *Semiconductor Science and Technology*, 31(6):064001, may 2016.

[137] J. Li, B. Nagaraj, H. Liang, W. Cao, Chi. H. Lee, and R. Ramesh. Ultrafast polarization switching in thin-film ferroelectrics. *Applied Physics Letters*, 84(7):1174–1176, 2004.

[138] R. G. Ross, P. Andersson, B. Sundqvist, and G. Backstrom. Thermal conductivity of solids and liquids under pressure. *Rep. Prog. Phys.*, 47(10):1347, 1984.

[139] D. M. Darbha and H. H. Schloessin. *Anisotropic Lattice Thermal Conductivity of α-Quartz as a Function of Pressure and Temperature*, pages 183–190. Springer US, Boston, MA, 1976.

[140] A.E. Beck, D.M. Darbha, and H.H. Schloessin. Lattice conductivities of single-crystal and polycrystalline materials at mantle pressures and temperatures. *Phys. Earth Planet. Inter.*, 17(1):35–53, 1978.

[141] Hideo Yukutake and Mitshuhiko Shimada. Thermal conductivity of NaCl, MgO, coesite and stishovite up to 40 kbar. *Phys. Earth Planet. Inter.*, 17(3):193–200, 1978.

[142] P. I. Baranskii, P. P. Kogutyuk, and V. V. Savyak. Thermal-conductivity of n-type germanium and silicon under strong uniaxial elastic-deformation. *Sov. Phys.-Semicond.*, 15(9):1061–1062, 1981.

[143] K. I. Amirkhanov, Y. B. Magomedov, S. N. Emirov, and N. L. Kramynina. Pressure dependence of the thermal conductivity of InSb. *Sov. Phys.-Solid St.*, 21(9):1619–20, 1979.

[144] A.A Averkin, Z. Z. Zhaparov, and L. S. Stilbans. Influence of hydrostatic pressure on thermal-conductivity of semiconducting materials. *Sov. Phys.-Semicond.*, 5(11), 1972.

[145] Wei Lu and Charles M. Lieber. Semiconductor nanowires. *J. Phys. D: Appl. Phys.*, 39(21):R387–R406, 2006.

[146] Riccardo Rurali. Colloquium: Structural, electronic, and transport properties of silicon nanowires. *Rev. Mod. Phys.*, 82(1):427–449, 2010.

[147] J. Greil, A. Lugstein, C. Zeiner, G. Strasser, and E. Bertagnolli. Tuning the electro-optical properties of germanium nanowires by tensile strain. *Nano Letters*, 12(12):6230–6234, 2012.

[148] Karl Winkler, Emmerich Bertagnolli, and Alois Lugstein. Origin of anomalous piezoresistive effects in VLS grown Si nanowires. *Nano Lett.*, 15(3):1780–1785, 2015.

[149] Hongti Zhang, Jerry Tersoff, Shang Xu, Huixin Chen, Qiaobao Zhang, Kaili Zhang, Yong Yang, Chun-Sing Lee, King-Ning Tu, Ju Li, and Yang Lu. Approaching the ideal elastic strain limit in silicon nanowires. *Science Advances*, 2(8), 2016.

[150] Zhong Lin Wang and Jinhui Song. Piezoelectric nanogenerators based on zinc oxide nanowire arrays. *Science*, 312(5771):242–246, 2006.

[151] Sheng Xu, Yong Qin, Chen Xu, Yaguang Wei, Rusen Yang, and Zhong Lin Wang. Self-powered nanowire devices. *Nature Nanotech.*, 5:366–373, 2010.

[152] Jun Zhou, Yudong Gu, Peng Fei, Wenjie Mai, Yifan Gao, Rusen Yang, Gang Bao, and Zhong Lin Wang. Flexible piezotronic strain sensor. *Nano Lett.*, 8(9):3035–3040, 2008.

[153] David Keith Chalmers MacDonald. *Thermoelectricity: an introduction to the principles.* Courier Corporation, 2006.

[154] DA Polvani, JF Meng, NV Chandra Shekar, J Sharp, and JV Badding. Large improvement in thermoelectric properties in pressure-tuned p-type $Sb_{1.5}Bi_{0.5}Te_3$. *Chemistry of materials*, 13(6):2068–2071, 2001.

[155] Gang Zhang and Yong-Wei Zhang. Strain effects on thermoelectric properties of two-dimensional materials. *Mechanics of Materials*, 91:382–398, 2015.

[156] LAA Algharagholy, T Pope, and CJ Lambert. Strain-induced bi-thermoelectricity in tapered carbon nanotubes. *Journal of Physics: Condensed Matter*, 30(10):105304, 2018.

[157] HY Lv, WJ Lu, DF Shao, and YP Sun. Enhanced thermoelectric performance of phosphorene by strain-induced band convergence. *Physical Review B*, 90(8):085433, 2014.

[158] Toshiki Tsubota, Michitaka Ohtaki, Koichi Eguchi, and Hiromichi Arai. Thermoelectric properties of Al-doped ZnO as a promising oxide material for high-temperature thermoelectric conversion. *Journal of Materials Chemistry*, 7(1):85–90, 1997.

[159] Richard S Thompson, Dongdong Li, Christopher M Witte, and Jia G Lu. Weak localization and electron- electron interactions in indium-doped ZnO nanowires. *Nano letters*, 9(12):3991–3995, 2009.

[160] Minjie Zhou, Haojun Zhu, Yang Jiao, Yangyan Rao, Suikong Hark, Yang Liu, Lianmao Peng, and Quan Li. Optical and electrical properties of Ga-doped ZnO nanowire arrays on conducting substrates. *The Journal of Physical Chemistry C*, 113(20):8945–8947, 2009.

[161] Steve Plimpton. Fast parallel algorithms for short-range molecular dynamics. *Journal of Computational Physics*, 117(1):1–19, 1995.

[162] DO Demchenko and David B Ameen. Lattice thermal conductivity in bulk and nanosheet Na_xCoO_2. *Computational Materials Science*, 82:219–225, 2014.

[163] Jianwei Che, Tahir Çağın, Weiqiao Deng, and William A Goddard III. Thermal conductivity of diamond and related materials from molecular dynamics simulations. *The Journal of Chemical Physics*, 113(16):6888–6900, 2000.

[164] Leila Momenzadeh, Behdad Moghtaderi, Irina V Belova, and Graeme E Murch. Determination of the lattice thermal conductivity of the TiO_2 polymorphs rutile and anatase by molecular dynamics simulation. *Computational Condensed Matter*, 17:e00342, 2018.

[165] Juan Antonio Seijas-Bellido, Riccardo Rurali, Jorge Íñiguez, Luciano Colombo, and Claudio Melis. Strain engineering of

ZnO thermal conductivity. *Phys. Rev. Materials*, 3:065401, Jun 2019.

[166] X. Wu, J. Lee, V. Varshney, J. L. Wohlwend, A. K. Roy, and T. Luo. Thermal conductivity of wurtzite zinc-oxide from first-principles lattice dynamics - a comparative study with gallium nitride. *Scientific Reports*, 6(22504), 2016.

[167] A.J.H. McGaughey and M. Kaviany. Thermal conductivity decomposition and analysis using molecular dynamics simulations: Part II. Complex silica structures. *International Journal of Heat and Mass Transfer*, 47(8):1799–1816, 2004.

[168] G.A. Greene, Y.I. Cho, J.P. Hartnett, and A. Bar-Cohen. *Advances in Heat Transfer*. Number v. 39 in Advances in Heat Transfer. Elsevier Science, 2006.

[169] Jianjun Dong, Otto F Sankey, and Charles W Myles. Theoretical study of the lattice thermal conductivity in Ge framework semiconductors. *Physical review letters*, 86(11):2361, 2001.

[170] Xufei Wu, Jonghoon Lee, Vikas Varshney, Jennifer L Wohlwend, Ajit K Roy, and Tengfei Luo. Thermal conductivity of wurtzite zinc-oxide from first-principles lattice dynamics–a comparative study with gallium nitride. *Scientific reports*, 6:22504, 2016.

[171] Somnath Bhowmick and Vijay B. Shenoy. Effect of strain on the thermal conductivity of solids. *The Journal of Chemical Physics*, 125(16):164513, 2006.

[172] Kunpeng Yuan, Xiaoliang Zhang, Dawei Tang, and Ming Hu. Anomalous pressure effect on the thermal conductivity of ZnO, GaN, and AlN from first-principles calculations. *Physical Review B*, 98(14):144303, 2018.

[173] R Ghosh, D Basak, and Shinobu Fujihara. Effect of substrate-induced strain on the structural, electrical, and optical properties of polycrystalline ZnO thin films. *Journal of Applied Physics*, 96(5):2689–2692, 2004.

[174] Tao Ouyang and Ming Hu. Competing mechanism driving diverse pressure dependence of thermal conductivity of X Te (X = Hg, Cd, and Zn). *Physical Review B*, 92(23):235204, 2015.

[175] Pol Torres, Juan Antonio Seijas-Bellido, Carlos Escorihuela-Sayalero, Jorge Íñiguez, and Riccardo Rurali. Theoretical investigation of lattice thermal conductivity and electrophononic effects in srtio$_3$. *Phys. Rev. Materials*, 3:044404, Apr 2019.

[176] Justin B. Haskins, Alper Kinaci, Cem Sevik, and Tahir Çağın. Equilibrium limit of thermal conduction and boundary scattering in nanostructures. *The Journal of Chemical Physics*, 140(24):244112, 2014.

[177] S. Kjelstrup and D. Bedeaux. *Non-equilibrium Thermodynamics of Heterogeneous Systems*, volume 16. Series on Advances in Statistical Mechanics, Vol 16, World Scientific, Singapore, 2008.

[178] R. Dettori, C. Melis, X. Cartoixà, R. Rurali, and L. Colombo. Thermal boundary resistance in semiconductors by non-equilibrium thermodynamics. *Advances in Physics: X*, 1(2):246–261, 2016.